PIEZO-PHOTOTRONICS: FROM EXPERIMENTS TO THEORY

A Thesis
Presented to
The Academic Faculty

by

Ying Liu

In Partial Fulfillment
of the Requirements for the Degree
Doctor of Philosophy in the
School of Materials Science and Engineering

Georgia Institute of Technology

August, 2014

PIEZO-PHOTOTRONICS: FROM EXPERIMENTS TO THEORY

Approved by:

Dr. Zhong Lin Wang, Advisor
School of Materials Science and Engineering
Georgia Institute of Technology

Dr. Ken Gall
School of Materials Science and Engineering
Georgia Institute of Technology

Dr. Mostafa El-Sayed
School of Chemistry and Biochemistry
Georgia Institute of Technology

Dr. Suresh Sitaraman
School of Mechanical Engineering
Georgia Institute of Technology

Dr. Christopher Summers
School of Materials Science and Engineering
Georgia Institute of Technology

Date Approved: June 23rd, 2014

To my mother and my deceased father

And to all researchers building the bridge between science and technology

ACKNOWLEDGEMENTS

First I would like to thank my advisor, Dr. Zhong Lin Wang, for leading me into this field of research that I enjoy so much during these years, for his practice as the best model, his generous guidance, support and encouragement all the way through my PhD study. I would also like to give thanks to members of my dissertation committee, Dr. El-Sayed, Dr. Summers, Dr. Gall and Dr. Sitaraman, and for the time, patience and valuable advice they generously offer. Also thank the professors who have instructed the courses I took.

I would like to thank my colleagues, who let me learn so much from them during cooperation, and provided insightful discussions both in research and in course work. None of the work in this thesis is possible without the help from each and every of them. Special thanks to Dr. Qing Yang, who worked with me hand in hand on research related to this thesis.

I would also like to thank my friends who offer warm company and help in my personal life, so I can settle smoothly in this new country far from home and enjoy my personal life outside my research and study. Special thanks to my roommates, Xiaolin Wang and Mengdie Hu, who cared for me like sisters over these five years

Lastly, I would like to thank my family. My mother has given me every bit of support she can offer both physically and spiritually. My deceased father has taught me so many things from my birth to my teenage, and even now he is gone, the older I get, the more I learn from him.

TABLE OF CONTENTS

LIST OF TABLES

LIST OF FIGURES

LIST OF SYMBOLS

R	responsivity
I_{ph}	photocurrent
P_{ill}	illumination power
P	emitted optical power
η_{ext}	external quantum efficiency
q	electronic charge
h	Planck's constant
v	frequency of the light
Γ_G	internal gain
I_n	root mean square value of the noise current
Δf	electrical bandwidth
I	device current
V	applied voltage
D	electric displacement
ε_r	permittivity
E	electric field
D_F	integral of the energy along Fermi level
m^*	effective electron mass
ξ	average electric field is given by
ψ_{bi}	built-in potential
$\boldsymbol{\varepsilon}$	strain
s	compliance matrix
T_s	stress
$[e]$	direct piezoelectric coefficient matrix

A^*	Richardson constant
T	temperature
φ_n	effective Schottky barrier height
J_{sv}	slowly varying current density term
k	Boltzmann constant
E_0	tunneling parameter
Δn	excess electron concentration
Δp	excess hole concentration
N_D	donor doping density
N_A	acceptor doping density
n	free electron density
p	free hole density
τ_n	carrier lifetime
$G_L(I)$	rate of photon generation
ρ_{piezo}	density of the strain-induced piezo-charges
W_{piezo}	width of the piezo-charge distribution
S_R	cross section area for reverse junction
S_F	cross section area for forward junction
R_{NW}	resistance of the nanowire
V_{NW}	voltage across the nanowire
V_R	voltage across the reverse junction
V_F	voltage across the forward junction
P	resistance of the semiconductor
l	length of nanowire
$\delta\rho$	resistance change due to piezoresistance effect

δl	change in nanowire length
π	piezoresistance coefficient
Ψ_n	potential built in the n-type side
Ψ_p	potential built in the p-type side
$\boldsymbol{J_n}$	electron current density
$\boldsymbol{J_p}$	hole current density
U_n	electron recombination rate
U_p	hole recombination rate
G_n	electron generation rate
G_p	hole generation rate
E_g	band gap
E_C	conduction band energy
E_V	valence band energy
E_F	Fermi level
E_{Fn}	quasi Fermi level for electrons
E_{Fp}	quasi Fermi level for holes
χ	Electron Affinity
D_n	electron diffusion coefficient
D_p	hole diffusion coefficient
I_{sc}	short circuit current
V_{oc}	open circuit voltage
N_V	Valence band Density of State
N_C	Conduction band Density of State
μ_n	Electron Mobility
μ_p	Hole Mobility

LIST OF ABBREVIATIONS

ZnO	Zinc Oxide
CdS	Cadmium Sulfide
LED	Light Emitting Diode
BFC	Enzymatic Bio Fuel Cell
MFC	Microbio Fuel Cell
TEM	Transmitting Electron Microscopy
SEM	Scanning Electron Microscopy
NW	Nanowire
NWPD	Nanowire Photodetector
MSM	Metal-Semiconductor-Metal
FEM	Finite Element Method
EQE	External Quantum Efficiency
PS	Polystyrene
FWHM	Full Width at Half Maximum
MWCNT	Multi-Wall Carbon Nanotubes
PBS	Phosphate Buffer Solution
CF	Carbon Fiber
PEDOT: PSS	Poly(3,4-ethylenedioxythiophene): Polystyrenesulfonate
PMMA	Poly (methyl methacrylate)
PDMS	Polydimethylsiloxane
PZT	Lead Zirconate Titanat
$BaTiO_3$	Barium Titanate
GaN	Gallium Nitride

InN	Indium Nitride
ZnS	Zinc Sulfide
TE	Thermionic Emission
HCP	Hexagonal Close Pack
LUMO	Lowest Unoccupied Molecular Orbit
HOMO	Highest Occupied Molecular Orbit

SUMMARY

The piezo-phototronics effect is the three way coupling of semiconductor properties, photonics and piezoelectricity in the same material. Research on piezo-phototronics effect has illustrated its application on various Zinc Oxide (ZnO) nanowire based devices, yet a systematical study with comprehensive theoretical model is still missing. Here we have designed experiments on wider variety of materials to investigate the mechanism of the piezo-phototronics effect, and then built up a theoretical model for more thorough understanding. Experimental results are shown for Cadmium Sulfide (CdS) photodetectors for visible light detection, inorganic/organic hybrid Light Emitting Diodes (LEDs) and LED arrays, and it is demonstrated that strain can significantly tune the performance of these optoelectronic devices. Theoretical methodologies are proposed for Metal-Semiconductor-Metal (MSM) structure and p-n junctions, including analytical solutions and Finite Element Method (FEM) simulations. For Schottky contacts in photodetectors, barrier height change is determined as the main reason for the effect, and an exponential relationship between applied external strain and the device current is discovered, and is qualitatively confirmed from experimental results. For p-n junctions in LEDs, change in size of depletion region under strain is credited for the current change, and a charge channel is predicted for large strain, which gives explanation for the observed gigantic enhancement of light emission efficiency in experiments.

CHAPTER 1

INTRODUCTION

The piezo-phototronics effect is a brand new research area. This effect is about the consequence of piezoelectric polarization on the generation, transport, separation and/or recombination of charge carriers at the junction, and is a three way coupling among piezoelectricity, semiconductor behavior and photon excitation, as shown in Figure 1.[1-2] Since year 2010, several experimental results have been reported to demonstrate the existence of the piezo-phototronics effect on ZnO based optoelectronics devices, including photocells, photodetectors and LEDs, in which the device performances and interaction with light are significantly changed by externally applied strain.[3-5] General explanations and illustrations were provided in these reports, yet a systemized fundamental model is still missing, and in order for better understanding of this phenomenon, further experiments devoting on the working mechanism is also desired. Thus, we carry out a study for more detailed design of the experiments, while also extending the application of piezo-phototronics on broader material system including other piezoelectric inorganic materials (CdS) and organic materials. The asymmetry of piezo-phototronics effect is discovered, and gigantic improvement of photodetection and photoemission is realized using the piezo-phototronics effect. We then build up analytical model and numerical simulation to explain the fundamental physics of piezo-phototronics effect, and the calculated result agrees to the experimental data very well.

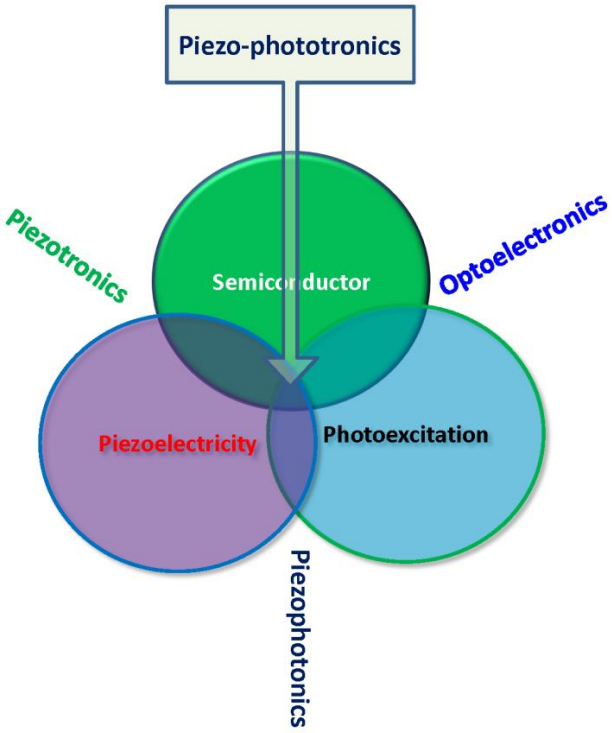

Figure 1 Schematic diagram showing the three-way coupling among piezoelectricity, photo excitation and semiconductor properties.

CHAPTER 2

SELF-POWERED PHOTODETECTORS AND PIEZO-PHOTOTRONICS EFFECT IN PHOTODETECTORS

Nanostructures are promising materials for photodetection, with advantages of high sensitivity, fast response speed, and low energy consumption,[6-10] which should give credit to the large surface-to-volume ratio and the presence of deep level surface trap states in NWs which prolongs the carrier lifetime, and the reduced dimensionality of the active area in NW devices which shortens the carrier transit time, resulting in substantial photoconductive gain.[11-14]

Previous reports have demonstrated the influence of piezo-phototronics effect on a ZnO based UV photodetector.[4] In such a study, an ultra-sensitive ZnO microwire based photodetector was fabricated by creating Schottky contacts on ends of the nanowire which connects into the testing circuit. With gradually increasing and uniformly applied strain on the nanowire, it was discovered that the current response under the same intensity of UV light illumination will change accordingly, and thus the sensitivity of the photodetector will increase to up to 530%. This study mainly focused on realization of enhancement on the device sensitivity, while the rules of piezo-phototronics effect was not yet clear and needed more elaboration.

Hereby we have extended this application to broader spectrum using the CdS NW, and emphasized on details for demonstrating rules and mechanism of piezo-phototronics effect. We prepared the CdS single-nanowire-based multicolor photodetector (NWPD) and assembled a self-powered system using bio fuel cells as the power source, as shown in Figure 2.

As a preparation step for application of piezo-phototronics effect, we have fabricated an ultrasensitive NWPD using a Cadmium Sulfide (CdS) nanowire with a

diameter of about 800 nm. The NWPD has a responsivity of more than 300 AW^{-1}, which is two to three orders of magnitude higher than that achieved using a conventional MSM photodetector, a detection limit as low as nW/cm^2, and low energy consumption.

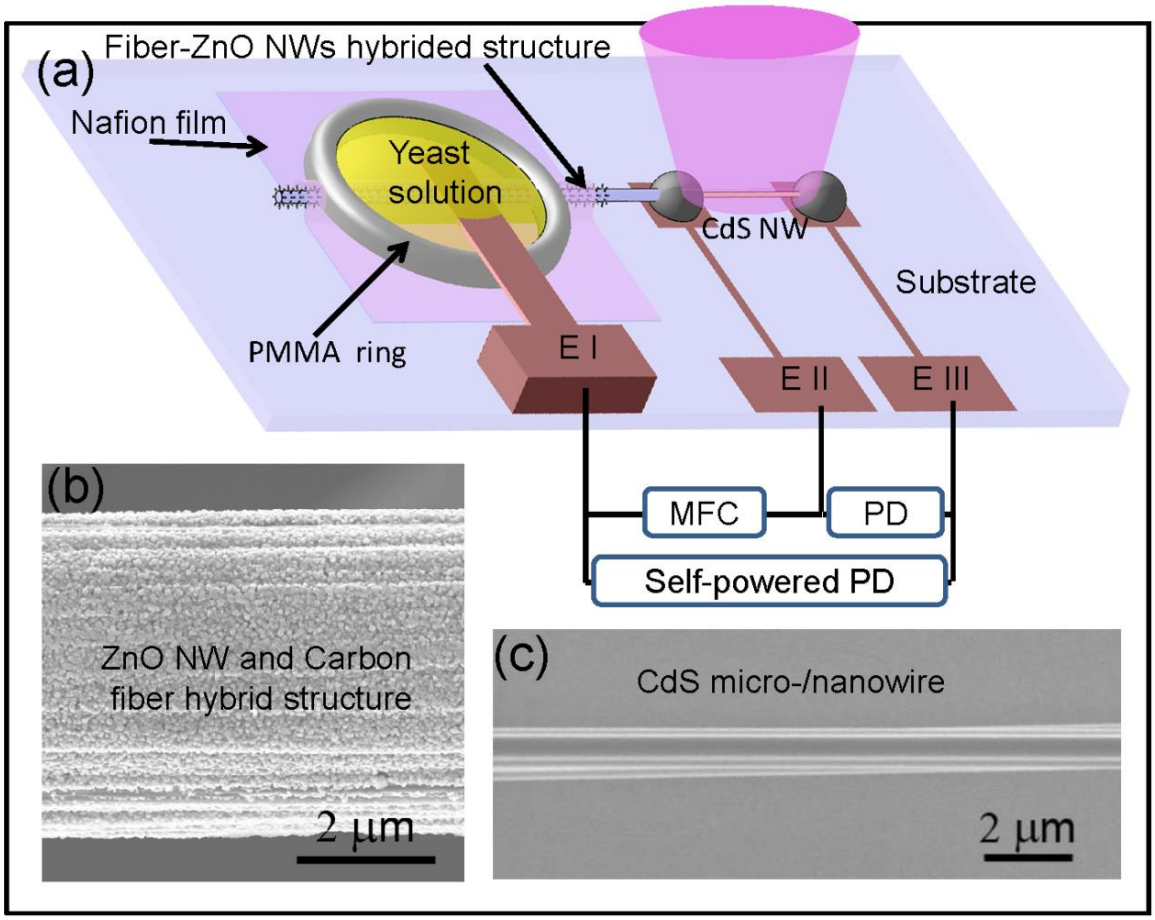

Figure 2 Experimental design of the self-powered photodetector system. (a) Schematic illustration of a self-powered nanosystem composed of a MFC (left-hand side) and a nanowire photodetector (right-hand side). (b) SEM image of a carbon fiber covered with densely packed ZnO NWs, which was used for fabricating the MFC. (c) SEM image of a CdS wire used for fabricating a photodetector.

Preparation of CdS Nanowire Photodetector

The CdS nanowires were synthesized using high-temperature thermal evaporation process, and are typically 0.8 to 3 micrometers in diameter and several hundreds of micrometers in length, as shown in the TEM image in Figure 3.[15] Transmission electron microscopy analysis of a single CdS nanowire and energy dispersive X-ray spectrometer show that the as-synthesized CdS NWs are single crystalline with Wurtzite structure, and growing along [0001] direction. A single CdS nanowire is placed on an elastic Kapton

(polyimide) substrate, with both ends bonded to the substrate and copper wires using silver paste to form Schottky contact. A device with Schottky contact has shown much higher sensitivity and much faster responsivity than a device with Ohmic contact for gas, chemical and bio-sensor.[16-17]

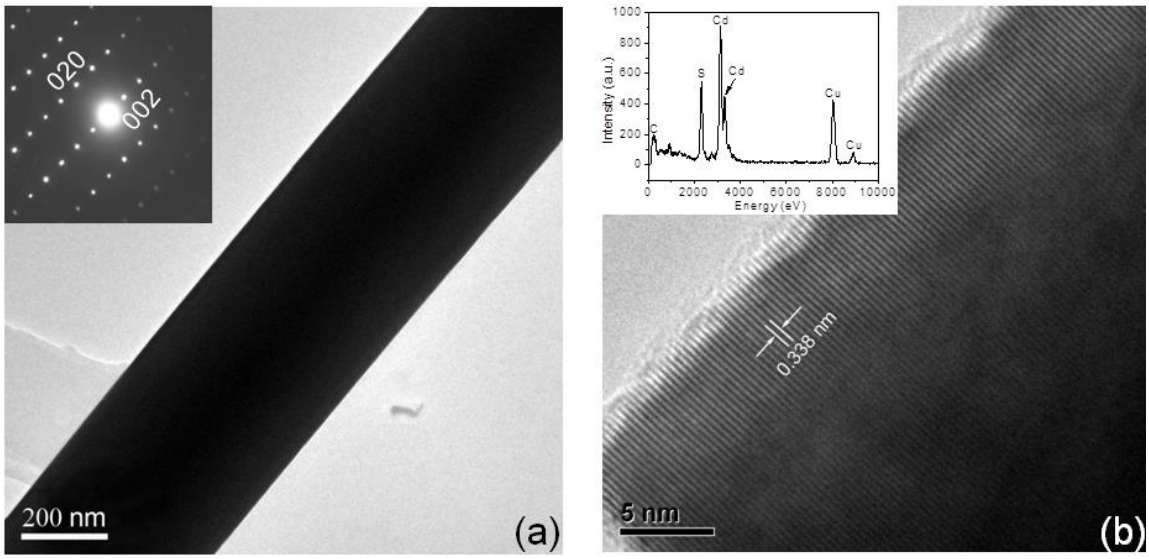

Figure 3 Characterization of the CdS NWs fabricated by thermal evaporation. (a) TEM image of a CdS nanowire, the inset is an electron diffraction pattern of the nanowire indicating its [0001] growth direction. (b) HRTEM image of the CdS nanowire, the inset is an EDX spectrum of the nanowire.

The results of photocurrent measurements performed on a single CdS NW device driven by an external voltage source are summarized in Figure 4. The origin of the photocurrent in Figure 4a arises from the photoconductivity of the CdS NW and the shrinkage of the depletion region of Schottky contact. The responsivity of the optical sensor is defined as18

$$R = \frac{I_{ph}}{P_{ill}} = \frac{\eta_{ext} q}{h\nu} \Gamma_G \qquad (1)$$

where R is the responsivity, I_{ph} photocurrent, P_{ill} the illumination power on the photodetector, η_{ext} the external quantum efficiency, q the electronic charge, h is Planck's constant, ν the frequency of the light, Γ_G the internal gain. The responsivity is observed to scale with the bias voltage, until it saturates at a high voltage as shown in Figure 4c. A

responsivity of 6 A/W can be achieved under -0.3 V bias, which is good enough for sub-μW/cm^2 light detection.

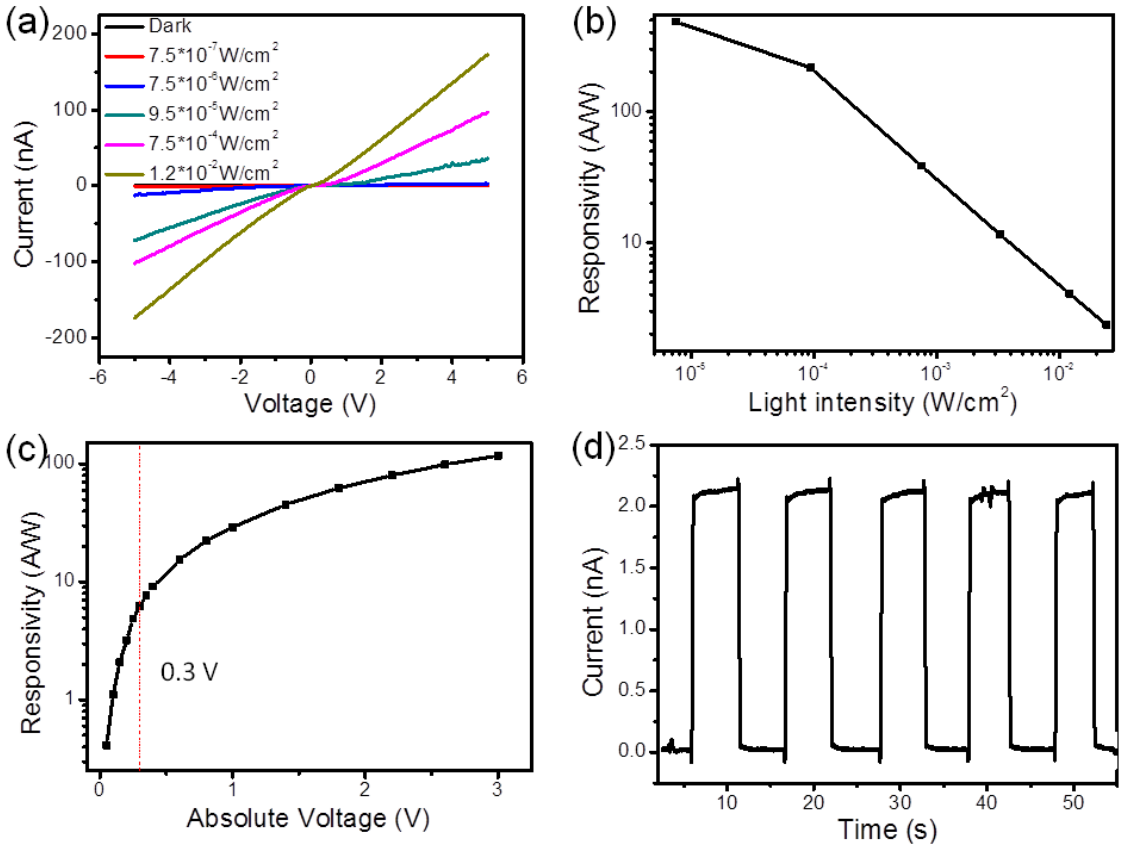

Figure 4 Characteristics of a single CdS NWPD for UV light detection. (a) I-V characteristics of a single CdS NWPD as a function of light intensity. (b) Derived photon responsivity relative to excitation intensity onto the CdS NW at an applied bias of -5 V. (c) Photon responsivity of the single NWPD as a function of biased voltage with excitation light intensity of 9.5×10^{-5} W/cm^2. (d) Time dependence of the current rise and decay under periodic illumination of UV light on the device at an applied bias of -0.3 V.

Fabrication and Performance of Bio Fuel Cells

We have then fabricated bio-fuel cells and used them to power up our NWPD as a self-powered photodetection system.

Enzymatic Bio Fuel Cells

An enzymatic Bio Fuel Cell (BFC) can be used to convert the chemical energy of glucose and oxygen in biofluid into electricity. The BFC configuration is illustrated in Figure 5c. The electrodes were patterned onto Kapton film and coated with multi-wall carbon nanotubes (MWCNT), followed by immobilization of glucose oxidase (GOx) and

laccase to form the anode and cathode, respectively. Glucose oxidase (GOx, from Aspergillus niger, type X-S) and laccase powder (from Trametes versicolor) were purchased from Sigma-Aldrich, multi-wall carbon nanotubes from Hanhwa Nanotech (diameter 3~9nm, purity>95%) and phosphate buffer solution (PBS, pH 7.0) from Fluka. All chemicals were used as received. Carbon nanotubes were dissolved in ethanol and sonicated for 1 h to form 2 g/L dispersion. A 4 g/L solution of GOx in phosphate buffer solution and a 4 g/L solution of laccase in phosphate buffer solution was prepared. The Kapton film with Au electrodes was prepared as described and then bleached and rinsed with deionized water before use. 2 μL of CNT dispersion was deposited onto both electrodes, and was rinsed with deionized water after drying. 2μL GOx solution was then deposited onto one of the CNT/Au electrodes to form the anode and 2 μL of laccase solution was deposited onto the other to form the cathode. The device was then stored under 4 ℃ for at least 4 hours before use. Prior to use, the electrodes were rinsed in pure PBS.

In addition to immobilizing the enzymes onto the electrodes, it has been shown that CNTs help promote the electron transfer between the enzymes and the electrodes.[19-21] The operating principle of the BFC is illustrated in Figure 5d. When the device is in contact with a biofluid that contains glucose (such as blood), the corresponding chemical processes occurring at the two electrodes is:[22] glucose is electro oxidized to gluconolactone at the anode: $Glucose \xrightarrow{GOx} Gluconolactone + 2H^+ + 2e^-$, and dissolved O_2 is electro-reduced to water at the cathode: $\frac{1}{2}O_2 + 2H^+ + 2e^- \xrightarrow{Laccase} H_2O$.

A voltage preamplifier (Stanford Research Systems, Model SR560) and a current preamplifier (Stanford Research Systems, Model SR560) were used to measure voltage and current output of the devices, respectively. A Labview program was used to monitor and record the measurement. A DC linear motor was used to provide strain for the nanogenerator measurement. The open-loop voltage and short-circuit current produced by

the BFC operating in Phosphate Buffer Solution (PBS, pH 7.0) with glucose concentrations of 0.5 mM, 5 mM, and 50 mM is presented in Figures 4a-b. Both the current and the voltage were found to increase with increasing glucose concentration. Human blood has a glucose concentration that fluctuates between ~ 4 to 6 mM and has a pH of 7.35-7.45.[22] At 5 mM the open loop voltage was found to be 50 mV and a short-circuit current of 11 nA. The power density of the BFC depends on load matching and was found to have a maximum at ~ 10 MΩ with a corresponding power density of ~ 2.2 nW/cm^2 and a current density of ~ 58 nA/cm^2.

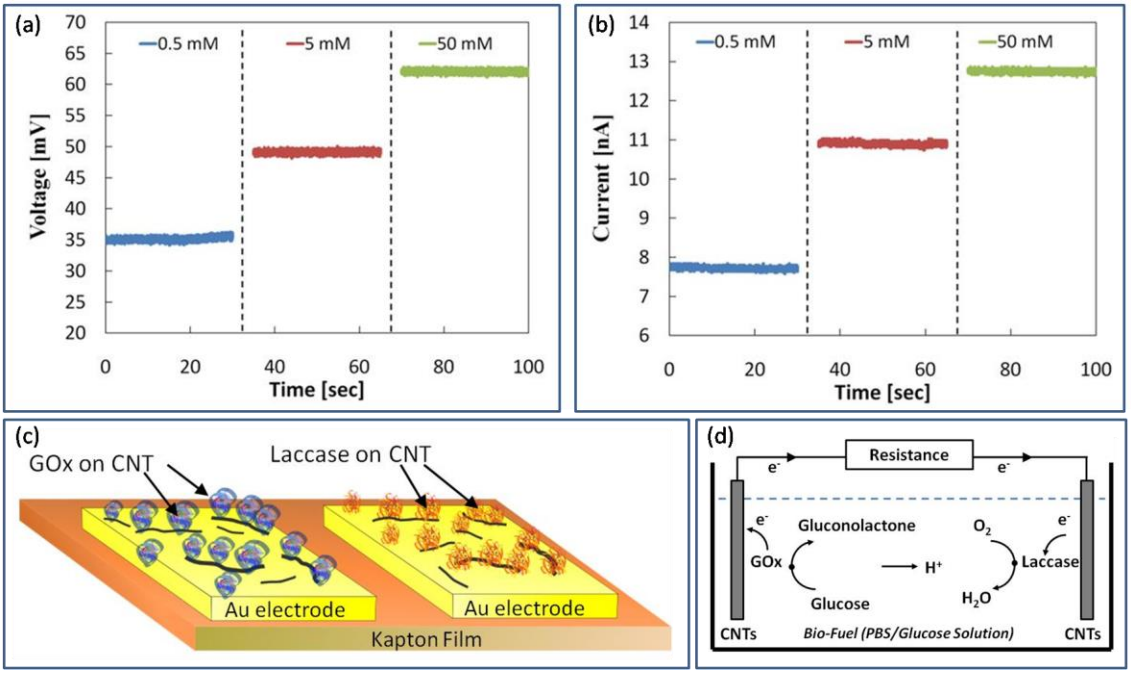

Figure 5 (a) Open-loop voltage and (b) short-circuit current of the BFC as a function of glucose concentration in PBS solution. (c) Schematic illustration of the fabricated BFC device. (d) Simplified schematic of the BFC operating mechanism.

The output achieved with BFC is not enough to power up a NWPD yet. The highest theoretical voltage that may be obtained from a GOx/laccase based BFC is dictated by thermodynamics and is ~ 1 V.[22] To obtain this voltage, various factors need to be optimized, but the most important one is the enzyme surface interactions. By cross-linking or "wiring" the immobilized redox enzymes to a redox hydrogel, the output of the BFC can be further optimized in the future.[23-25] In addition, multiple BFCs could be

integrated together to boost power output. However, such improvement can be time consuming and cost ineffective, and will cause device instability. Thus, we have turned to a cheaper and steadier device with higher output and potential for environmental application, the Microbio Fuel Cell.

Microbio Fuel Cell

The working principle of a Microbio Fuel Cell (MFC) is presented in Figure 6a. Glucose was decomposed by yeast to form CO_2 and electron proton pairs. The electrons produced in the micro-organism solution are transferred to the anode and subsequently through an external circuit to the cathode, whilst protons or phosphate anions migrate from anode to the cathode through the separator membrane. At the cathode, H^+ and electron recombine with oxygen molecule to form H_2O molecule. A separator is an important part to ensure an efficient and sustainable operation of an MFC. The paradox of ion transfer and oxygen permeation is the major constraint for most separators in MFC. For example, a porous membrane will increase ion transfer, but suffers from high oxygen permeation. Oxygen permeation will lower the bioelectrocatalytic activity of the anode microorganisms, thus lower the efficiency of the MFC. The hybrid structure MFC has solved this paradox using a hybridized structure of carbon fiber-ZnO NWs, which has increased ion transfer and avoided oxygen permeation simultaneously. As shown in Figure 6a, a porous membrane rather than smooth film will form on the ZnO NWs coated carbon fiber (CF) when spin coating Nafion film, which allows various charged or neutral species to pass through efficiently and leads to easier ion transfer. On the other hand, oxygen is adsorbed and immobilized on the ZnO NW surface, as represented schematically by blue balls on the ZnO nanowire surfaces. Thus, the oxygen permeation through the membrane is reduced. These two advantages may allow the hybrid structured MFC to give a higher output.

For the device fabrication, ZnO NWs around CFs were fabricated by physical vapor deposition processes. A CF was used as the cathode for the MFC. The ZnO NWs at one end of the CF were etched by HCl solution, and the end was connected with electrode by silver paste. A thin film of Nafion was carefully spun coated onto the fiber-NWs hybrid structure, which will be used as anion exchange membrane separator. The separator was bound with cathode (CF) here to form a separator cathode assembly for the MFC. This design greatly simplified reactor configuration and reduced operation costs of MFCs by adopting passive air flow. Then a millimeter-diameter micro-pool was constructed by squeezing poly(methyl methacrylate) (PMMA) solution onto the Nafion film to form a ring shaped "micro-pool" (the inner diameter about 1 - 5 mm, the thickness about 1 mm, the volume less than 20 μL). The yeast solution for MFC was made by the following procedure: 0.2 g glucose was mixed with 10 ml phosphate buffer (Na_2HPO_4 and NaH_2PO_4) with pH = 7.0; and 0.2 g dry Baker's yeast was mixed with 10 ml distilled water. Then the two kinds of solution were mixed together in commensurable volume to form a solution used for MFC. A pipette was used to suck up the solution and drop it into the micro-pool.

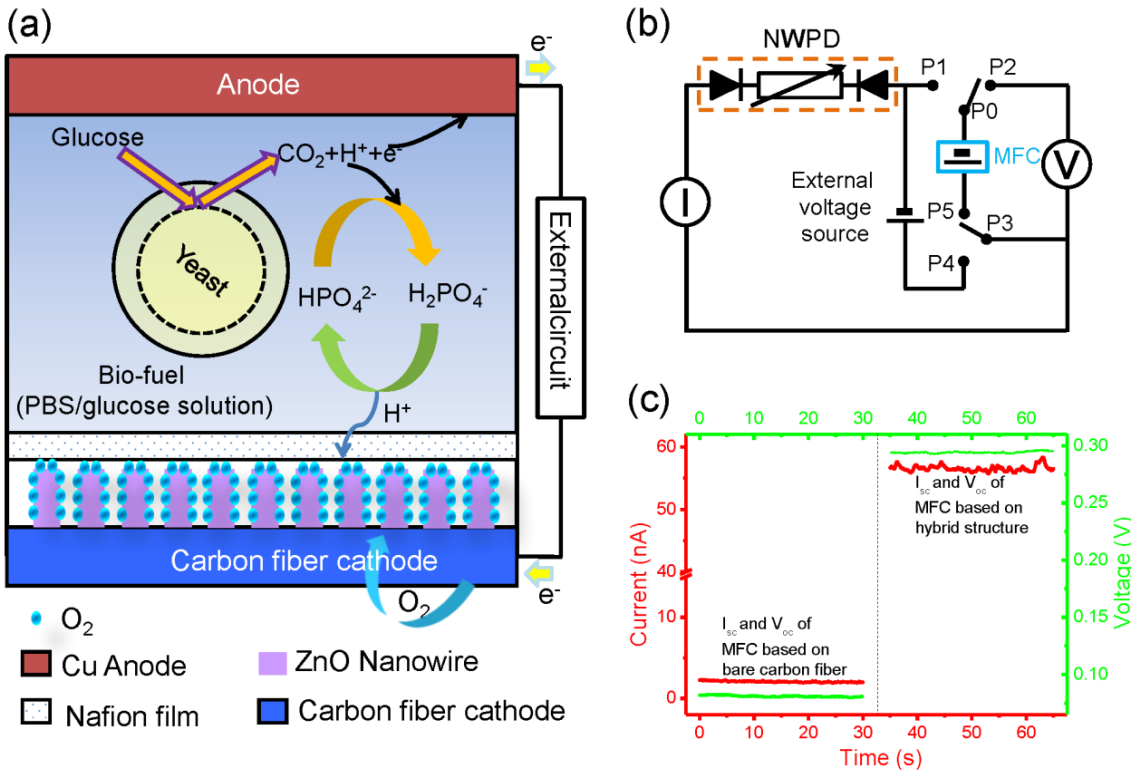

Figure 6 Principle and performance of MFC and the working circuit of the self-powered nanosystem. (a) Principle of a MFC based on fiber-NW hybrid structure (see text). (b) Circuit diagram used for integrating a single hybrid structured MFC and a NWPD. The diodes at the two ends of the device represent the local Schottky contacts between CdS and metal electrodes. (c) Open-loop voltage (green line) and short-circuit current (red line) of the hybrid structured MFC and bare CF based MFC.

The performance of the MFC is characterized by measuring the short circuit current I_{sc} and open circuit voltage V_{oc}. Once a drop of yeast solution was dripped into the micro-pool, the MFC started to generate a DC output. A typical output of the MFC is shown in Figure. 6c, the I_{sc} is about 56 nA, the V_{oc} is about 295 mV, and the corresponding power density is about 30 W/m^2 of electrode geometry area, while the performance reported for μL and sub-μL scale MFC is limited by low volumetric power density due to its high internal resistance. The performance of our MFC is among the best of its kind reported so far.

We found that the ZnO NWs around the CF play an important role for the enhanced performance of our micro-size MFC. For a comparison purpose, a MFC was fabricated using a bare CF without ZnO NWs following the same procedures as for the hybrid structured MSC. The corresponding I_{sc} was about 2 nA, and the V_{oc} was about 80

mV, and the corresponding power density was 0.29 W/m^2 of electrode geometry area, which are two orders of magnitude lower than that of the hybrid structured MFC. Thus, the significant enhancement in performance of our hybrid structured MFC may originate from the increased surface area and the absorption of oxygen at ZnO NW surfaces.

Self-Powered Photodetection

Next, it is demonstrated that this NWPD can be successfully powered by a MFC to form a self-powered system. The experiments were carried out in the following manner. For the self-powered nanosystem, there are three electrodes pre-fabricated in the system before measuring the performance of the device, as shown in Figure 1. Electrode I was placed on the top surface of the yeast solution, electrode II was the joint point of the CF and CdS NW, and electrode III was connected at the other end of the CdS NW. Monochromatic UV (centered at 372 nm), blue (centered at 486 nm), or green light (centered at 548 nm) illuminated on the CdS nanowire to test the performance of the device, which was focused by a 10X microscope objective with a 17.5 mm work distance. He-Ne 632.8-nm-wavelength laser was used as red light to excite the CdS NW. A Newport 92250A-1000 solar simulator was used as the solar light. The optical power density impinging on the nanowire photodetector was varied by means of neutral density filters. The illumination density was determined by a thermopile power meter (Newport 818P-001-12). Electrical measurements were obtained on a precise electrical measurement system built with Stanford low noise current preamplifier, low-noise voltage preamplifier and function & arbitrary waveform generator. Dark current noise for the nanosystem was carried out in an electrically shielded and optically sealed probe station, to minimize the environmental noise.

As shown in Figure 7, the self-powered nanosystem shows an excellent response to solar light with a response time of ~30 ms and decaying time of ~40 ms. When light irradiation on the CdS NW is turned off, the system leakage current is less than 1 fA. The

on-off cycles have remarkable repeatability. The self-powered nanosystem can detect light down to nW/cm^2 level (fW light illuminating onto the NW).

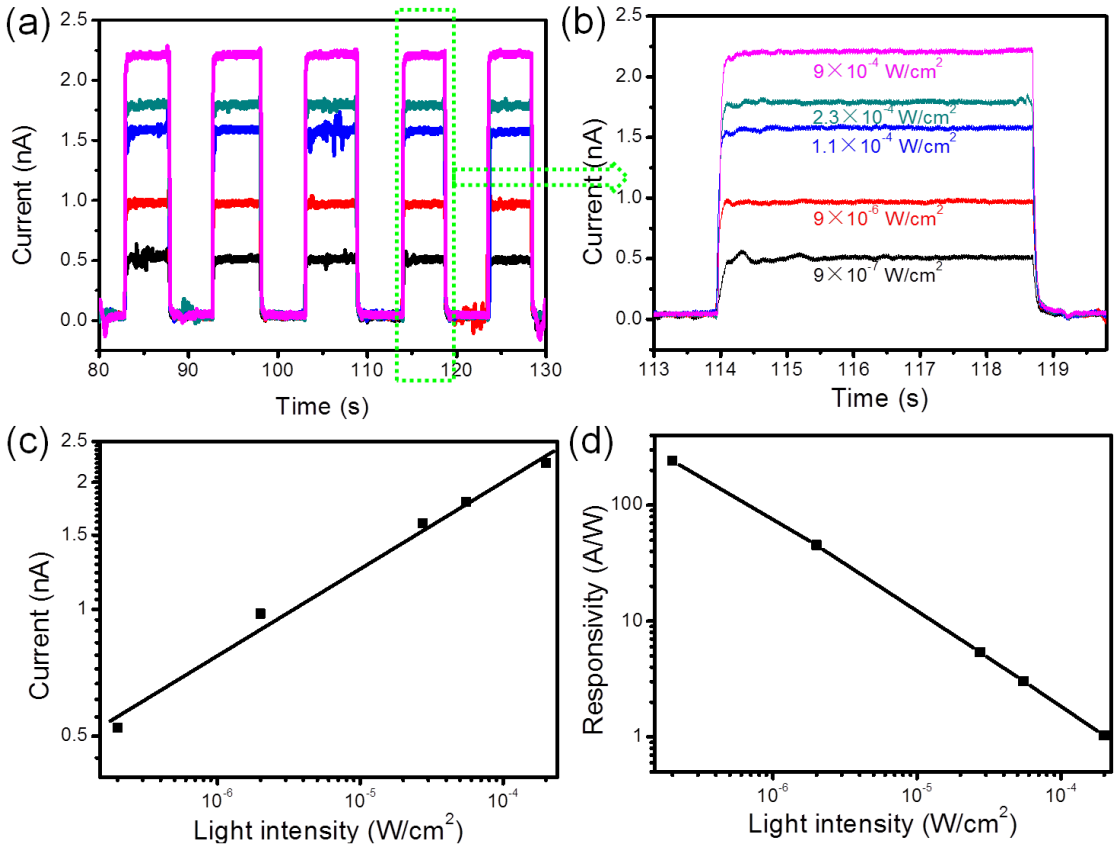

Figure 7 Detection of solar light by a self-powered CdS NWPD that was driven by a single hybrid structured MFC. (a) Repeatable responses to different excitation light intensities: from black to pink the light intensity varied from 9×10^{-7}, 9×10^{-6}, 1.1×10^{-4}, 2.3×10^{-4}, and 9×10^{-4} W/cm^2. There is no external voltage source applied in the system. (b) The photocurrent rise and decay process, plotted in the same color code with (a). The rise time is about 30 ms, the decay time is about 40 ms. (c) Measured current through the sensor as a function of the illuminating light intensity. (d) Derived photon responsivity as a function of the solar light intensity shed on the CdS NW.

Besides solar light detection, our self-powered photodetector can be used to detect multicolor light ranging from red light to UV light. Once the UV light with an intensity of about 1.6×10^{-4} W/cm^2 shed on the CdS NW, the system current immediately increased to 1.4 nA. The responsivity for UV, blue, and green light with intensity of 2.3 nW/cm^2 (equal to 25 fW light illumination onto the NW) of the system were 1180, 344 and 332 A/W, respectively, which is two to three orders of magnitude higher than that received using a nitride based MSM photodetector[26] and silicon NW photodetector. The intensity dependence of the measured current for UV, blue and green light is plotted in Figure 8,

which increased linearly with the optical power and showed no saturation at high power levels, offering a large dynamic range from nW/cm^2 to mW/cm^2. Photodetection for red light is plotted in Figure 9. Spectral photo response of the self-powered nanosystem showed that the responsivity depended on light wavelength. The responsivity for UV, blue and green light was much higher than that for red light since the photon energy of red light is less than the band gap of CdS, and thus the generation of electron-hole pairs was less efficient.

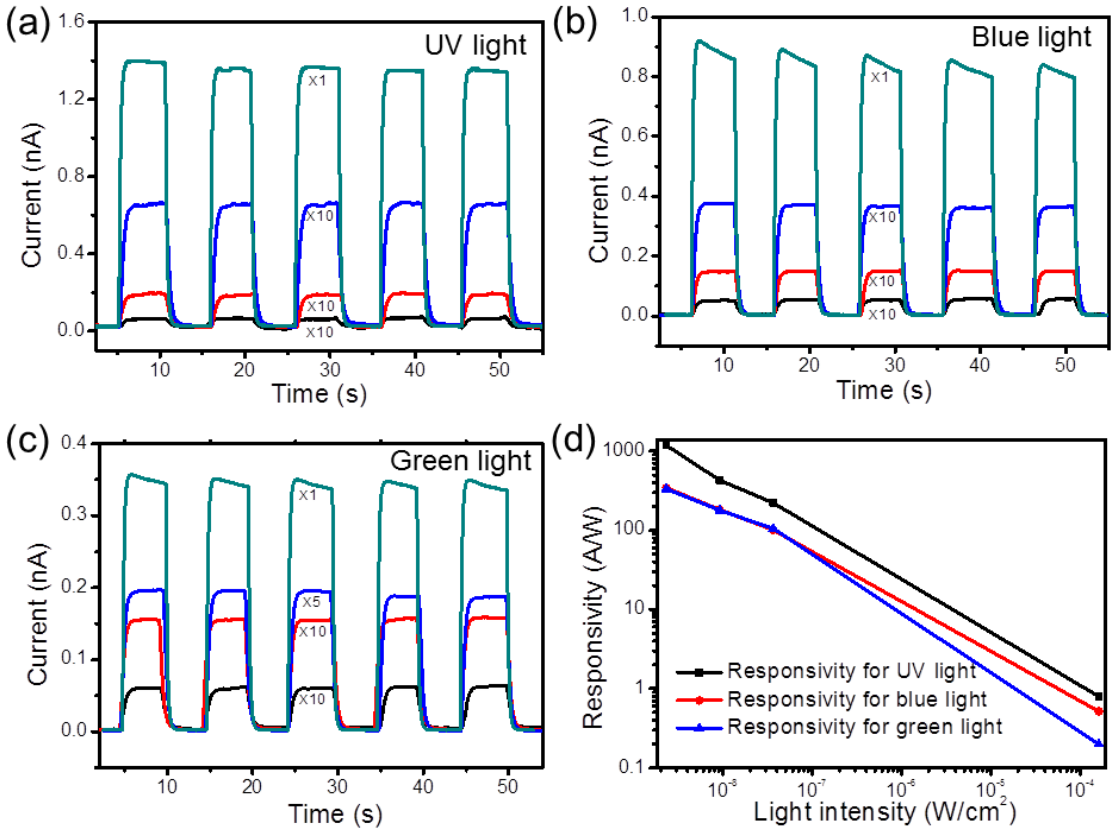

Figure 8 UV-blue-green multicolor detections by a single CdS NWPD driven by a single hybrid structured MFC. (a) UV light (372 nm). (b) blue light (486 nm). (c) green light (548 nm). From black line to green line, light intensity varied from 2.3×10^{-9}, 9.1×10^{-9}, 3.6×10^{-8}, and 1.6×10^{-4} W/cm^2, respectively. The corresponding light power illuminated onto the CdS wire was about 25 fW, 100 fW, 400 fW and 1.7 nW, respectively. (d) Derived photon responsivities as a function of the excitation intensity on the CdS NW that was illuminated by UV, blue and green light, respectively.

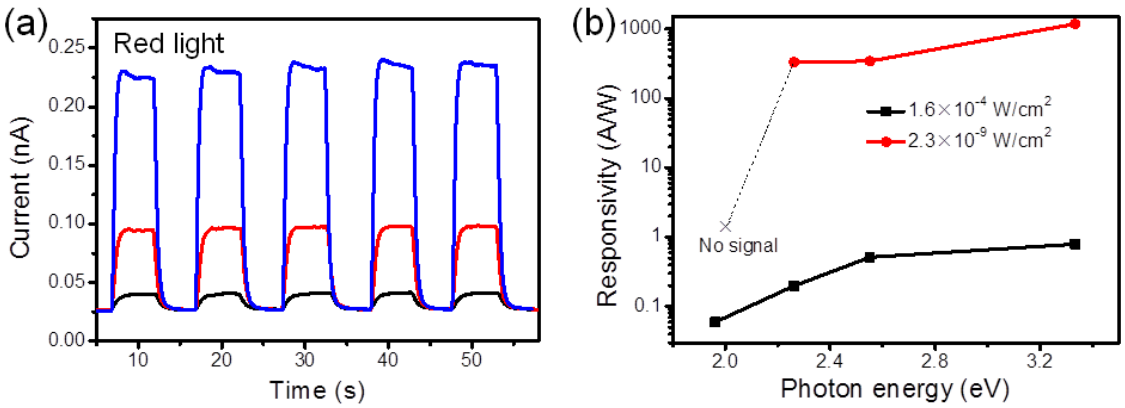

Figure 9 Red light detection and spectral response of the self-powered NWPD. (a) Red light (632 nm wavelength) detection using the single CdS NWPD driven by a single hybrid structure MFC. From black line to blue line, light intensity is 1.0×10^{-4} W/cm^2, 2.3×10^{-4} W/cm^2, 1.2×10^{-2} W/cm^2, respectively. (b) Spectral photoresponse of the self-powered NWPD.

The figure 10 shows the NEP of the photodetector, i.e. the minimum radiant power that a detector can distinguish from noise. It is difficult to measure the signal when the signal-to-noise ratio is unity. So it is customary to make the measurement at a high level of incident radiation and calculate the NEP from the following equation:[27]

$$NEP = \frac{I_n}{R\sqrt{\Delta f}} \qquad (2)$$

where I_n is root mean square value of the noise current at output of photodetector, and Δf is the electrical bandwidth in Hz. Frequency dependent responsivity and the noise equivalent power of the self-powered nanosystem are shown in Figure 10a and 10b, respectively. Surprisingly, we found that the noise current of the NWPD driven by a hybridized MFC is about one order of magnitude lower than that driven by an external voltage provided by a function generator due to the small size and good stability of the microscale MFC (Figure 10b inset image). The NEP of the self-powered NWPD for detection of UV, blue and green light at 10 Hz is about 5.0×10^{-18}, 1.5×10^{-17} and 2.8×10^{-17} W Hz$^{-1/2}$, respectively, two to three orders lower than previous reports,[7-8, 27-28] which means that our self-powered NWPD has the potential to detect light down to sub-fW level. Another figure of merit for photodetector is the linear dynamic range (typically

quoted in dB) which is estimated by $20\log(\frac{I_{ph}}{I_n})$,[27] where I_{ph} is the photocurrent measured at light intensity of 1 mW/cm^2. Figure 8d shows the responsivity versus light intensity for UV, blue and green light, respectively. All of the linear dynamic range for three colors light is more than 100 dB, which is close to that of the high performance Si and polymer detectors. [27] The ultra-small size, large linear dynamic range and ultra-sensitivity of our self-powered photodetector may be used for implanted devices for in-situ monitoring the optical intensity during in-situ optical medical treatment.[29-31]

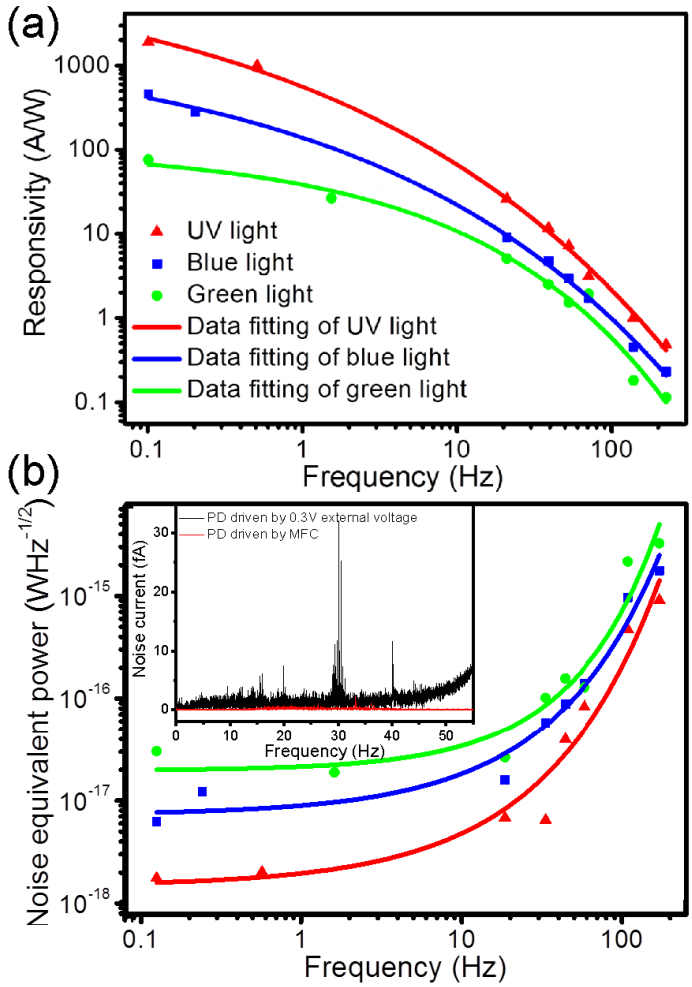

Figure 10 Frequency dependent performance of the self-powered multicolor NWPD. (a) Responsivity versus modulation frequency under 2.3×10^{-9} W/cm^2 UV, blue and green light illumination. (b) NEP versus modulation frequency of the self-powered NWPD for different color light detection. The inset image shows the noise current of the NWPD driven by a hybridized MFC and by a 0.3 V external voltage source provided through a function generator at a bandwidth of 90 Hz (from 10 to 100 Hz).

Demonstration of Piezo-Phototronics effect on CdS NWPD

For the next step, CdS NWPD is applied with mechanical strain through the experimental setup shown in Figure 11, and the photo response of the NWPD is tested under various mechanical strains for various device configurations.

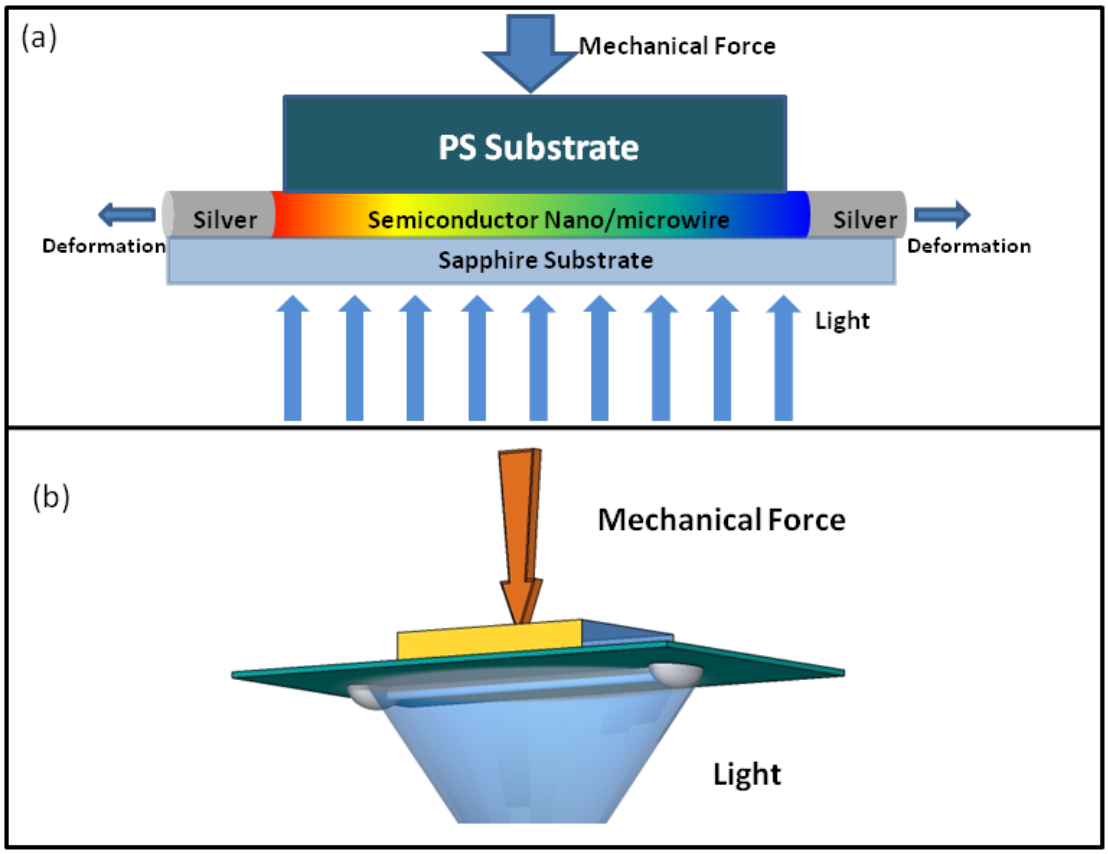

Figure 11 Illustration of the photodetection experiment with strain applied on the NW. (a) Two-dimensional illustration. (b) Three-dimensional illustration.

Here we have studied two kinds of typical MSM photodetectors: one with a Schottky contact on one end of the metal-CdS nanowire junction and an Ohmic contact on the other end; another with two Schottky contacts on both ends. Figure 11 is the result for a single Schottky contact photodetector. As shown in Figure 12b, under increasing strain, the current decreases. Thus, the device configuration and direction of the c-axis is as shown in the inset of Figure 12b. In Figure 12d, illumination power is kept at 6.4 $\times 10^{-6}$ W/cm^2, the change of responsivity R with applied strain for the photodetector is

calculated. Responsivity is the measurement of degree of sensitivity $R = \frac{I_{ph}}{P_{ill}}$, where P_{ill} is the measured light intensity. We can see that the responsivity in this case decreases with positive strain.

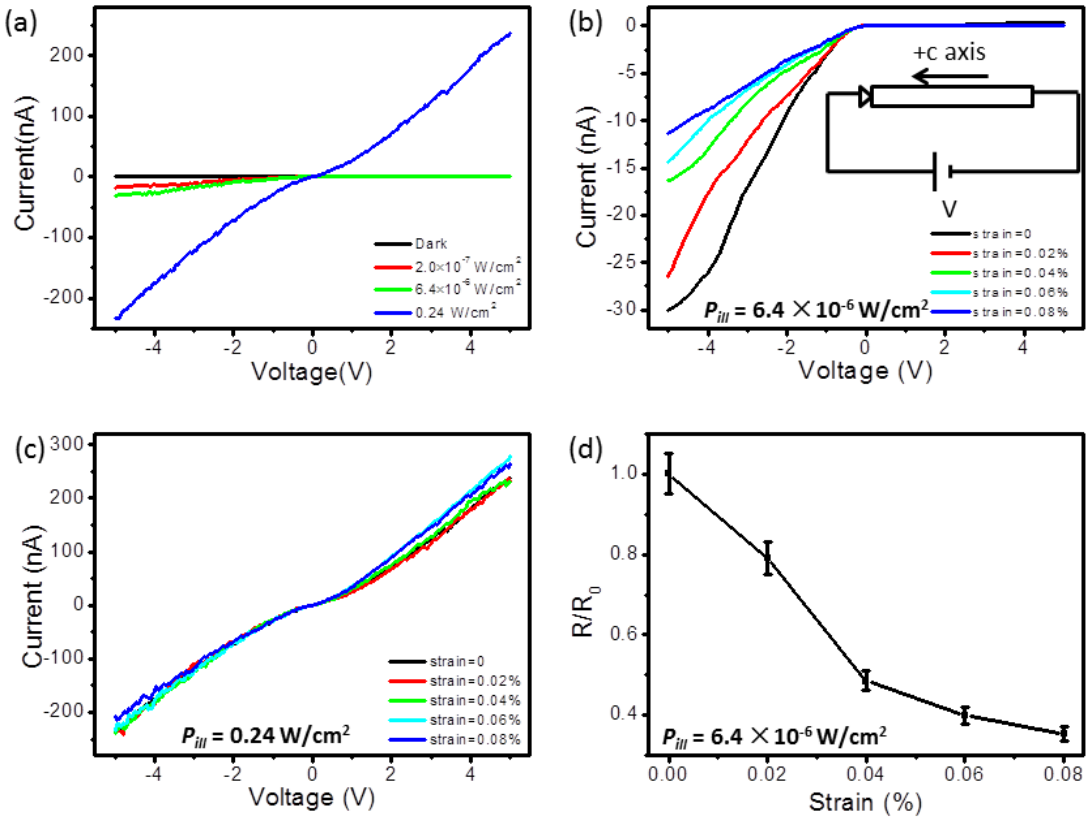

Figure 12 Experimental results for a CdS nanowire MSM photodetector with a single Schottky contact. Light illumination with monochromic blue light centered at 486 nm. (a) Current-voltage characteristic under different illumination power. Inset it dark current without strain. (b) Current-voltage characteristic under different strain when illumination power is 6.4 $\times 10^{-6}$ W/cm^2. Inset is the configuration of device and direction of forward bias. (c) Current-voltage characteristic under different strains when illumination power is 0.24 W/cm^2. (d) Calculated relative responsivity under various applied strain when illumination power is 6.4 $\times 10^{-6}$ W/cm^2. R_0 is set as responsivity under zero strain for this illumination power.

Figure 13 is the result for a double Schottky contact photodetector. As shown in Figure 13b, the change in I-V characteristic with applied strain is in the way exactly as predicted by the theoretical model: while the current under forward bias increases with applied strain, under reverse bias the current decreases with it.

In both Figure 12c and 13c, we can see that, with an increase in illumination power, the strain effects are not as significant as that at lower illumination power. The

piezo-phototronic effect can help enhance sensitivity of the detection at low light intensity, but does not necessarily have significant effect for strong light intensity. In practice, the detection of low intensity light is practically desired.

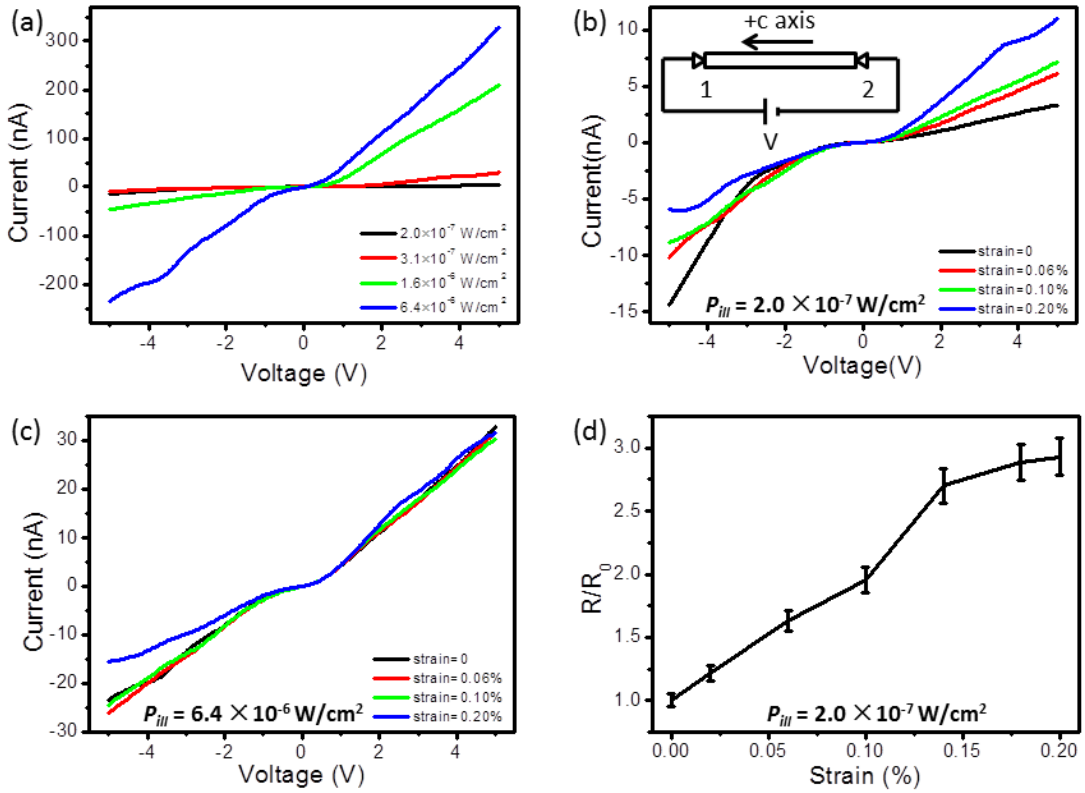

Figure 13 Experimental results for a CdS nanowire MSM photodetector with double Schottky contacts. Light illumination with monochromic blue light centered at 486 nm. (a) Current-voltage characteristic under different illumination power. (b) Current-voltage characteristic under different strain when illumination power is 2.0 $\times 10^{-7}$ W/cm^2. Inset is the configuration of device and direction of forward bias. Inset is the configuration of device and direction of forward bias. (c) Current-voltage characteristic under different strains when illumination power is 6.4 $\times 10^{-6}$ W/cm^2. (d) Calculated relative responsivity under various applied strain when illumination power is 2.0 $\times 10^{-7}$ W/cm^2. R_0 is set as responsivity under zero strain for this illumination power.

CHAPTER 3

PIEZO-PHOTOTRONICS EFFECT IN LEDS

Nanowire based Light Emitting Diodes (LEDs) have attracted considerable attention from as they offer interesting possibilities in photonics.[32] The demonstration of piezo-phototronics effect on NW LEDs was first demonstrated on a structure composed of single n-type ZnO NW on p-type GaN thin film. Here we expand the effect from inorganic to polymer, and from single NW structure to NW arrays.

Piezo-Phototronics Effect in Organic/Inorganic Hybridized LEDs

ZnO NW inorganic/organic hybrid UV LEDs not only combine the high flexibility of polymers with the structural and chemical stability of inorganic NWs, but also have higher light extraction efficiency than thin film structures. However, the external quantum efficiency of UV LED based on ZnO nanostructures has been limited by a lack of efficient methods to achieve a balance between electron contributed current and hole contributed current that reduces the non-radiative recombination at interface. We have applied the piezo-phototronics effect and have largely enhanced the efficiency of a hybridized LED (HyLED) made of a ZnO nanowire/p-polymer structure, by trimming the electron current to match the hole current and increasing the localized hole density near the interface through a carrier channel created by piezoelectric polarization charges on the ZnO side. The external efficiency of the hybrid LED was enhanced by at least a factor of two after applying a proper strain, reaching 5.92%.

ZnO NWs have become a subject of great scientific and technological interests because of their unique semiconductor, photonic and piezoelectric properties for a range of applications in photonics, electronics, sensors and energy harvesting.[1, 33-36] With a direct band gap of about 3.30eV, large excitonic binding energy about 60 meV as well as

large refractive index, ZnO NWs are among the most promising materials for the next generation optoelectronic devices operating in ultraviolet (UV) region, such as light emitting diodes (LEDs), photodetectors and solar cells. [4, 11, 37-42] Nanoscale hybrid materials containing organic as well as inorganic components have attracted considerable attention in recent years, as they promise new properties that may not easily be available from conventional materials. For example, the hybrid structure devices can combine the high flexibility of polymers with the structural and chemical stability of inorganic nanostructures, compatible with low cost, polymer printing techniques.[43-44] To date, inorganic/organic hybrid LEDs with n-type ZnO nanostructures have been realized in many different systems, including poly(3,4-ethylenedioxythiophene): polystyrenesulfonate (PEDOT:PSS), p-type N, N'-diphenyl-N, N'-bis(1-naphthyl) - 1, 1'-biphenyl-4, 4='-diamine (α-NPD), N,N'-di(naphth-2-yl)-N, N′-diphenyl-benzidine (NPB), poly N-vinylcarbazole (PVK), poly (2-methoxy-5-(2-ethylhexyloxy)-1, 4-phenylenevinylene) (MEH-PPV) and poly(3-methylthiophene) (PMT) etc.[45-51] However, UV LEDs based on ZnO nanostructures have shown relatively low EQE due to the difficulties in achieving current balance between electrons and holes and high non-radiative recombination induced by surface defects.[52] In most of the reports, there was no data about conversion efficiency or EQE of ZnO NW/organic hybrid LED.

The quantum efficiency of LEDs, which is the photons emitted per electron injected, depends on the balance of the currents and therefore on the charge injection rates at the cathode and anode interfaces. If one sign of carrier dominates over the other, most of the majority carriers across from one electrode to the other do not experience recombination, which contributes to the current instead of photon emission. Therefore, it becomes critical to achieve the best possible current balance in the fabrication of LEDs such as using suitable electrode materials, insulator as carrier blocking layers and post-treatment of organic materials.[52-54] In previous work, it is already demonstrated that

piezo-phototronic effect can enhance the external efficiency of an inorganic LED fabricated using a single ZnO micro-/nanowire on a GaN substrate.[5]

In our experiment, the piezo-phototronic effect in Schottky contact and p-n junctions are effectively utilized to enhance the external efficiency of the HyLED using a single ZnO nanowire/p-polymer core-shell structure. The emission light intensity and EQE has been enhanced to 190% and 230% after applying a -0.008% compressive strain when the c-axis of ZnO nanowire is pointing away from the p-polymer. Meanwhile, when the c-axis of ZnO nanowire is pointing toward the p-polymer, the emission light intensity and EQE has been enhanced to 230% and 370% after applying a 0.017% tensile strain. The asymmetric change in current under forward and reverse bias indicates that the performance enhancement is attributed to piezo-phototronic effect. This work not only proves that the applications of the piezo-phototronic effect can extend from rigid inorganic to flexible organic materials, but also offers a more compact and lower cost device structure as well as a very simple fabrication process for high efficient hybrid UV LED. Numerical simulations fit well to the experimental results, and the physical mechanism is proposed with considering the big difference of organic materials and inorganic materials.

The experiments were carried out based on the following design. The device structure is schematically shown in Figure 15a. The HyLED was fabricated by coating a thin layer of p-polymer on ZnO NW under microscope. The ZnO micro/nanowires were synthesized by a high-temperature thermal evaporation process.[15] A Kapton film (20mm ×8mm ×0.5mm) covered by Ni/Au (20/50 nm) film or ITO film electrodes with a well-controlled gap was used as the substrate. A single ZnO NW was picked up from the substrates and the free end was dipped in a small PEDOT: PSS droplet to form ZnO NW/p-polymer core-shell structure. SEM images (Figures 15b and 15d) show that a thin and smooth PEDOT: PSS film (about 10 nm) is coated on ZnO NW uniformly, indicating an excellent contact and good interface forming between these two materials. The ZnO

NW/p-polymer core-shell nanostructure was placed across the gap with a close contact with electrode film (Figures 15a and 16). A transparent polystyrene (PS) tape was used to cover and fix the nanowire.

The experimental setup is shown schematically in Figure 14. In order to avoid short circuit, the shell should be terminated inter the gap of two Au electrodes. The measurement system is built under a microscope. A 3D stage was used to fix the device and another 3D stage was used to introduce strain. The Kapton substrate was bent up and down under different direction force. Mainly axial compressive or tensile strain was introduced depending on the bending direction of the substrate considering the relative size of the wire and the substrate. The strain was quantified by the maximum deflection of the free end of the substrate.[55]

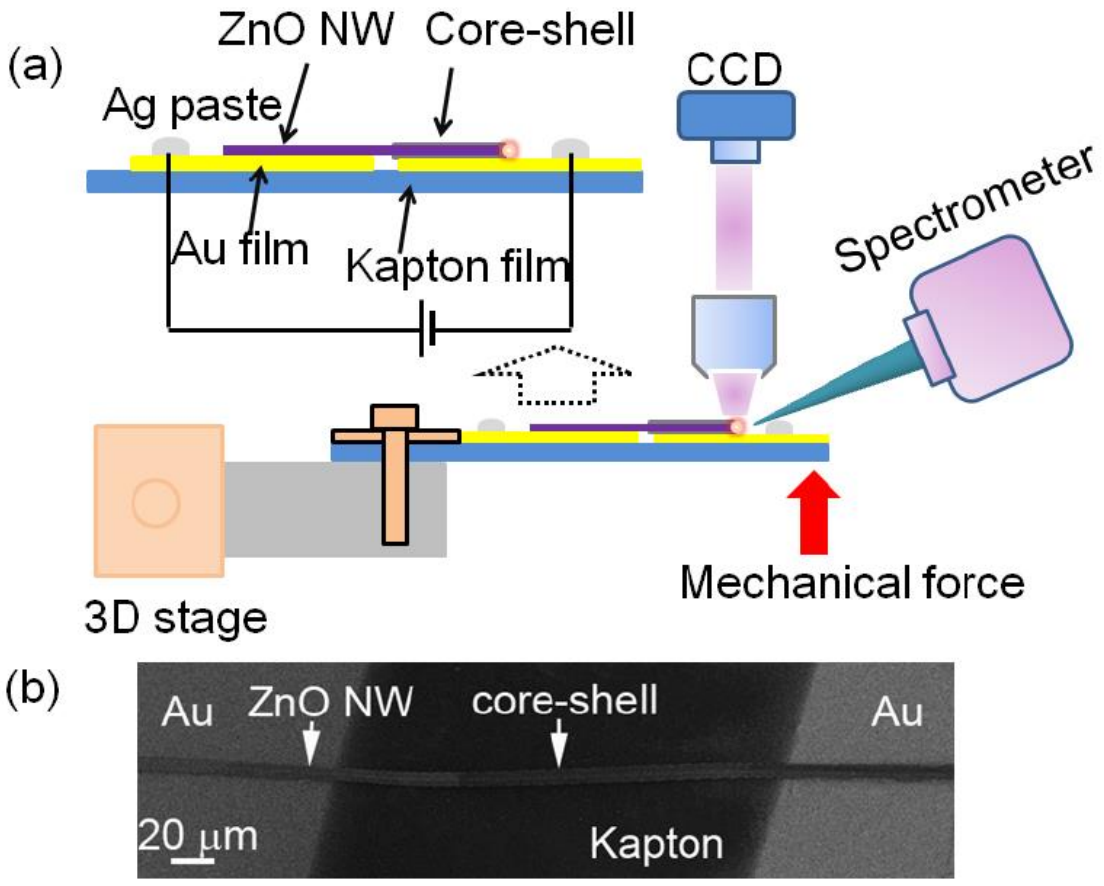

Figure 14 Measurement system and device structure of the HyLED. (a) Schematic diagram of the measurement system for characterizing the performance of a ZnO NW/p-polymer core-shell structure LED under applied strain. (b) SEM image of a ZnO NW/p-polymer LED device structure.

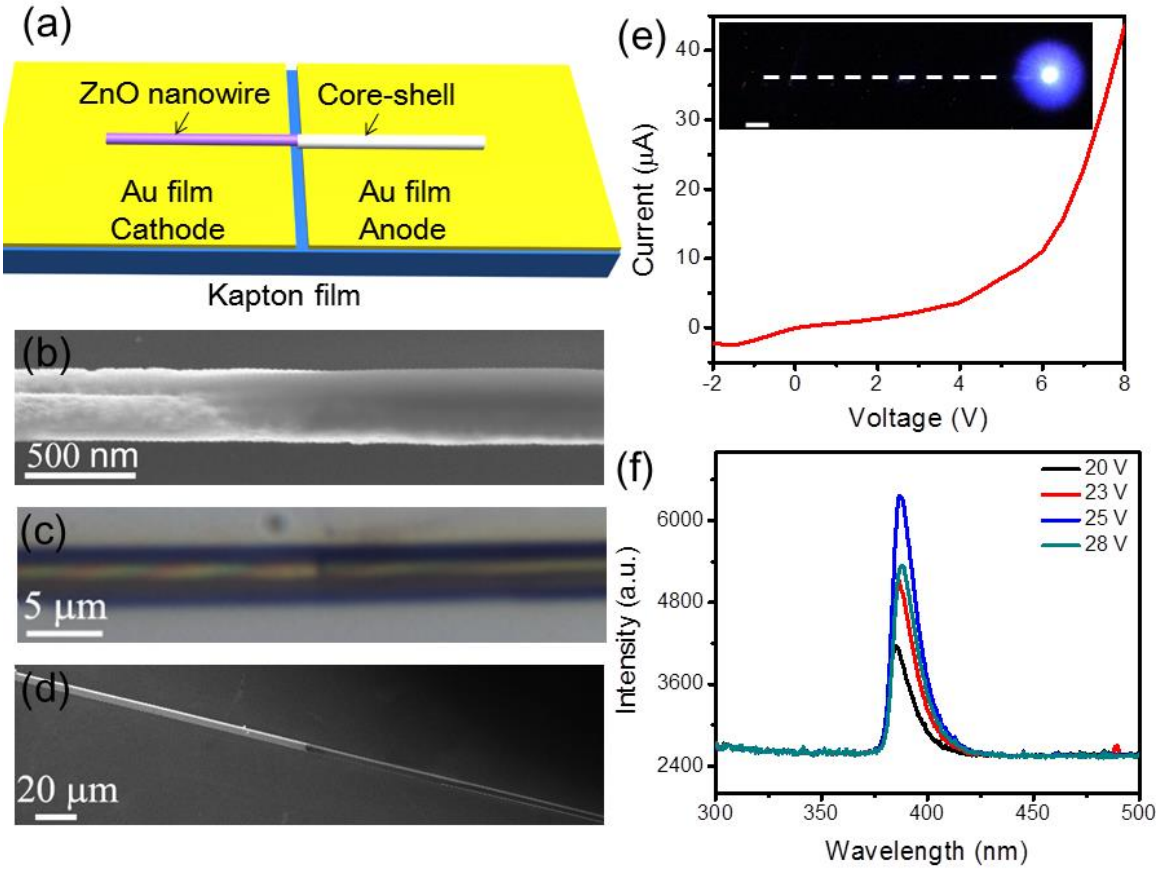

Figure 15 Characterization of ZnO NW/p-polymer core-shell UV LED. (a) Schematic diagram of device structure. (b) SEM image of a ZnO NW/PEDOT:PSS core shell structure. (c, d) OM and SEM image of a ZnO microwire/PEDOT:PSS core-shell structure. (e) *I-V* curve of the LED, the inset is a CCD image of the LED at 25 V biasing voltage, the dashed line represents the physical location of the ZnO NW/p-polymer core-shell structure, scale bar 10 μm. (f) EL spectrum as a function of the forward biased voltage.

The *I-V* characteristics and dependence of the emission intensity on applied voltage of an as-fabricated LED without applying additional strain are presented in Figures 15e and 15f. Strong UV emission peak is obviously observed while visible broad-band luminescence also exists in some devices. The UV emission is centered at a wavelength of 387 nm and has a full width at half maximum (FWHM) of 13 nm, ascribed to bound-exciton or vacancy-related transitions in ZnO NWs.[56-57] The EQE and power conversion efficiency of an as-fabricated single ZnO nanowire inorganic/organic core-shell LED before applying strain was measured to be about 1.6% and 0.5% respectively. It is found that the relative high efficiency benefits from the core-shell structure and the Au electrodes (Figure 16 and Table 1). Among the three device structures in Figure 16,

the hybrid structure LED based on nanoscale core-shell structure with Au electrodes has the highest EQE, followed by the core-shell structure with ITO electrodes, the hybrid structure based on ZnO NW and ITO film shows the lowest efficiency. Compared with the conventional hybrid structure LED based on ZnO NW and spun-coating PEDOT:PSS film, the hybrid structure LED based on nanoscale core-shell structure could offer better contact and more uniform interface (Figures 15b to 15d), which is good for achieving high efficiency LED. Furthermore, defects on ZnO NW surface may be passivated by a p-polymer, resulting in decrease of the non-radiation recombination and increasing in light output.

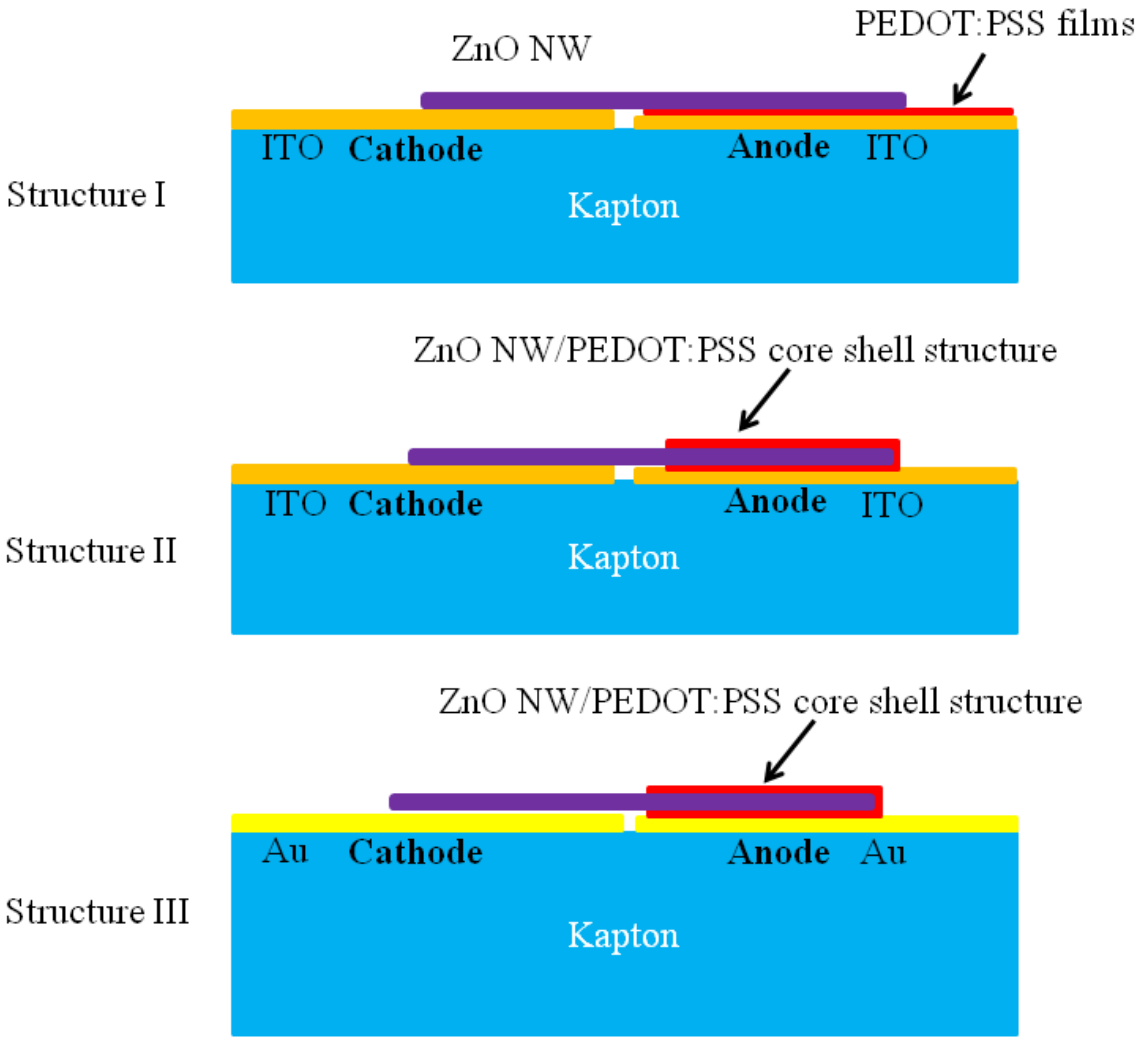

Figure 16 Detailed side views of the three different kinds of device structures.

Table 1 Room temperature external quantum efficiency of three different structured LED

Structure	electrodes	pn junction structure	Number of measured devices	yield	Energy conversion efficiency	External quantum efficiency
I	ITO	NW/film	20	10%	~0.01%	~0.03%
II	ITO	Core-shell	40	50%	~0.1%	~0.32%
III	Au	Core-shell	100	50%	~0.5%	~1.60%

An important factor influencing the conversion efficiency of LED is the current balance including charge injection rate and carrier mobility of electrons and holes. In our device, electrons are the majority carrier and recombination is limited by hole injection because of the large barrier height for hole transport. As shown in Figure 17, there is a 0.6 eV barrier for electron injection from Au into ZnO's conduction band and a 1.0eV barrier between the ZnO conduction band and the PEDOT LUMO (lowest unoccupied molecular orbit). The hole injection barrier is 0.1 eV between the Au and PEDOT:PSS HOMO (highest occupied molecular orbit), 2.7 eV for electron injection from PEDOT: PSS HOMO into ZnO valance band. Thus the total barriers for electrons and holes when using Au as electrodes are 1.6 eV and 2.8 eV, respectively. As a comparison, if using ITO as electrodes, the total barriers for electrons and holes are 1.0 eV and 3.2 eV, respectively. Compared with ITO electrodes, Au electrodes will balance the electron current and hole current more easily by increasing the barrier for electron transport and reducing that for holes simultaneously. The results are similar to that utilizing a thin oxide layer as carrier blocking layer to improve the performance of organic LED.[52] The experimental results are consistent with the above analysis. In Table 1, the external efficiency of the ZnO NW/p-polymer core shell structure is about 1.6% and 0.3% for structure using Au electrodes and ITO electrodes, respectively.

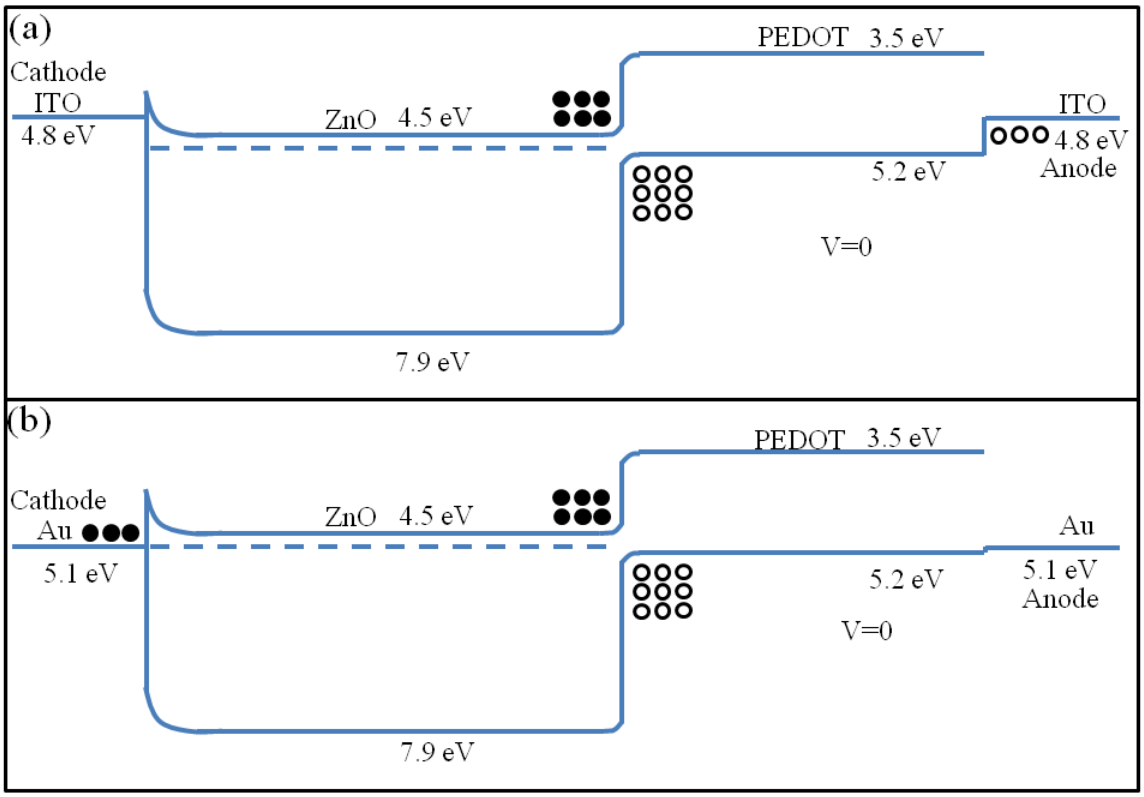

Figure 17 (a, b) Schematic energy band diagram of the LED without applied strain in thermal equilibrium using ITO and Au as electrodes, respectively.

In the next step, piezoelectricity is applied on the device and proved to be capable of significantly enhancing the EQE, which is a complete new approach to improve the performance of inorganic/organic hybrid LED. In the experiment, the output light intensity is measured by spectrometer and CCD, which characterizes the optical power in a relative manner. The main focus is on the relative change of the output light intensity as well as the quantum efficiency under different strain. The change of quantum efficiency is derived by analyzing the output light intensity and current under the applied strain. The data for investigating the influence of strain on light intensity and spectrum are recorded using a fiber optical spectrometer. The integration of peak spectrum is considered as the relative emission light intensity. The data for studying the strain effect are recorded using a CCD. The relative light output intensity is extracted by analyzing the brightness of the image. The actual external efficiency of the single ZnO NW/p-polymer core-shell

structure LED is quantified by adopting the method used in previous work. The output light is coupled by a pure silica fiber with diameter of 100 μm and guided into the spectrometer. We calculated the optical power received by the spectrometer by analyzing the integrated intensity. Table 1 shows the room temperature external quantum efficiency of three different structured LED shown in Figure 16. Under a fixed forward bias above the turn-on threshold voltage, the current decreases step-by-step when applied a variable strain from 0.003% tensile strain to -0.008% compressive strain. An important characteristic of the current change is the asymmetric change of *I-V* curve at negative and positive bias (Figures 18d and 18e): while the current under forward bias decreases with applied strain, under reverse bias the current increases. It indicates that the change is mainly due to genuine piezo-phototronic effect that is from the polarized piezopotential. Other factors induced by external strain such as piezoresistance, band shifting or contact area change will induce symmetric change at both ends of the nanowire regardless the polarity of the applied voltage.[5]

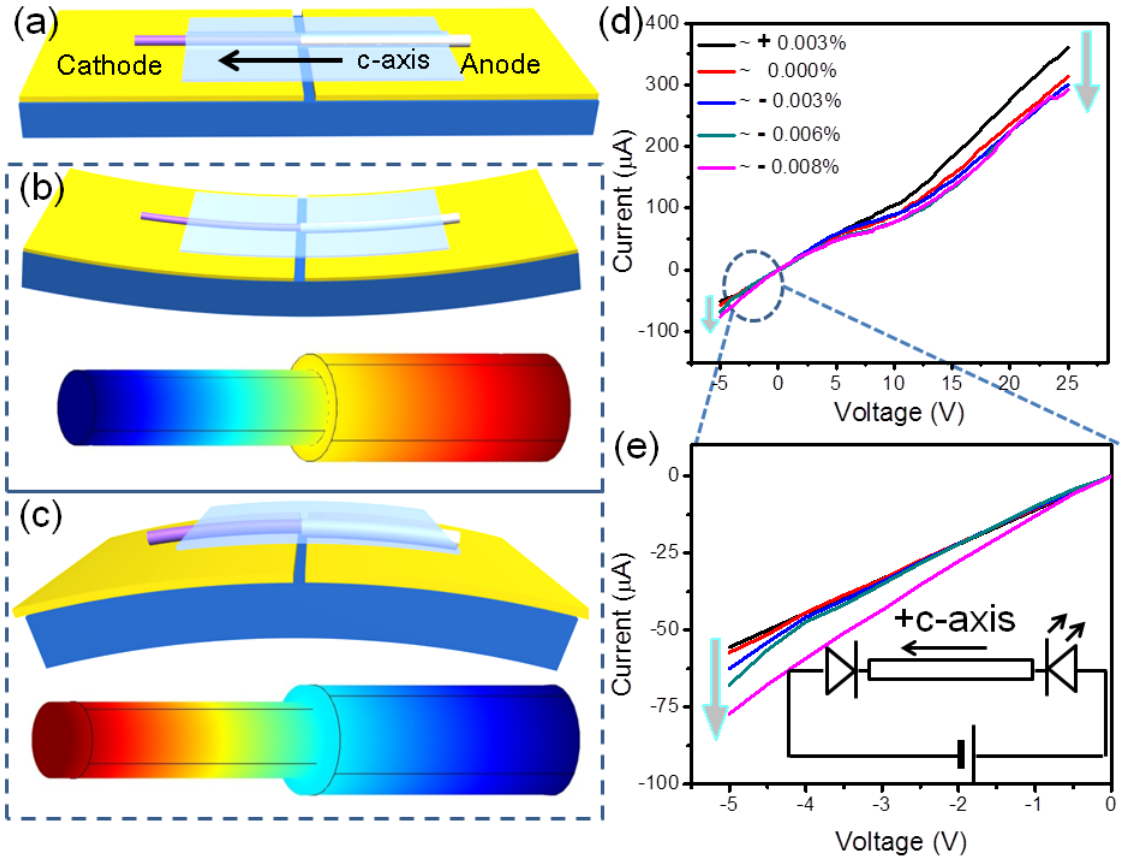

Figure 18 Electric characteristics of a ZnO NW/p-polymer core-shell UV LED with c-axis pointing away from p-polymer under different strain. (a) Schematic diagram of the device. (b) Simulated piezopotential distributions in the ZnO NW under compressive strain. (c) Simulated piezopotential distributions in the ZnO NW under tensile strain. The diameter and length used for calculation are 1 μm and 10 μm, respectively. The compressive and tensile strain are about -2% and 2%, respectively. The conductivity of the ZnO is ignored in the simulation for simplicity. (d) I-V characteristics of the device at forward bias with the variation of the applied strain. (e) The enlarged picture of I-V curve circled by dashed line. Insets are the configuration of the device and direction of forward bias.

Importantly, from experimental results shown in Figure 15, the light emission should be localized near the end surface of the nanowire, where ZnO is in contact with PEDOT: PSS. The following analysis is based on the light emission at the end polar surface of the nanowire instead of the side surface. The change of the current with strain can be determined by[55]

$$\ln\left(\frac{I_\varepsilon}{I_0}\right) = \Delta\Psi \;/\; kT \qquad (3)$$

Since piezopotential has a linear relationship with the external strain, we can expect that the change of current $\frac{I_\varepsilon}{I_0}$ have an exponential relationship with the external strain, as shown in Figure 19a.

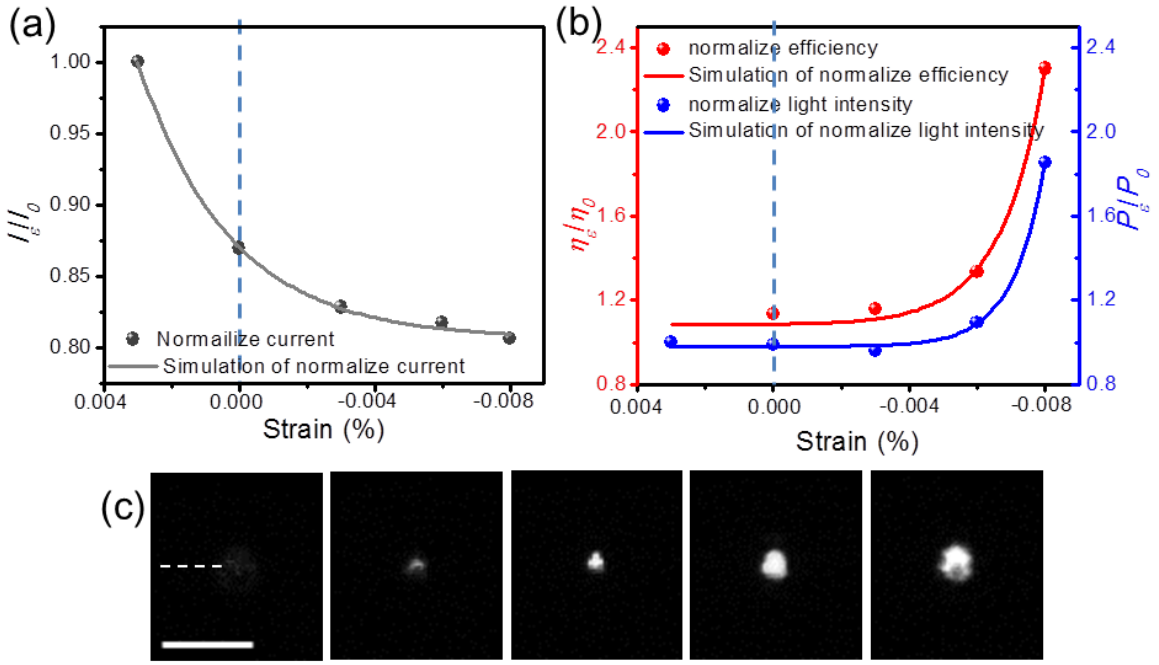

Figure 19 Enhancement of emission light intensity and conversion efficiency of a ZnO NW/p-polymer core-shell UV LED with c-axis pointing away from p-polymer under different strain at 25 V biasing voltage. (a) Change in relative injection current I_ε/I_0 under different strain. (b) Change in relative light intensity P_ε/P_0 and external efficiency η_ε/η_0 under different strain. (c) CCD images recorded from the emitting end of a packaged single wire LED under different applied strain, the dashed line represents the position of ZnO NW/p-polymer core-shell structure, scale bar 10 μm.

Surprisingly, in the experiments, the light emission intensity is increased step-by-step while the forward current is decreased gradually (Figure 19b) when we apply a compressive strain. The light output enhancement can be directly observed in optical images recorded by a CCD. The change of the light intensity increases exponentially with the increased compressive strain (Figure 19b). The ocular sensitivity of the human eye is very low at the ultraviolet wavelength and the silicon diode used to measure luminance is not sensitive at 380 nm either. Thus the normally used luminous efficiencies in terms of Cd/A or lm/W are not good measures of UV LED. Better measures of the performance are the EQE and overall emission efficiency (also called power-conversion efficiency).

The overall emission efficiency η is defined as the ratio of the emitted optical power P to the applied electrical power,

$$\eta = \frac{P}{I \times V} = \eta_{ext} \frac{h\nu}{eV} \tag{4}$$

where P is the emitted optical power, I is the current, V is the applied voltage, and η_{ext} is the EQE, the ratio of the externally produced photon flux to the injected electron flux, thus we have

$$\eta_{ext} = \frac{P / h\nu}{I / e} \tag{5}$$

The light intensity under -0.008% compressive strain was enhanced to 190%, while the current was decreased to 81% of the original value. The light output increase and current decrease will dramatically enhance the EQE and conversion efficiency according to equations (4) and (5). The efficiency is enhanced to 230% after applying -0.008% compressive strain.

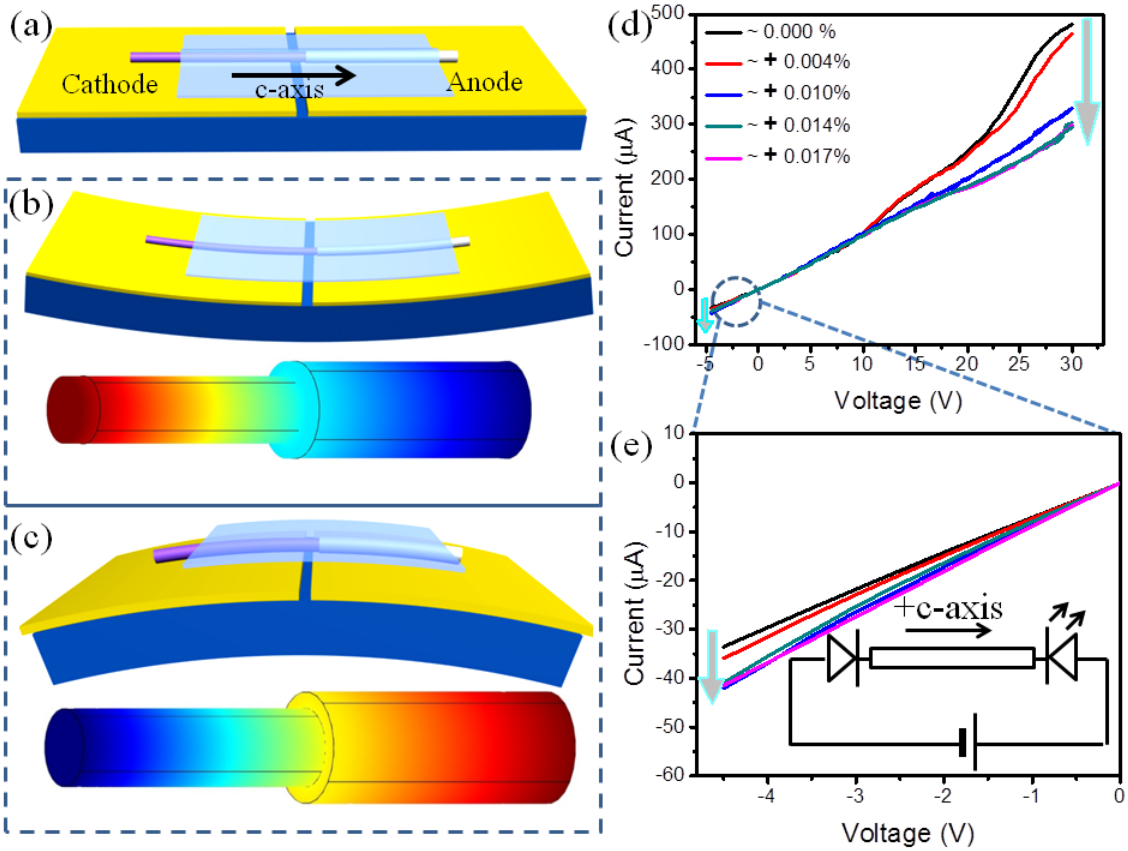

Figure 20 Electric characteristics of a ZnO NW/p-polymer core-shell UV LED with c-axis pointing toward p-polymer. (a) Schematic diagram of the device. (b) Simulated piezopotential distributions in the ZnO NW under compressive strain. (c) Simulated piezopotential distributions in the ZnO NW under tensile strain. The diameter and length used for calculation are 1 μm and 10 μm, respectively. The compressive and tensile stresses are about -2% and 2%, respectively. The conductivity of the ZnO is ignored in the simulation for simplicity. (d) *I-V* characteristics of the device at forward bias with the variation of the applied strain. (e) The enlarged picture of *I-V* curve circled by dashed line. Insets are the configuration of the device and direction of forward bias.

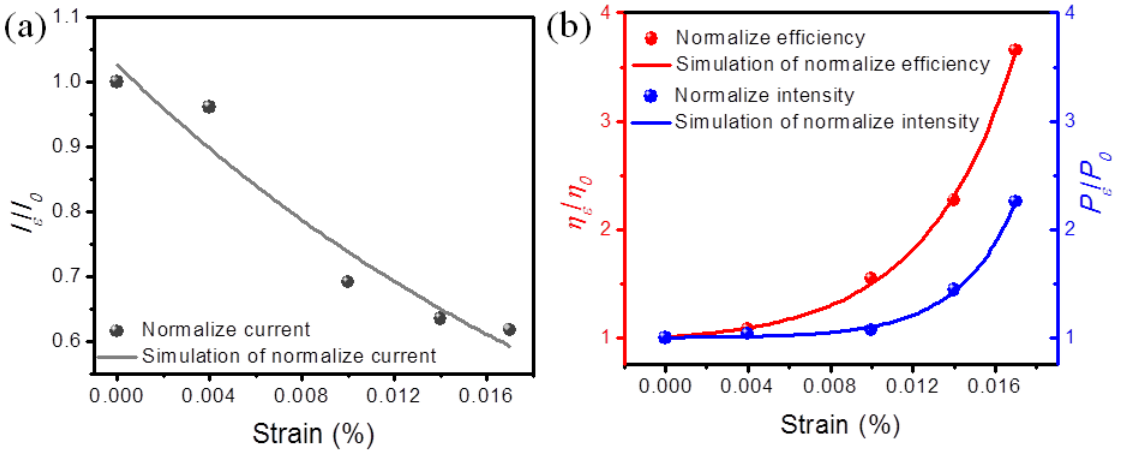

Figure 21 Enhancement of emission light intensity and conversion efficiency of a ZnO NW/p-polymer core-shell UV LED with c-axis pointing to p-polymer under different strain. (a) Change in relative injection current *I(ε)/I(0)* under different strain. (b) Change in relative light intensity *P(ε)/P(0)* and external efficiency *η(ε)/ η(0)* under different strain.

In the experiments, some of the devices show opposite trend of change, which means that the light output and efficiency is enhanced under tensile strain (Figure 20 and 21). The emission light intensity and EQE have been enhanced to 230% and 370%, respectively, after applying a 0.017% tensile strain. And the absolute conversion efficiency and the EQE of the LED are 1.85% and 5.92%, respectively, after applying a tensile strain, which is comparable to that of inorganic pn junction LED and quantum-well enhanced nanowire LED.[58] The opposite change in two different types of NWs is attributed to the switching in signs/polarity of the piezoptential, which depends on the orientation of the c axis of the ZnO wire. Statistically, we have 50% chance in experiments to have the ZnO wire oriented along the *c* or *–c* direction (the axial direction of the wires). It is noted that in two different kinds of devices, the *I-V* curve change is both asymmetric for negative and positive bias, which agrees to the photodetetion experiments in the previous chapter. In experiments, the LED operation voltage is randomly chosen (above the turn-on threshold voltage) and the enhancement is calculated at the chosen applied voltages. We found that the enhanced effect has no dependence on applied voltage from testing on more than 10 devices. This indicates that the enhancement occurs across a range where the forward bias is larger than the turn-on threshold voltage, which can also be observed from the similar trend of current change at different voltage after applying strain.

The gigantic efficiency enhancement by piezo-phototronic effect in ZnO nanowire/p-polymer core-shell structure LED can be explained schematically in Figure 24. The schematic band diagram of the device without strain shows that the barrier for hole injection from PEDOT: PSS into ZnO is approximately 3 eV (Figure 17). Therefore, extremely high barrier height for holes injection makes the recombination being largely limited by hole injection and transport. The efficiency is low as majority electrons flow through without sufficient recombination with holes. When the device is applied with proper strain under forward bias, a distinctive change will be induced on the band

diagram due to the piezoelectric effect, which is proved to enhance the electron-hole recombination and efficiency significantly. Numerical simulation of the piezopotential distribution on the ZnO NW/p-polymer core-shell structure shows that a negative potential drop is created along +*c* axis of ZnO NW when the NW is under c-axis compressive strain, while an oppositely distributed piezopotential is created when the NW is under *c*-axis tensile strain, assuming that ZnO NW is intrinsic or low-doping. If the *c*-axis of the ZnO NW is pointing away from the p-polymer and the ZnO NW under *c*-axis compressive strain, the effect of the local negative piezopotential at the cathode will increase the Schottky barrier height, while the local positive piezopotential near the pn junction (at the end of ZnO NW where light is illuminated as shown in Figure 15) will introduce a carrier channel owing to a dip at the local band, with considering the narrow distribution width of the piezoelectric polarization charges. The formation of the dip can be derived from the coupling of Poisson equation and piezoelectric constitutive equation.[5] Theoretical analysis of current distribution show that the current mainly flows through the adjacent of the illuminating end face of NW. Thus overlapping of localized piezo-charges and current density can enhance piezo-phototronic effect and light output of LED significantly.

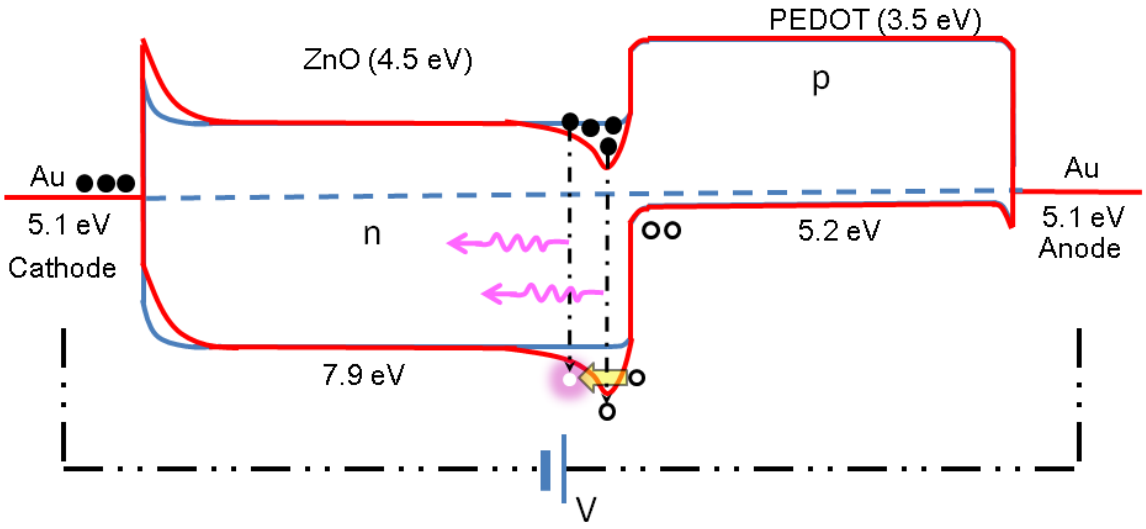

Figure 22 Proposed mechanism of the enhanced light emission under strain for a ZnO NW/p-polymer core-shell UV LED under different strain. The red line represents the band diagram considering piezo-phototronic effect, while the blue line represents the case without considering piezo-phototronic effect.

The polarity of the bias applied on the entire LED device is defined in reference to the pn junction. If the device is forward biased, the Schottky contact between the Au-ZnO is under reverse bias, which largely dictates the transported current. An increase in barrier height will result in a decrease in electron current. The increase of light output occurs with the decrease of the forward current may be suggested from the carrier trapping channel near the interface caused by the existence of piezo-charges. Electrons and holes can be temporarily trapped and accumulated in the channel and adjacent area. Since abundant electrons are available in ZnO and the extreme high barrier height for holes, the efficiency of the hybrid LED is largely dominated by the local concentration of holes. The trapped holes can increase the hole injection from PEDOT: PSS into n-ZnO, which increases the recombination efficiency of electrons and holes near the junction, leading to a large increase in emission intensity and enhancement of efficiency. On the other hand, if the c-axis of ZnO is pointing to the p-polymer, a tensile strain will introduce the same sign piezo-charges at the Schottky contact and pn junction region as that introduced by the compressive strain on an opposite c-axis orientation of the NW. In our experiments, we found that, statistically, the light output and efficiency of about 50% of the devices are enhanced under compressive strain (Figures 15 and 18), while the other half were enhanced under tensile strain (Figures 20 and 21), depending on the orientations of the c-axis of the NWs. Furthermore, we measured the light intensity of a ZnO NW/p-polymer LED under different strain in a strain applying-releasing cycle (Figure 23). The good reproducibility in a cycle shows good stability and repeatability of our device. Another interesting phenomenon can also be observed in Figure 23. The light emission intensity gets further enhanced when we apply a compressive strain with absolute value larger than 0.008%. The slope of the curve becomes smaller when the strain absolute value is larger than 0.008% which may be caused by piezoelectric nonlinearity, elastic nonlinearity and the change of electronic parameters of the core-shell structures under relative large strain, etc.[3, 59] In this paper, our major focus is on the effect

under relative small strain for simply and clearly understanding piezo-phototronic effect. The nonlinear piezo-phototronic effect shall be investigated in future work.

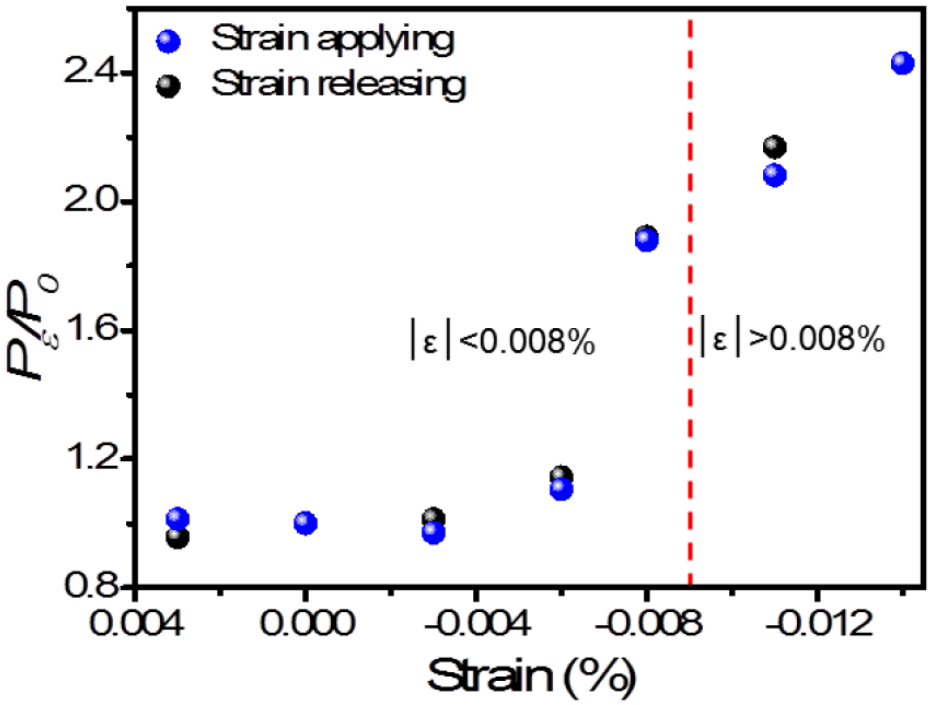

Figure 23 Repeatability measurement of the device. Relative light intensity P_s/P_0 of a ZnO NW/p-polymer LED under different strain in a strain applying/releasing cycle. All of the light intensity data were measured for more than 3 times and the average value is used in the figure for accuracy and reliability. The good reproducibility in a cycle shows the device has good stability and repeatability.

For the case that the device is reversely biased, the Schottky contact is forward biased and the pn contact is reversely biased. When the electric field is sufficiently high at the pn junction, a finite probability exists for interband quantum tunneling. Assuming a triangular potential barrier, the net current can be obtained by solving the Schrödinger equation, and the equation takes the form[36]

$$J_t = \frac{q^2\xi}{36\pi\hbar^2}\sqrt{\frac{2m^*}{E_g}}D_F \exp\left(-\frac{4\sqrt{2m^*}E_g^{3/2}}{3q\hbar\xi}\right) \quad (6)$$

where D_F is the integral of the energy along Fermi level, E_g is band gap, m^* is the effective electron mass, and the average electric field is given by

$\xi = \sqrt{\frac{q(\psi_{bi} - V)N_A N_D}{2\varepsilon_s (N_A + N_D)}}$. While the application of strain changes built-in potential ψ_{bi}, the average electric field is also changed. The channel induced by positive piezopoential will increase the built in potential. When built in potential increases, tunneling current increases and vice versa.

Although the device is demonstrated on a single NW, the same effect can be utilized to enhance the array LEDs using pattern or printing technique. Ultrasensitive and high resolution strain image may also be achieved through detection light variation from each NW LED under different strain.

Piezo-Phototronics effect in LED arrays

The quantum efficiency of LEDs, photons emitted per electron injected, is dependent upon the current balance and therefore upon the charge injection rates at the cathode and anode interfaces. We have demonstrated a UV LED based on ZnO nanowire arrays grown on GaN substrate. As shown in Figure 24, the ZnO nanowire arrays are vertically grown on a p-type GaN thin film substrate in uniform distribution. PMMA was spin coated to fill between nanowires in order to package the device and enhance the elasticity. In the tip area, PMMA are etched away and ITO is deposited to form electric connection to outer circuit. UV light comes out of almost all nanowires in the array with appropriate applied voltage, which is emitted from GaN-ZnO p-n junction area and transmitted through the ZnO NW waveguide. Notably, the position, diameter and length of the nanowire array could be well controlled experimentally with high precision and uniformity. Tiny fluctuations (for example, 1-2%) in the lengths of the nanowires would not affect the sensing result after depositing the top ITO electrode and packaging layer, because the large deformation arising from the ITO and packaging layer due to their low Young's moduli will tolerate small variations in nanowire length, as supported by FEM modelling in Figure 27.

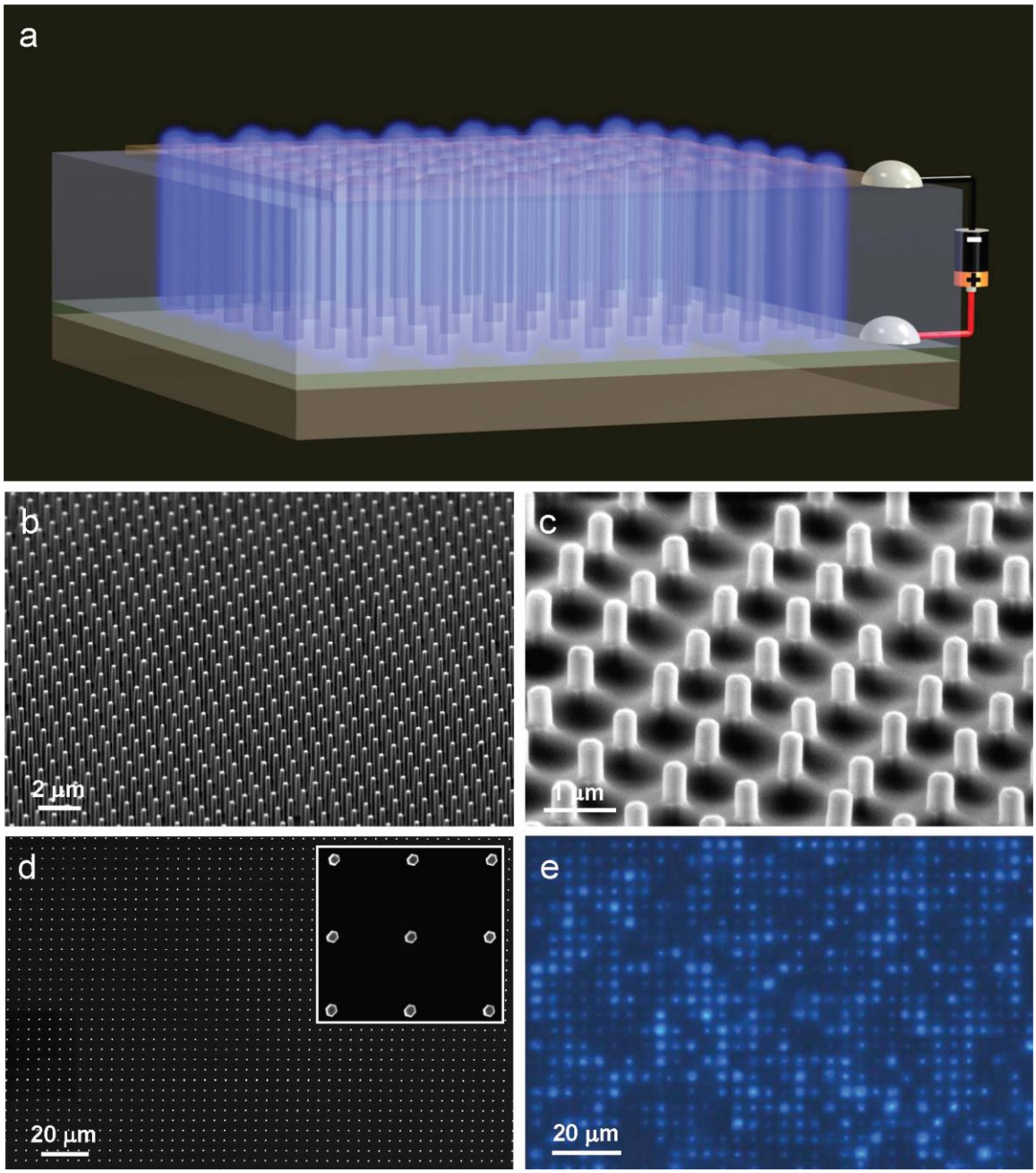

Figure 24(a) Design overview of the LED. (b) 60 °tilt SEM view of the as-grown patterned vertical ZnO nanowires with a width about 300 nm and (c) after they are coated with SiO_2 and wrapped with PMMA, and the tips are exposed. (d) Top SEM image of the ZnO nanowire arrays. The pitch and layout of the nanowire arrays are readily controlled by the EBL. (e) The optical image of a turned on LED.

The NW LED array can be uniformly lit up under a bias of 5 V. An optical image of a lit LED array is shown in Figure 25a, where each nanowire is a single light emitter and also a pixel unit. The center-to-center distance between two adjacent spots is 4 mm, corresponding to a pixel resolution of 6,350 dpi. Five typical NW LEDs marked with a

red rectangle in Figure 25a are enlarged and displayed in Figure 25b together with their intensity line profile. There is little crosstalk between adjacent pixels, and the actual resolution is 2.7 mm, as defined by the full-width at halfmaximum (FWHM) of the emission pixels. The emission spectra obtained at different bias voltages (6, 7, 8, 9, 10 V) at room temperature are shown in Figure 25c. Electroluminescence intensity increases with an increase in bias voltage, as expected from the band-bending

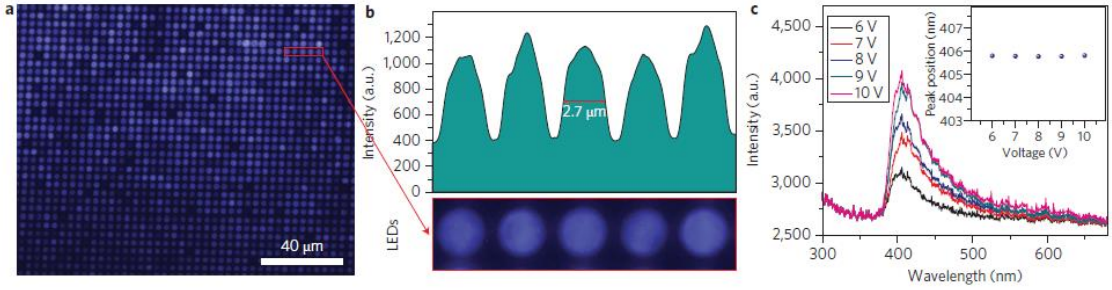

Figure 25 Characterization of NW-LED arrays. (a) Optical image of a NW-LED array when electrically emitting light. A nanowire is a single light emitter that also forms a pixel unit in the sensor array. (b) Five typical nanowire LEDs (marked with a red rectangle in a) and a corresponding line profile of the emission intensity from which the possible spatial resolution achieved by the sensor can be estimated. (c) Corresponding optical spectra of emitted light at bias voltages of 6, 7, 8, 9 and 10 V. Inset: dependence of peak position on applied voltage.

A two-dimensional mapping of strain was demonstrated using a convex character pattern of 'PIEZO' moulded on a sapphire substrate, which was directly applied onto the LED arrays as a seal (Figure 26a). Figure 30b presents an optical image of the device with an SU-8 convex mould on top. Each black dot is a pixel comprising a single ZnO NW-LED with 4 mm pitch. Light-emitting images of the device at applied strains of 0, 20.06% and 20.15% were recorded by a CCD, as shown in Figure 26c-e, respectively. The images unambiguously show that the change in LED intensity occurred at the pixels that were being compressed by the moulded pattern, while those not affected by the moulded characters showed almost no change in LED intensity. There was little crosstalk between adjacent pixels in the device. The spatial strain distribution can be extracted from the LED intensity images. By carefully aligning the two images in Figure 30c,e, an image for the enhancement factor $E(x,y) = (I_\varepsilon (x,y) - I_0(x,y))/I_0(x,y)$ was obtained, which is presented using a two dimensional contour map in Figure 26f, where (x, y) are the

coordinates of the CCD pixels in the plane. The E image provides a spatial mapping of pressure applied to the entire array, and clearly shows the word ‘PIEZO’, originating from the mould. The colour code indicates that the average enhancement factor *E* is ~200%. The signal-to-noise ratio of the *E* factor can be derived using the line profile data, as indicated for two positions in Figure 26e: one on the moulded pattern (vertical pink line) and the other off the pattern (horizontal red line). The results are presented in Figure 30g,h, respectively. The crosstalk is completely negligible, and the FWHM of the NW-LED pixels under strain is nearly the same as in Figure 25b, without strain. The *E* factor for the seven NW-LED pixels on the mould increased by a factor of 4-5 (up to 750%) when the applied strain increased from 20.06% to 20.15% (Figure 30g). In contrast, the 36 NW-LED pixels that were off the mould pattern showed no enhancement at all, instead having a random variation at the noise level when the strain was increased from 20.06% to 20.15% (Figure 30h). This unambiguously shows the gigantic effect of the piezoelectricity on LED emission. It proves the principle of using the piezo-phototronic effect for mapping pressure/strain at high spatial resolution, with high sensitivity and even high reliability.

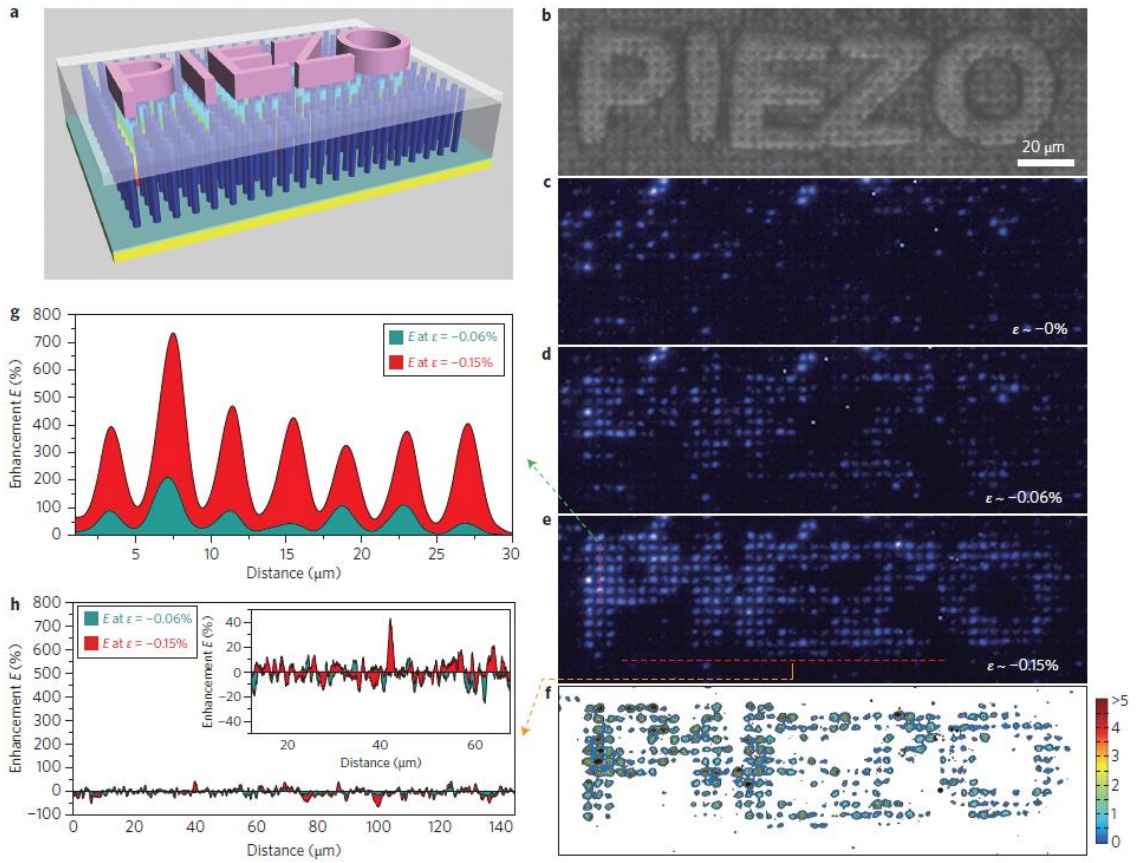

Figure 26 High-resolution parallel imaging of pressure/force distribution. (a) Illustration showing the working process of pressure distribution imaging. (b) Optical image of the device with a convex mould on top. (c)-(e), Electroluminescence images of the device at strains of 0, 20.06% and 20.15%, respectively. The images clearly show that a change in LED intensity occurred at the pixels that were compressed, while those away from the moulded pattern showed almost no change. (f) Two-dimensional contour map of the $E(x,y)$ factor derived from the LED intensity images shown in c and e. It directly presents the word 'PIEZO', as given on the mould. (g) (h) Line profile data showing the signal-to-noise ratio of the E factor for two typical positions, one on the moulded pattern (vertical pink line, (g)) and one off the pattern (horizontal red line, (h)), showing unambiguous differences.

A FEM modeling for the distribution of strain and stress in the LED array is carried out. As shown in Figure 27, 51 ZnO NWs array were built on a GaN/Sapphire substrate, the matrix is PMMA as we used in the experiments, and a layer of 300 nm ITO layer is on top of the composite structure. At last, a layer of 5 μm PDMS is on the top most of the structure. There are two reasons for introducing the PDMS layer, one is to serve as the package layer, and the other is the convex character pattern of 'PIEZO' made by polymer (SU-8), where the stress was applied to.

The dimensions of each component are as following:

Sapphire substrate: thickness = 20 μm

ZnO NWs: diameter = 1.5 μm, length = 3.8 μm

ZnO NW spacing: 4 μm

PMMA: 2.5 μm by 3.8 μm

ITO top electrode: 300 nm

PDMS layer: 5 μm

After a uniform stress of 0.8 GPa is applied on the surface of the device, the stress distribution in the devices is shown in Figure 27a. Due to the limitation of our computation power, we only built 51 NWs on the substrate in this modeling, it is clearly that the stress distribution in ZnO NWs is very uniform over the central 200 μm (see the enlarged result in Figure 27b and Figure 27c), except the four ZnO NWs at the edges, which is only less than 20 μm, as shown in Figure 27a.

For the devices used in the test, the size is about 2 cm by 2 cm, the response of NWs of the device can be treated as very uniform if we build the strain sensor on the center part of the whole device, not at the 100 μm edge area.

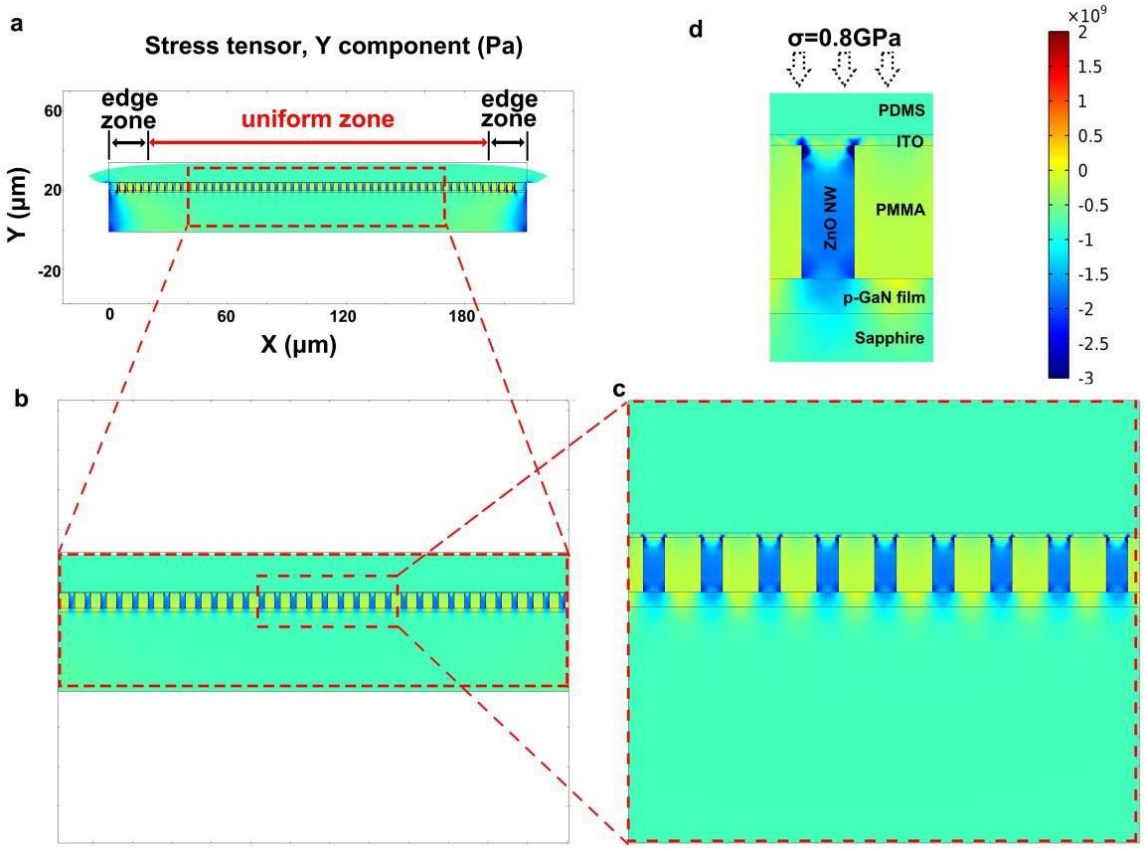

Figure 27 FEM modeling shows the distribution of stress in the device. (a) A low-magnification view of the device. (b-c) Enlarged view of the device, indicating that the stress is uniform in the middle of the device. (d) The stress in a single ZnO NW, and the scale bar of stress, which unit is Pa.

CHAPTER 4

THEORY OF PIEZO-PHOTOTRONICS EFFECT IN SCHOTTKY CONTACT

With experimental data presented, the next step is to construct a model for piezo-phototronics, which will not only provide an in-depth understanding about the experimental results, but also explore the core phenomena and build high performance devices. Besides piezo-phototronic effect, other factors such as piezoresistance effect and change of contact area or contact condition can also affect the device performance. It is important to distinguish the contribution made by the piezo-phototronics effect from these factors through theoretical analysis.

We have coupled the photoexcitation and piezoelectric terms into the basic current equations to study their influence on the final device performance. Theoretically predicted results have been quantitatively verified by photodetectors based on CdS nanowires for visible light and ZnO nanowires for UV light. The theoretical model for two-way coupling in piezotronics has been developed in previous report.[60] Here we adopt the same assumptions and follow similar methods. The Schottky contact current equation will be used as the basic starting point. The influence of photoexcitation and piezo-charges on material band structure will be discussed, and the final coupled term will be integrated into the current transport equation. To give more intuitive perspective of the piezo-phototronic effect, we have also carried out numerical calculations. One-dimensional model and other simplification are adopted for easy understanding. The core equations and conclusions are shown as follows.

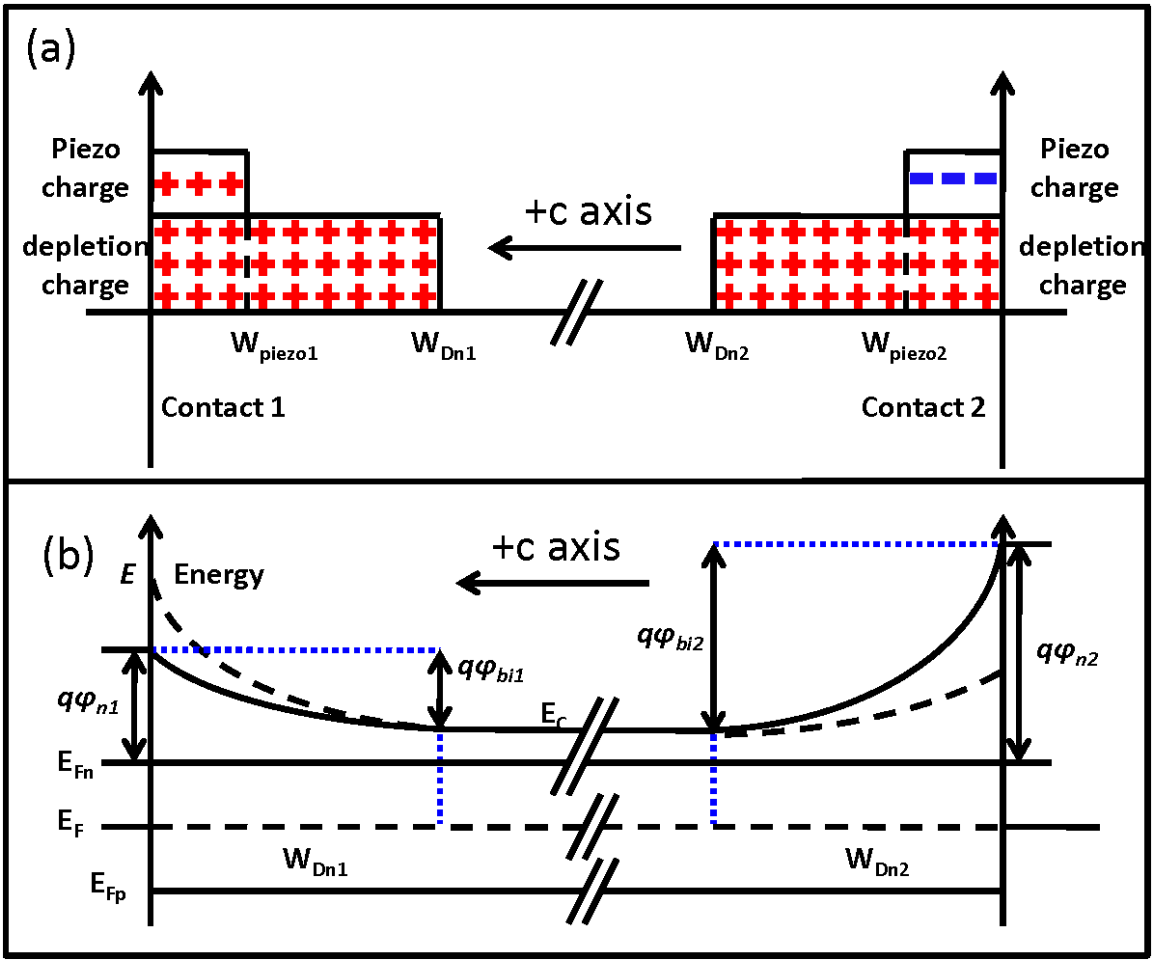

Figure 28 Illustration of ideal metal–semiconductor-metal structures with the presence of piezo-charges and photon generated charges. (a) Space charge distribution and corresponding (b) energy band diagram in the presence of piezo charges and photo generated charges. Dashed lines stand for original barriers without strain nor photoexcitation. The solid line is the finally tuned band structure by the piezo-charges, with one end being lifted up and one side being lowed.

Analytical Model

Basics of Piezoelectricity

Piezoelectricity is defined as: electric polarization produced by mechanical strain in crystals belonging to certain classes, the polarization being proportional to the strain and changing sign with it.[61] At the atomic level, piezoelectricity comes from the lack of centrosymmetry/inversion symmetry in the crystal. Twenty one out of all thirty two crystal classes lack inversion symmetry, and twenty of them exhibit piezoelectric effect. The two most important classes include Perovskite structure, which occurs in ceramics

such as Lead Zirconate Titanate (PZT) and Barium Titanate ($BaTiO_3$); and Wurtzite structure, which occurs in semiconducting materials such as ZnO, Gallium Nitride (GaN), Indium Nitride (InN), and Zinc Sulfide (ZnS).

In a Wurtzite structure, each of the two individual atom types forms a sublattice which is hexagonal close pack (HCP) type, and they form tetrahedral coordination with each other.[62] Distinct from Perovskite structure, Wurtzite structure crystals do not need distortion or external poling to break the centrosymmetry. In single crystals, there are strong and uniform dipoles along the *c* axis, and the dipole direction is determined by the stacking order position of the anions and cations, and more specifically, $+c$ for from cation to anion and $-c$ for from anion to cation. The orientation and polarity determines the direction of the piezoelectricity in the crystal. In ZnO, the interaction of the polar charges at the surface results in the growth of a wide range of unique nanostructures, such as nanobelts, nanosprings, nanorings and nanohelices.

In theoretical concern, piezoelectricity refers to the linear coupling of electricity and mechanics.[63] Considering electrical behavior, we have Maxwell's equation: $D = \varepsilon_r E$, where D is electric displacement, ε_r is permittivity, and E is electric field. Considering mechanical behavior, we have Hooke's law: $\boldsymbol{\varepsilon} = sT_s$, where $\boldsymbol{\varepsilon}$ is strain, s is compliance and T_s is stress. To describe piezoelectricity, the coupled equations are given as

$$D = \varepsilon_R E + [e]S \tag{7}$$

where $[e]$ is the direct piezoelectric effect matrix, and its specific form is related to the point group to which the crystal belongs. The most frequently used parameter is the piezoelectric coefficient e_{33}, with expression, so the unit of e_{33} is either C/m^2. When normal stress is applied along the polarization axis and on the surface charge is collected, e_{33} can be simplified as the electric polarization when subject to stress. A similar parameter e_{31} is applied when stress is applied at right angle with the polarization axis.

As in previous theoretical frame work for piezotronics, [60] by solving the Poisson equation according to Figure 28, the modification to the Schottky barrier height by piezo-charges is

$$\Delta\phi_{piezo} = -\frac{1}{2\varepsilon}\rho_{piezo}W_{piezo}^{2} \quad (8)$$

where ρ_{piezo} is the density of the strain-induced piezo-charges at nanowire side of the metal-semiconductor junction, and W_{piezo} is the width of the piezo-charge distribution adjacent to the interface.

As piezoelectricity originated from inner crystal polarization of ions, the piezo-charges can be seen as fixed charges at the two ends of the nanowire with opposite signs, which is shown in Figure 28a. For a Wurtzite structured nanowire with strain along the c-axis, which is assumed to be the growth direction of the nanowire, the piezo polarization is

$$P = e_{33}\varepsilon_{33} = \rho_{piezo1}W_{piezo1} = -\rho_{piezo2}W_{piezo2} \quad (9)$$

where ε_{33} stands for the strain along the c-axis, ρ_{piezo1} is the density of the strain-induced piezo-charges at contact 1, and ρ_{piezo2} is the density of the strain-induced piezo-charges at contact 2.

Basics for Photoexcitation

The basic equation for photodetetion is referenced in the experimental sections. The resonsivity of a photodetector is the most important figure of merit, and is defined as the ratio of photocurrent over the incident optical power.

Photons with energy higher than the band gap (E_g) of the photodetector material will excite electron-hole pairs. Under a steady light illumination, the excess free carrier concentration is given by the continuity equation [64]

$$\Delta n = \Delta p = \tau_n G_L(I) \quad (10)$$

where Δn is the excess electron concentration and Δp the excess hole concentration under light illumination, τ_n is the carrier lifetime, and $G_L(I)$ is the rate of photon generation, which is a function of light intensity.

Without photoexcitation, the Fermi level of the semiconductor lines up with the Fermi level of the metal. When light is illuminated onto the nanowire, the existence of excess carriers will result in a split of the original Fermi level into two quasi-Fermi levels for electrons and holes accordingly, as shown in Figure 28b. In bulk materials, the absorption of light decays with distance into the semiconductor, yet in our NW photodetector, as the NW diameter is so small, it is reasonable to assume that as long as light illumination is uniform, the quasi Fermi level should also be uniform along the entire nanowire. The quasi Fermi level E_{Fn} for electrons and E_{Fp} for holes can be described by [65]

$$E_{F_n} = E_F + kT \ln\left(\frac{n_0 + \Delta n}{n_0}\right) \tag{11}$$

$$E_{Fp} = E_F - kT \ln\left(\frac{p_0 + \Delta p}{p_0}\right) \tag{12}$$

Current Density for Forward Biased and Reversely Biased Schottky Contact

For an n-type Schottky contacted device between a metal and a semiconductor, under forward bias voltage, the thermionic emission (TE) theory should be adopted for the charge carrier transport, and the current density under forward bias J_F is[65]

$$J_F = A^* T^2 e^{-\frac{q}{kT}\phi_n}\left(e^{\frac{q}{kT}V} - 1\right) \tag{13}$$

where A^* is the Richardson constant, T is temperature, ϕ_n is the effective Schottky barrier height, and V is the applied voltage across the contact.

For a reversely biased n-type Schottky contact, the thermionic field emission (TFE) theory better describes the behavior of heavily doped semiconductor materials

with considering the tunneling effect.[65-66] According to the TFE theory, the current density under reverse bias takes the form of

$$J_R = J_{sv} e^{-\frac{q}{E_0}\phi_n} e^{V_R(\frac{q}{kT}-\frac{q}{E_0})} \quad (14)$$

where J_{sv} is the slowly varying term regarding applied voltage and Schottky barrier change, V_R is the reverse voltage, k the Boltzmann constant, and E_0 is a tunneling parameter of the same order of but larger than kT.[67] Usually E_0 is larger than kT, and is constant regarding barrier height and applied voltage, so it is reasonable to assume that $E_0 = akT$, with $a > 1$, so equation (9) now becomes

$$J_R = J_{sv} e^{-\frac{q}{akT}\phi_n} e^{V_R\frac{q}{kT}(1-\frac{1}{a})} \quad (15)$$

Piezo-Phototronics Effect for a Single Schottky Contact

For a Schottky contact, photo excitation and introduction of local piezo-charges can change the barrier height, which can be quantitatively expressed as

$$\Delta\phi_n = -\frac{1}{2\varepsilon}\rho_{piezo} W_{piezo}^2 - \frac{kT}{q}\ln(\frac{n_0+\Delta n}{n_0}) \quad (16)$$

Thus, the modified barrier height is

$$\phi_n = \phi_{n0} + \Delta\phi_n \quad (17)$$

where φ_{n0} is the original Schottky barrier height without strain nor light illumination.

The electron current density transported through a forwardly biased Schottky contact is then

$$J_n = J_{n0}(\frac{n_0+\Delta n}{n_0})\exp(\frac{q}{kT}\frac{1}{2\varepsilon}\rho_{piezo} W_{piezo}^2) \quad (18)$$

where J_{n0} is the current density without applying light illumination nor external strain, and $J_{n0} = A^* T^2 e^{-\frac{q}{kT}\phi_{n0}}(e^{\frac{q}{kT}V} - 1)$

As the sign of ρ_{piezo} depends on the direction of c-axis and type of applied strain, the influence of piezo-charges can either enhance photo excitation or reduce it.

Piezo-Phototronics Effect for a Double-Schottky-Contact Structure

In a device with double Schottky contacts, with certain bias voltage, one junction will be reversely biased and the other junction will be forwardly biased. The current across the double Schottky junction device should take the form

$$I = S_R J_R = V_{NW} / R_{NW} = S_F J_F \tag{19}$$

where S_R and S_F are cross section area for reverse junction and forward junction accordingly, R_{NW} is the resistance of the nanowire, and V_{NW} is the voltage across the nanowire. Thus we have

$$V_R + V_{NW} + V_F = V \tag{20}$$

where V_R and V_F are the voltage across the reverse and forward junction, V is the total applied voltage.

In equation (19), the R_{NW} term mainly influences the current behavior at applied voltage above 5 V or higher,[67] and at working voltage range for photodetection, the dominating term should be mainly controlled by the reversely biased contact. To clearly see the effect of piezo-charges and photo excitation, we make reasonable simplifications that $V_R = cV$, where c is assumed constant and $c < 1$. Thus, equation (10) now becomes

$$J = J_{sv} \exp\left(-\frac{q}{akT}\phi_{n0}\right) \exp\left[V \frac{q}{kT} c\left(1 - \frac{1}{a}\right)\right] \left(\frac{n_0 + \Delta n}{n_0}\right)^{\frac{1}{a}} \exp\left(\frac{q}{akT} \frac{1}{2\varepsilon} \rho_{piezo} W_{piezo}^{\ 2}\right) \tag{21}$$

Thus, the device current under different bias voltage takes the form

$$I = S_1 J_{C1} \left(\frac{n_0 + \Delta n}{n_0}\right)^{\frac{1}{a}} \exp\left(\frac{q}{akT} \frac{1}{2\varepsilon} \rho_{piezo} W_{piezo}^{\ 2}\right)$$ when contact 1 is under reverse bias (V>0)

(22)

$I = -S_2 J_{C2} (\frac{n_0 + \Delta n}{n_0})^{\frac{1}{a}} \exp(\frac{q}{akT} \frac{1}{2\varepsilon} \rho_{piezo2} W_{piezo2}^{\ 2})$ when contact 2 is under reverse bias (V<0) (23)

where $J_{C1} = J_{sv1} \exp(-\frac{q}{a_1 kT} \phi_{n10}) \exp[V \frac{q}{kT} c_1 (1 - \frac{1}{a_1})]$, and

$J_{C2} = J_{sv2} \exp(-\frac{q}{a_2 kT} \phi_{n20}) \exp[V \frac{q}{kT} c_2 (1 - \frac{1}{a_2})]$, are the currents under reverse bias for contact 1 and 2 accordingly, and S_1 and S_2 are the areas for junction 1 and 2, respectively. As ρ_{piezo1} and ρ_{piezo2} have opposite signs, equation (20) shows asymmetric change in photocurrent under opposite bias by the same amount of applied strain.

Numerical Simulation of MSM Photodetector

We now apply our analytical result to numerical calculation for a Ag-CdS-Ag structure. As the materials for piezo-phototronics are mainly Wurtzite structured materials who share the same crystal symmetry, their piezoelectric coefficient matrix takes the same form.

The parameters for CdS, the dielectric constant $\varepsilon_r = 9.3$,[68] piezoelectric coefficient $e_{33} = 0.385$ C/m^3. For photoexcitation, we suppose the external quantum efficiency $\eta_{ext} = 1$, the internal gain $\Gamma_G = 1.5 \times 10^5$, [4] carrier lifetime $\tau_n = 3$ ns.[69] For typical UV photodetection experiments the light wavelength $\lambda = 385$ nm. The diameter of the ZnO nanowire is assumed to be 100 nm. At dark condition, assume the electron concentration in ZnO nanowire is 1×10^{15} cm^{-3}.

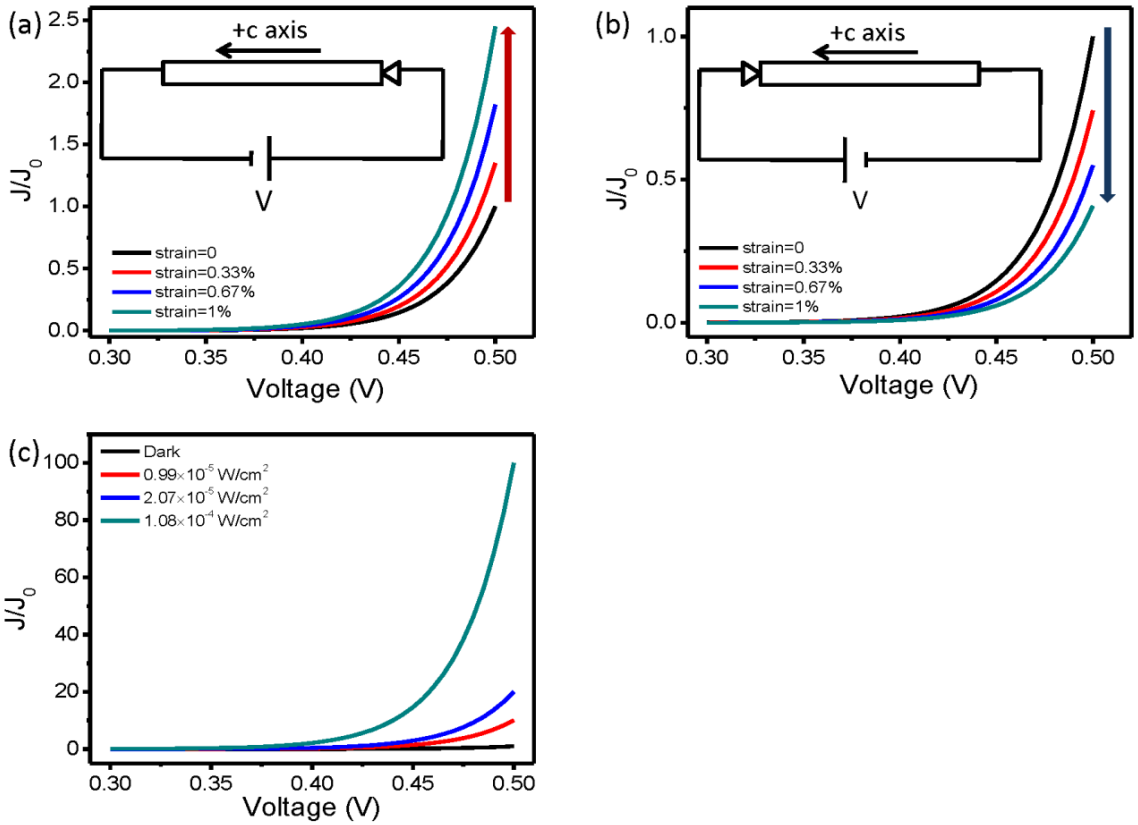

Figure 29 Results for numerical simulation for a metal-CdS-metal photodetector. J_0 is set as the current of the device at zero strain and at applied voltage of 0.5 V. Insets are the configuration of device and direction of forward bias. (a, b) with a Schottky contact on one end and Ohmic contact on the other end. Relative current density vs. voltage under different strains and the same illumination power, for two devices with different orientation of c-axis regarding the position of the Schottky contact. (c) Current-voltage diagram under different illumination power.

For an Ag-CdS-Ag structure with one Ohmic contact and one Schottky contact, when forward bias is applied on the Schottky contact, using Equation (21), we are able to calculate the photocurrent under the same intensity of light illumination with applied strain varying from 0 to 1%. Depending on the direction of c-axis, the photocurrent can either increase or decrease with applied strain. Figure 29a and 29b shows the performance of two single-Schottky-contact devices, the configuration of which are shown in the inset of Figure 29a and 29b accordingly. We are also able to calculate the photocurrent under strain free condition with different illumination power, as shown in Figure 29c.

For an Ag-CdS-Ag structure with two Schottky contacts at both ends, we set a =1.3 and c = 0.8 in equation (21), which are reasonable values according to previous reports.[67] The result of simulation according is shown in Figure 30a. The asymmetric characteristic of the piezo-phototronic effect is demonstrated very clearly: the change of current under the same amount of applied strain is opposite when the bias voltage is applied at opposite direction.

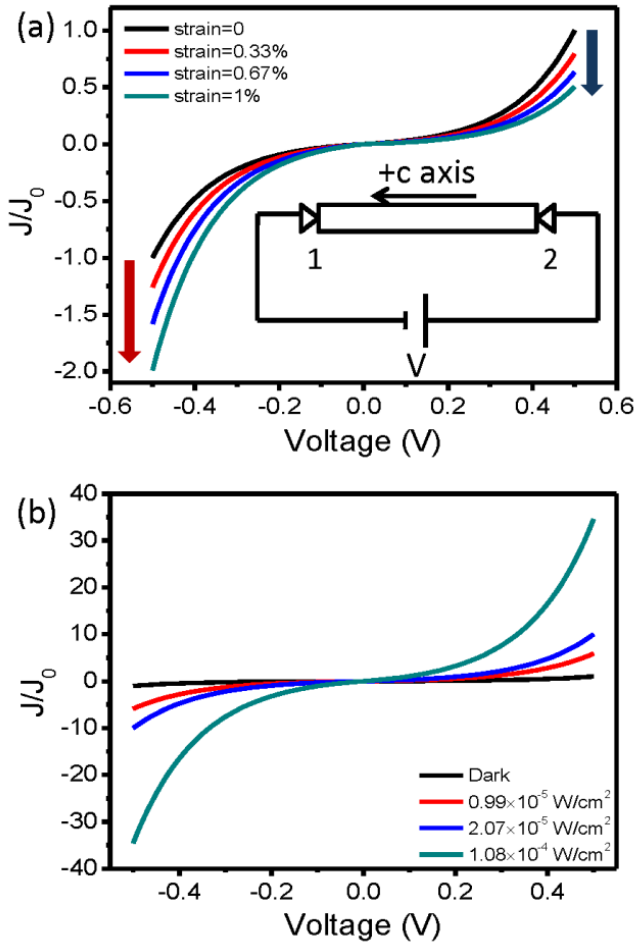

Figure 30 Numerical simulation for a metal-CdS-metal photodetector with Schottky contact on both ends based on our analytical solution. (a) Relative current density vs. voltage under different strains and the same illumination power. J_0 is set as the current of the device at zero strain and at reverse applied voltage of 0.5 V. Inset is the configuration of device and direction of forward bias. (b) current-voltage diagram under different illumination power. J_0 is set for the dark current at forward applied voltage of 0.5 V.

For ZnO, the dielectric constant ε_s = 8.9, piezoelectric coefficient e_{33} = 1.22 C/m^3, carrier lifetime τ_n = 3.0 ns.[69] which means that the simulation results for ZnO will only

have slight difference in magnitude with CdS, and will have the same trends of change with strain and light intensity. Numerical simulation for ZnO photodetection is also carried out and shown in Figure 31.

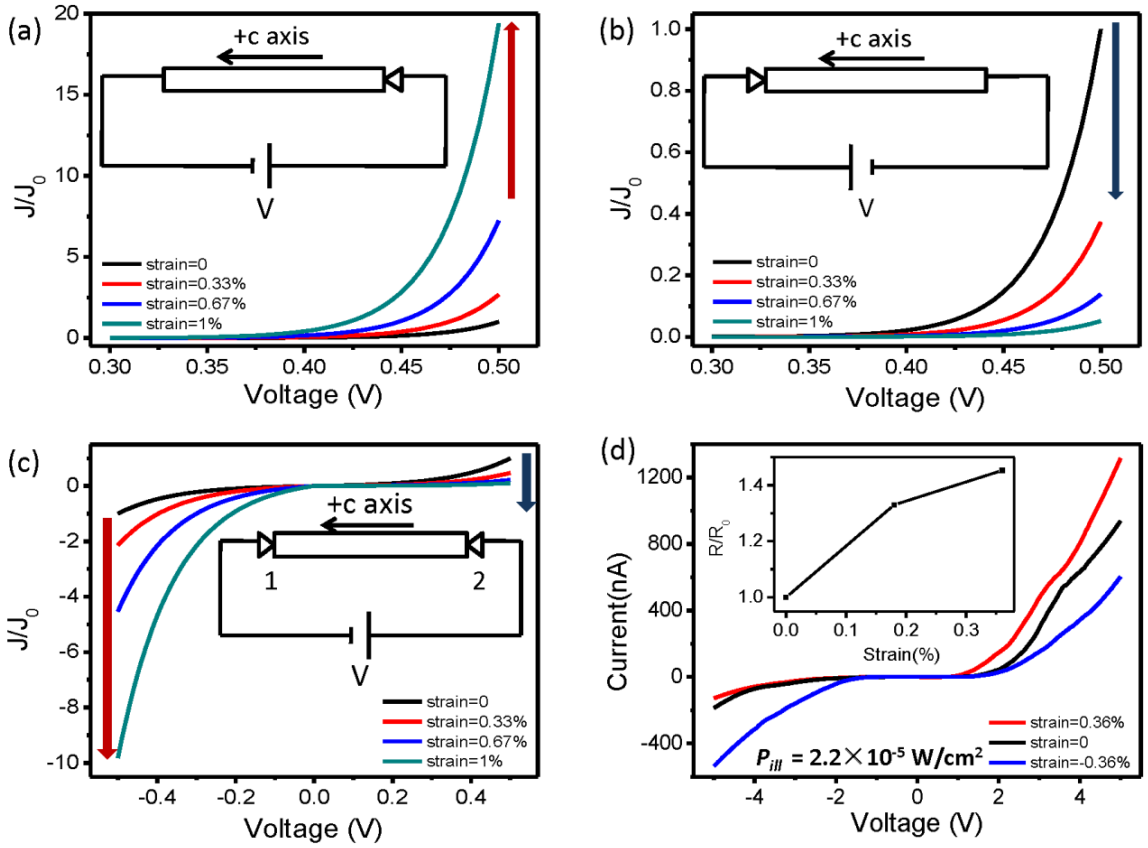

Figure 31 Numerical calculation regarding photodetection of Ag-ZnO-Ag structure. (a) (b) are relative current density vs. voltage under different strains and the same illumination power, for two devices with different orientation of c-axis regarding the position of the Schottky contact. J_0 is set as the current of the device at zero strain and at applied voltage of 0.5 V. Insets are the configuration of device and direction of forward bias. (c) Relative current density vs. voltage under different strains and the same illumination power. J_0 is set as the current of the device at zero strain and at reverse applied voltage of 0.5 V. Inset is the configuration of device and direction of forward bias. (d) Characteristic of a piezo-phototronic photodetection based on ZnO nanowires for UV light. The asymmetric change of current under changing strain is clearly demonstrated. Inset is the change of responsivity for forward bias under positive strain.

Consideration of other factors

Effect of piezoresistance

When a crystal lattice is deformed under strain, the band gap width shall have a minor change, and can finally result in conductance change of the semiconductor. This is called piezoresistance effect.[70-71] The piezoresistance effect is present in semiconductors

either with or without piezoelectricity. In piezotronics and piezo-phototronics, piezoresistance is always accompanied with the piezoelectric effect.

In piezoresistance effect, the change of resistance is given by

$$\frac{\delta\rho}{\rho} = \pi \frac{\delta l}{l} \tag{24}$$

where ρ is the resistance of the semiconductor, l is the original length of the nanowire, $\delta\rho$ is the resistance change due to piezoresistance effect, δl is the change in nanowire length, and π is the piezoresistance coefficient. From equation (24), we can see that the piezoresistance is a resistance effect that is a uniform and symmetric effect regardless the biasing of the applied voltage

Effect of series resistance

There are a lot of factors that result in deviation of *I-V* characteristic from ideal current-voltage equation, and one of the most important factors should be the effect of series resistance. Series resistance is the equivalent resistance of various factors in the electric circuit, including outer circuit resistance, capacitors and inductors. Methods to solve the influence of series resistance have been extensively developed.[72-73] According to these solutions, when applied voltage is small, the device behavior is dominated by current equations for contact junction; when applied voltage is large, the device behavior is mostly linear.

Other factors

Other factors also include the surface trapped charges on the contact areas, and change in contact areas due to externally applied strain. These factors either have similar behavior with piezoresistance effect or should be too small to affect the results.

Judging Criteria for Piezo-phototronic Photodetection

In our model and experiments, we successfully demonstrate the difference between the piezo-phototronics effect and other non-piezoelectric effects in highly sensitive photodetection. Here we propose three criteria for characterizing piezo-phototronic photodetection.

1. Piezo-phototronic photodetection requires the presence of charge barrier, including a Schottky junction, p-n junction or some special heterostructure. Recent studies have also shown that special structures such as core-shell nanowires made of materials that have a lattice mismatch, a staitc internal potential field can also be induced due to piezoelectric effect.[74] The piezo charges originate from the dipole nature of piezoelectricity, and they accumulate at the ends of the piezoelectric semiconductor nanowire as fixed charges. With the existence of a charge barrier, the small amount of piezo charges can effectively tune the current transport properties of the photodetector.
2. Photoexcitation influences the current-voltage characteristic through generating excess free charges. Provided that the entire device is under uniform illumination, photon generation of electrons and holes effectively tunes quasi Fermi level, and this change is applied along the entire wire, resulting in a decrease of the barrier height.
3. Piezoelectric effect influences photodetection by strain induced polar charges at the ends of the nanowires. The effect of piezo-charges in a double Schottky contact photodetector shall result in asymmetric change in barrier heights at the two sides. Other factors induced by external strain such as piezoresistance or contact area change will induce symmetric change in both ends of the nanowire. In this way, we can easily tell whether the change is caused by genuine piezo-phototronics effect.

These three criteria give a better understanding of our piezo-phototronics experiments, and work as guidance for our future work in related areas.

CHAPTER 5

THEORY AND 2D SIMULATION FOR PN JUNCTION

Previous explanations of this effect were limited to one-dimensional (1D) analysis, which did not take device geometry factors into consideration, especially in light emitting devices. Here, we developed a methodology for 2D simulation of the piezo-phototronic effect in a p-n junction based LED. With this methodology, we utilize finite element method (FEM) to overcome the difficulty of analytical modeling and provide more intuitive results, including band structure and device current characteristics under different device geometries, which can be compared with experimental data and provide an optimization approach.

Model Development

COMSOL multiphysics software was utilized for most of the calculations in this study. A major difficulty with semiconductor device simulation via the FEM is the large gradient of charge concentration, electric field and local band energy in the depletion region, which may result in singularity or failure to converge. Thus, in our simulation, higher order solvers and mesh refinement were utilized. For carrier current calculations, both the time-dependent solver and stationary solver were used in conjunction with the introduction of electrical circuit equations in the COMSOL.

The two-dimensional layout of our theoretical model was built according to common experimental designs,[75-76] which includes an n-type piezoelectric nanowire (NW) structure and a thin film p-type substrate, as shown in Figure 33a. The NW is 1 μm $\times 10$ μm and the substrate is 10 μm $\times 10$ μm in size. The diameter of the NW is close to the ZnO NW used in LED experiments. One end of the NW is set as the cathode with an ohmic contact, and the other end is attached to the surface of a p-type thin film

component that also serves as a substrate for supporting the NW. The c-axis of the NW (its growth direction) is set pointing from the substrate to the cathode. Uniaxial strain is applied along the axis of the NW, and the strain-induced piezoelectric polarization charges exist at the p-n junction. In this simulation work, the piezo-phototronic effect under both tensile strain and compressive strain are studied. For a p-type NW/n-type thin film structure, the simulated results can be amended to apply without any subtle change.

As for material choice, ZnO was utilized as the material for both the n-type NW and the p-type substrate of homojunctions, and p-GaN was utilized to investigate the effect of p-n heterojunctions.[77] The conclusions from such materials can be easily extrapolated to p-type NWs and other n-type materials. For a simplified model of the phenomenon, strain is set as applied along the c-axis growth direction of the NW, the p-type thin film is assumed non-piezoelectric, and factors including spontaneous polarization, deformation potential and reverse piezoelectric effect are neglected here.

The basic material parameters of ZnO/GaN are taken from the database provided with the COMSOL software and from reported data[78-79] as:

Table 2 Material Properties Used in Simulation

Property	ZnO	GaN
Relative Permittivity (ε_r)	9.1	10
Band Gap (E_g)/eV	3.38	3.40
Electron Affinity (χ)/eV	4.5	4.1
Valence band Density of State (N_V)/cm^{-3}	3.5×10^{18}	4.1×10^{19}
Conduction band Density of State (N_C) /cm^{-3}	1×10^{20}	1.2×10^{18}
Electron Mobility(μ_n)/m^{2}V^{-1}s^{-1}	0.2	0.2

Table 2 continue

Hole Mobility(μ_p)/$m^2V^{-1}s^{-1}$	10^{-3}	10^{-3}

The doping profile of ZnO is set as 1×10^{15} cm^{-3} for both n-type and p-type in our simulation, which is based on the low defect concentration of high temperature chemical vapor deposition (CVD) synthesized ZnO NWs.

Results for Numerical Simulation

Strain-induced Change of Band Structure

A critical concept in the piezo-phototronics effect is the formation of a piezo-charge induced channel in the p-n junction depletion region, which can serve as an effective means for tuning the carrier separation or recombination. For the LED structure, a positive charge channel is proposed for trapping the holes in the valence band at the metallurgical junction and increasing the recombination probability,[1] so that the light emission efficiency is enhanced. Therefore, our objective here is to validate the existence of such a charge channel from rigorous theoretical calculation.

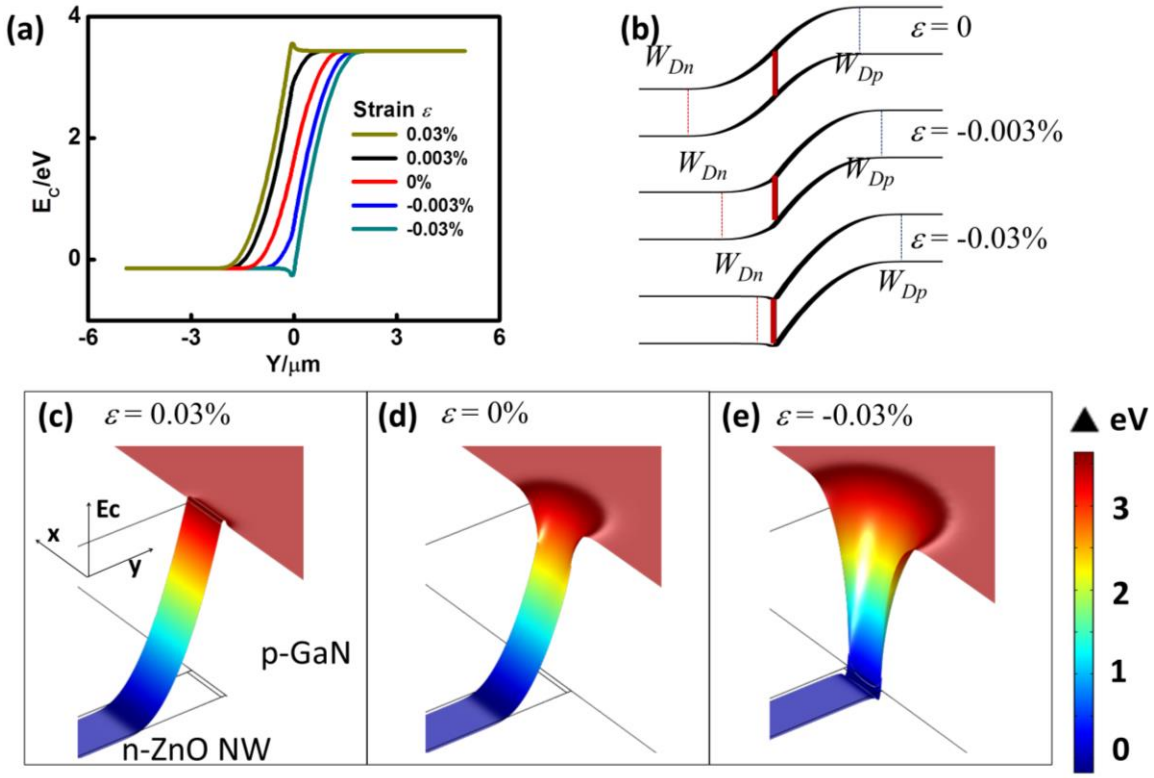

Figure 32 (a) Conduction band deformation of n-ZnO/p-ZnO structure under different strain on n-type side, 1D simulation, (b) illustration of the formation of charge channel, (c, d, e) Conduction band in height expression from 2D simulation in n-ZnO/p-ZnO structure under (c) 0.03% strain (d) no strain and (e) -0.03% strain at the n-type side

To address this problem, as the first step, we need to get the piezo-charge density at the p-n junction interface. The piezo-charge density can be obtained from the piezoelectric polarization *P*, which can be retrieved from the constituitive equation, as addressed in the previous chapter as equation (15). In this simulation, *P* is first calculated for the piezoelectric material by assuming that it is an insulator, then the obtained polarization charges at the interface area are used as an input for the next step of the calculation.

Then, using a 1D finite element model, we have calculated the band edge deformation under different strain conditions, and the resulting conduction band is shown in Figure 36b for a homojunction. The spatial variation of the valence band edge is identical to the spatial variation of the conduction band (offset by the band gap energy) and thus it is not necessary to plot it for the homojunction. The deformation of the

valence band edge and the conduction band edge are calculated by solving the Poisson equation. [80] In COMSOL, the electron concentration *n* and hole concentration *p* are solved self-consistently in the depletion region.

In regions far from the depletion zone, the conduction band energy and valence band energy are flat and fixed at values calculated from the bulk material properties and the background doping profile. Therefore, built-in potential ψ_{bi} is fixed at the difference between Fermi levels of the original doping. When piezo-charges are present, a 1D approximation will result in

$$N_A W_{Dp} = N_D W_{Dn} + \rho_{piezo} W_{piezo} \quad (25)$$

N_A is the p-type doping density in the p-type region, N_D is the n-type doping density in the n-type region, W_{Dp} is the depletion width in the p-type region, and W_{Dn} is the depletion width in the n-type region.

Thus, the depletion region will shrink on the n-type side and expand on the p-type side when $\rho_{piezo} > 0$ (positive piezo-charges), as shown in Figure 32a at strain ε = -0.003%; when $\rho_{piezo} < 0$ (negative piezo-charges), the depletion region will expand on the n-type side and shrink on the p-type side, as shown in Figure 32a at ε = +0.003%. In previous analytical models, it was assumed that the depletion region will have negligible change in width under strain, and the influence of piezo-charges is mainly changing the local built-in potential. As both the density and total amount of piezo-charges are dependent only on piezoelectric coefficient of the material and the existing strain, and independent of the doping profile of the material, this assumption is valid when the doping profile is low so that the total amount of depletion charges of the unstrained structure is far greater than the total amount of piezo-charges. Referring to experiments, this assumption is applicable to hydro-thermally grown NWs with abundant defects as well as photodetectors and solar cells with photo excited free charge carriers,[81-82] as depletion charge amount in these materials are far larger than piezo-charges under

experimental straining conditions. However, in our simulation, the doping profile is low so that the total amount intrinsic depletion charge is much smaller than the amount of piezo-charges at the junction interface. Thus the presence of piezo-charges at the interface results in significant change to the width and shape of the depletion zone due to the electrostatic interaction of the piezo-charges with the carriers in the region.

When the total amount of piezo-charges further increases and $\rho_{piezo}W_{piezo} >> N_D W_{Dn}$, as shown in Figure 32b, the entire depletion region shifts toward the p-type region ; in such a case W_{Dn} shrinks to the width of the piezo-charges distribution, and the localized piezo-charges will affect the charge redistribution, and we have $\Psi_n + \Psi_p > \psi_{bi}$, where Ψ_n is the potential built in the n-type side and Ψ_p is the potential built in the p-type side. Thus, in the depletion region, the local deformation will result in the presence of a charge channel, *i.e.* electron trap at ε = -0.03% and hole trap at ε = +0.03% shown in Figure 36a.

Next, the 2D geometry in Figure 33a is simulated, in which case the Poisson equation is

$$\begin{cases} \varepsilon_r\left(\frac{\partial E_x}{\partial x} + \frac{\partial E_y}{\partial y}\right) = -qN_A \\ \frac{\partial^2 \Psi_i}{\partial x^2} + \frac{\partial^2 \Psi_i}{\partial y^2} = \frac{qN_A}{\varepsilon_r} \end{cases} \quad \text{on p-side depletion region} \tag{26}$$

$$\begin{cases} \varepsilon_r\left(\frac{\partial E_x}{\partial x} + \frac{\partial E_y}{\partial y}\right) = qN_D \\ \frac{\partial^2 \Psi_i}{\partial x^2} + \frac{\partial^2 \Psi_i}{\partial y^2} = -\frac{qN_D}{\varepsilon_r} \end{cases} \quad \text{on n-side depletion region} \tag{27}$$

$$\begin{cases} \varepsilon_r\left(\frac{\partial E_x}{\partial x} + \frac{\partial E_y}{\partial y}\right) = q\rho_{piezo} \\ \frac{\partial^2 \Psi_i}{\partial x^2} + \frac{\partial^2 \Psi_i}{\partial y^2} = -\frac{q\rho_{piezo}}{\varepsilon_r} \end{cases} \quad \text{in piezo-charge region} \tag{28}$$

2D height plots are shown in Figure 32c, d, e to demonstrate the change in conduction band structure in the 2D case. In the simulated geometry, in regions close to the middle line on y-axis, $\frac{\partial E_y}{\partial y}$ and $\frac{\partial^2 \Psi_{bi}}{\partial y^2}$ will be close to zero, and the result is similar to 1D result. In other parts of the depletion zone, the influence of the piezo-charges will decrease compared to the 1D simulation, which means that the charge channels will require greater strain to become significant.

Simulation of Current-Voltage Characteristics

The current-voltage characteristics are among the most important data for piezotronics and piezo-phototronics. The simulation results for n-ZnO/p-ZnO structure with the geometry layout shown in Figure 33a are plotted in Figure 33.

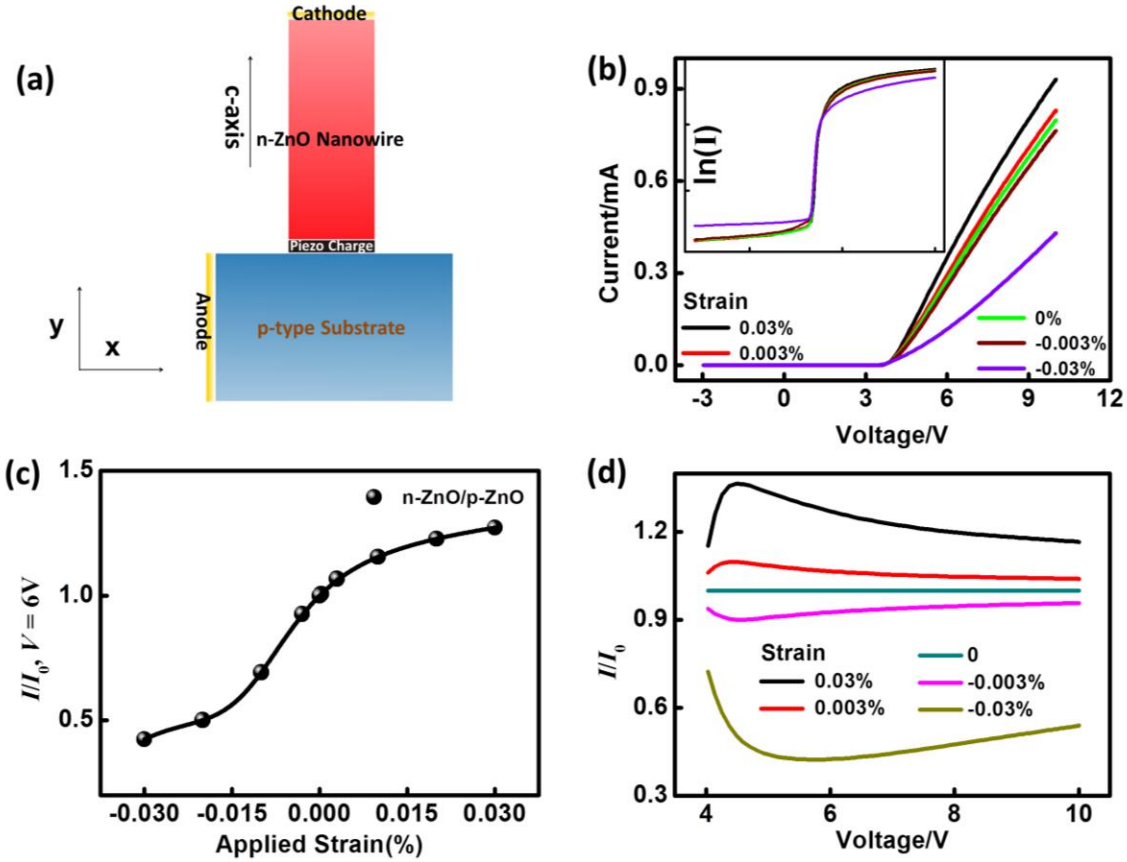

Figure 33 (a) Geometry of 2D simulation, (b) Current-voltage curve of n-ZnO/p-ZnO, (c) Change of current when bias is fixed at 6 V under different strain, I_{strain}/I_0 vs ε, (d) Relative change of current under strain vs. applied voltage, I_{strain}/I_0 vs V

For current calculation and integration through the whole geometric structure, the time-dependent continuity equations for current density are used[80]

$$\frac{\partial n}{\partial t} = -\frac{1}{q}\nabla \cdot \vec{J}_n - U_n + G_n \tag{29}$$

$$\frac{\partial p}{\partial t} = \frac{1}{q}\nabla \cdot \vec{J}_p - U_p + G_p \tag{30}$$

In the drift-diffusion approximation we have:

$$\vec{J}_n = \mu_n n \nabla E_C + qD_n \nabla n \big|_{W_{Dn}} \tag{31}$$

$$\vec{J}_p = \mu_p p \nabla E_V - qD_p \nabla p \big|_{W_{Dp}} \tag{32}$$

where $\boldsymbol{J_n}$ and $\boldsymbol{J_p}$ are electron and hole current densities; U_n and U_p are electron and hole recombination rates; G_n and G_p are electron and hole generation rates, E_C and E_V are conduction band energy and valence band energy; and D_n and D_p are electron and hole diffusion coefficients, respectively. The series resistance is set as zero for simplicity.

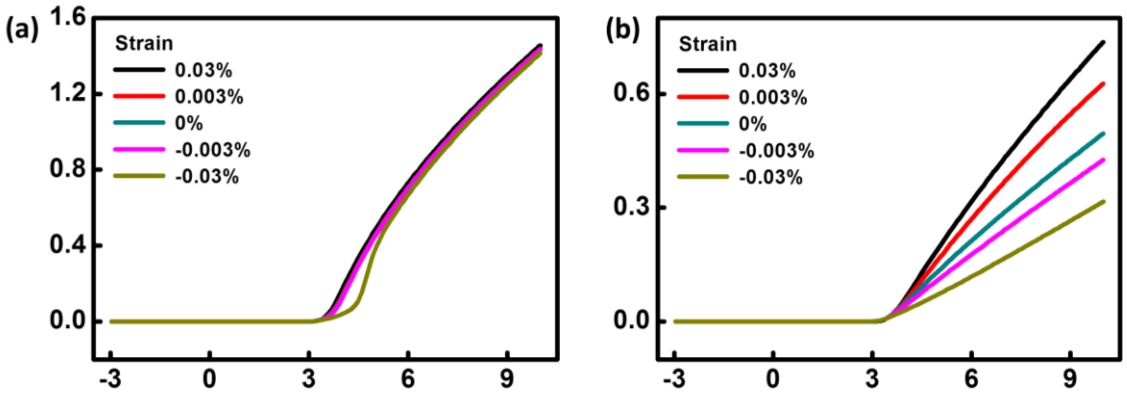

Figure 34 Current-voltage characteristics under different strain for (a) μ_p = 10 $m^2V^{-1}s^{-1}$ and μ_n = 0.2 $m^2V^{-1}s^{-1}$ in p-type GaN region, which is unrealistically high for hole mobility, and (b) $\mu_p = 5\times10^{-4}$ $m^2V^{-1}s^{-1}$ and μ_n = 0.2 $m^2V^{-1}s^{-1}$ in p-type GaN region. The influence of strain decreases to a great extent, indicating depletion resistance is the major reason for the current change here.

The depletion region is the main barrier for device current; however, the undepleted p-doped substrate region provides a large effective series resistance, due to the low mobility of the majority holes. When compressive strain is applied to the device, the p-type depletion region increases in area and spreads out to form a semicircle in the

substrate. Current will be injected into the substrate along the entire boundary of the depletion region and travel to the substrate contact, as has been confirmed by plots of the current density. As the radius of the semicircular depletion boundary increases, the current must travel a larger average distance from injection to the contact due to the contribution of current streamlines injected on the side of the semicircle opposite the contact side, thereby increasing the effective series resistance of the substrate and decreasing the device current. When tensile strain is applied, the p-type depletion region shrinks and the n-type depletion region enlarges, shrinking the depletion region boundary to the diameter of the nanowire, and lowering the effective series resistance of the substrate. In support of this proposed mechanism, comparison simulations are also provided in Figure 34, showing that when hole mobility is artificially increased to a high value, the influence of strain on current will greatly diminish. Even though the change is related to a series of resistors, it is totally different from piezoresistance effect and contact area effect, as the change of resistance and current comes from the change of depletion area caused by the introduction of piezo-charges. The above analysis is consistent to the result shown in Figure 33b, where the I - V curves under different straining conditions are plotted. A monotonic increase in current with increasing tensile strain and decreasing compressive strain is clearly shown. For more intuitive understanding, the current at 6 V under each straining condition are plotted into one curve in Figure 34c. It is easy to conclude that under lower strain, the current changes almost exponentially with strain; however, under higher strain, the current will saturate when p-channel or n-channel forms at the interface. Another comparison is made for the relative change in current I_{strain}/I_0 under different bias voltage for each strain condition, as listed in Figure 34d. The value of I_{strain}/I_0 at any strain first increases quickly with V, and when V gets higher, I_{strain}/I_0 tends to slightly decrease with V, and finally saturates. When V and ε are small, the trend of I_{strain}/I_0 - V and I_{strain}/I_0 - ε are close to exponential, these results agree well with our previous analytical models in which exponential relationships

between I_{strain}/I_0 - V and I_{strain}/I_0 - ε were predicted. When V and ε gets larger, the I_{strain}/I_0 - V and I_{strain}/I_0 - ε are closer to linear, which also suggests the effect of series resistance as well as other non-ideal factors.

Based on the simulation of device current, we then control the parameters related to device design and study the optimization of the piezo-phototronics effect using numerical method.

Optimization of Piezo-phototronics Effect and Device Design

Study of Doping Profile

The doping profile of both the NW and the substrate is usually coupled with geometric factors and is an essential factor in device design. In the above sample simulation, the doping profile is set at a relatively low level. Simulating different doping profiles can help us compare the piezo-phototronics effect in materials synthesized by different methods. Several sets of simulations have been conducted to study the influence of doping. Figure 35a-c shows the I - V curves under different strain conditions when the doping profile is changed. Figure 35d plots the relative change of current I_{strain}/I_0 at 6 V bias under different strains for these simulations together for easier comparison. Same as the conclusion we provided in the simulation in previous discussion, applying tensile strain can still enhance the current under all of these conditions, but the extent of enhancement varies with different doping profile. Generally, when doping profile increases, the relative impact of the piezo-phototronic effect decreases; and when doping profile decreases, the impact of the piezo-phototronic effect increases. This is because the lower the doping profile, the greater the magnitude of the piezo-charge is relative to depletion charges, and the more significant the piezo-phototronics effect. This result can help explain the attenuation of piezo-phototronics effect in photodetection experiments with the increase of the detected light intensity.[4, 83] When detected light intensity

increases, the electron-hole pairs generated can overwhelm the influence of piezo-charges.

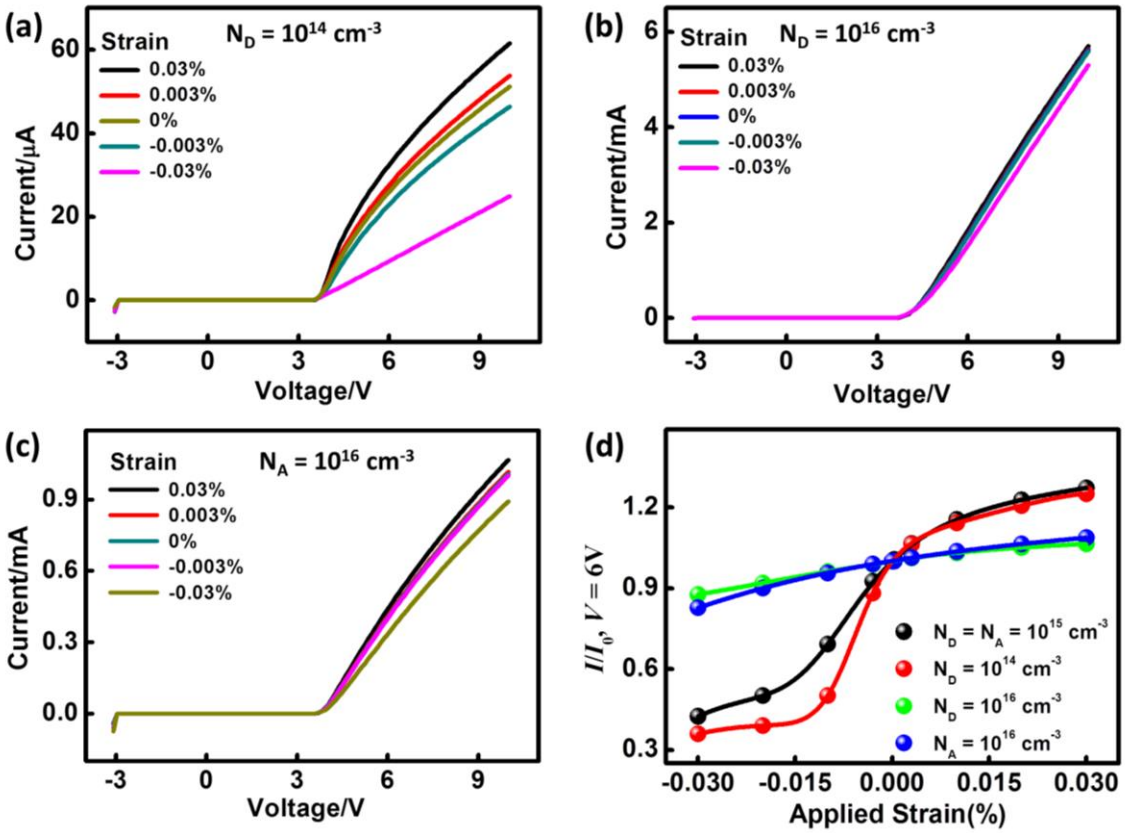

Figure 35 Current-Voltage simulation result from (a) N_D changes to 10^{14} cm^{-3}, (b) N_D changes to 10^{16} cm^{-3}, (c) N_A changes to 10^{16} cm^{-3}, (d) Comparison of calculated current at a fixed bias of 6 V for different doping concentrations by normalizing to the result received for $N_D = N_A = 10^{15}$ cm^{-3}

When the substrate doping reduces to 10^{14} cm^{-3} while the NW doping stays the same, the trend of I_{strain}/I_0 under different strain becomes unsteady, as shown in Figure 38. The reason for such behavior is multifold. When the substrate doping is small, the depletion region on the p-type side will be relatively large in size. In 1D calculation under strain free condition, decreasing the doping profile to 10% of original value results in 10 times larger depletion region. In 2D simulation, the change of depletion region profile varies in multiple directions. In the direction perpendicular to material interface, the change of depletion region is close to the change in 1D simulation; and along the direction parallel to material interface, the change of depletion region is smaller than that in 1D simulation. When the p-type depletion region is large enough to interact with the

electrode, it may be cut off in the electrode area, and influence of piezo-charges on band structure is much more complicated than previous simulation conditions. Therefore, the device current will also be influenced by both change in band structure and the inner resistance created within the depletion region and become unsteady.[84] This result provides sense that piezo-phototronics effect is optimized at certain doping profiles neither too high nor too low. The specific optimized value is also related to material properties.

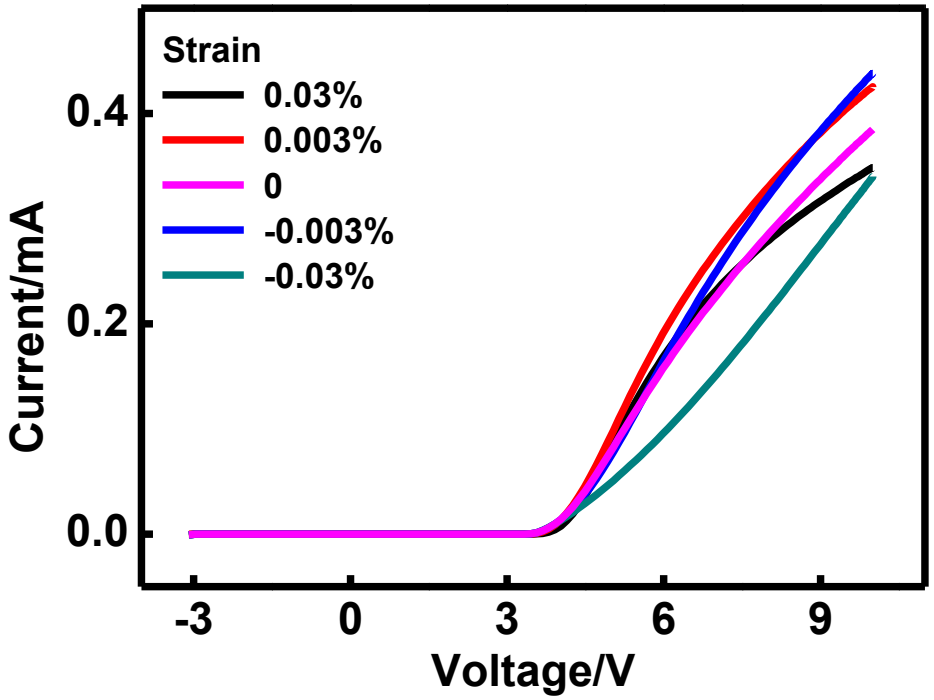

Figure 36 Current-voltage characteristics under different strain for $N_D = 10^{15}$ cm^{-3} and $N_A = 10^{14}$ cm^{-3}

Influence of Geometry Size

In bulk materials, the device size is orders of magnitude greater than the depletion width, and the electrode outlet is usually far away from the depletion region, the size or geometric layout usually influences the device performance only by influencing the equalized series resistance of the material. However, in the study of NW devices of micro-size structures, the size of the devices could easily be comparable to the size of the

depletion region, and thus their performance can be easily affected by geometry size. For example, when the geometry size is small, the depletion region may either be confined in the geometry in certain dimensions, or may overlap with the electrodes.

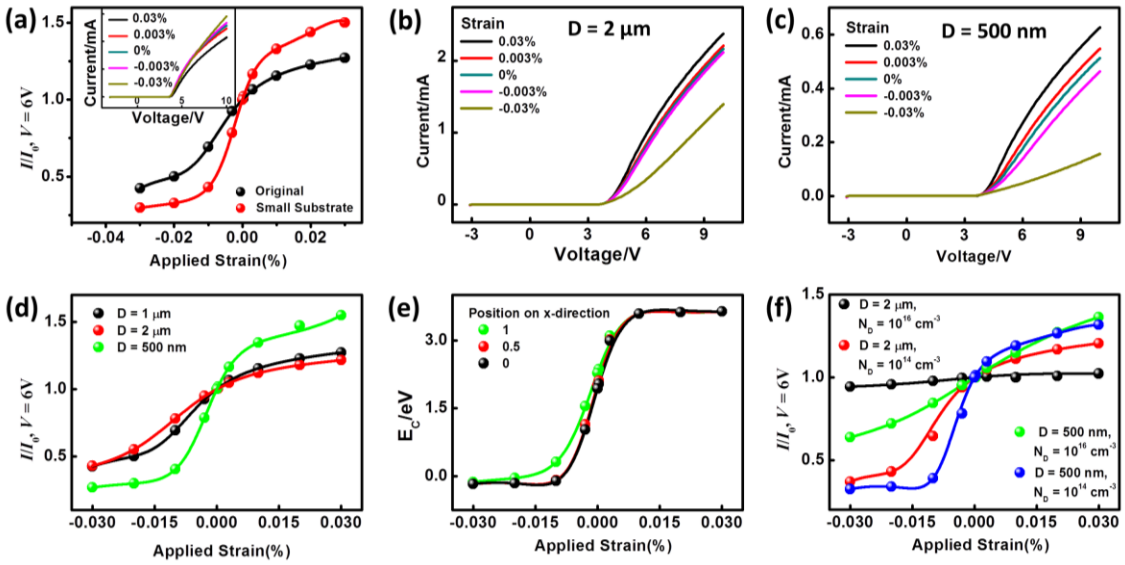

Figure 37 (a) Comparison of n-ZnO/p-ZnO with smaller substrate of size 5 μm × 5 μ m and result in figure 2, I_{strain}/I_0 vs ε at 6V bias, inset is the current-voltage characteristics of such simulation, (b) current-voltage characteristics of n-ZnO/p-ZnO with NW diameter D = 2 μm, (c) current-voltage characteristics of n-ZnO/p-ZnO with NW diameter D = 500 nm, (d) Comparison of I_{strain}/I_0 vs V, between Figure 39b, 39c with Figure 35c, (e) the E_C value under different strain for different locations along the direction parallel to material interface, position on x-direction is counted from the middle point in the piezo-charge distribution area, (f) relative change of current under different NW size and NW doping.

Simulation results with change of either the NW diameter or the substrate size are demonstrated in Figure 37. In Figure 37a, the substrate size in simulation was cut half in length and half in width for the structure, which means that the substrate size is 5 μm × 5 μm. From comparison with the original model, the relative current change at the same strain of the small device structure is about 20% larger than that of the original structure for all straining conditions. This kind of uniform enhancement under all strain conditions means that, as far as the simulated strain and applied voltage is concerned, the depletion region does not overlap with the electrodes and induce unsteadiness in current behavior, and such size shrink has mainly changed the series resistance.

Figure 37b has doubled the NW diameter and Figure 41c has cut the NW diameter in half. The overall comparison of *R* value for these two structures with the original

geometry is shown in Figure 37d. Besides inner resistance, this change also comes from the fact that, in direction parallel to material interface (*x*-direction), the change of band structure by strain is weaker than the change perpendicular to material's interface (*y*-direction), and thus the thinner the NW, the stronger overall the piezo-phototronics effect. For verification, we have plotted in Figure 37e the E_C value under different strain for different points along the direction parallel to material interface (*x*-direction), the *y* value for these points are in the middle of the piezo-charge distribution area. From an optimization aspect, as ZnO is non-ferroelectric, there is no such concept of domains as in PZT or $BaTiO_3$,[85-86] and as long as the NW size is larger than a few crystal lattices, smaller NW will give a stronger piezo-phototronics effect.

As a further step, a plot on the coupling of geometry size and doping profile is listed in Figure 37f. Four lines were plotted, each featuring different NW size and different NW doping. Lower NW doping and smaller NW size can both enhance the piezo-phototronics effect, yet their influence has minor difference. Lower NW doping results in a faster enhancement under lower strain, and the current saturates faster. Smaller NW size results in a more uniform change over the range of strain values.

Material Consideration and Device Design

In optoelectronic devices, heterojunctions are usually utilized to eliminate minority carrier injection and minimize photon reabsorption.[87] As far as band structure is concerned, the major difference between heterojunction and homojunction lies in the discontinuity formed in the interface between different materials and the associated band mismatch. This band discontinuity could provide an additional charge potential barrier depending on the materials used. Plus, heterojunctions can provide larger reflection in the material interface and is favored in LED fabrications. In the case of piezo-phototronics effect, piezo-charges can help either "recover" or enhance the discontinuity by tuning the local band structure.

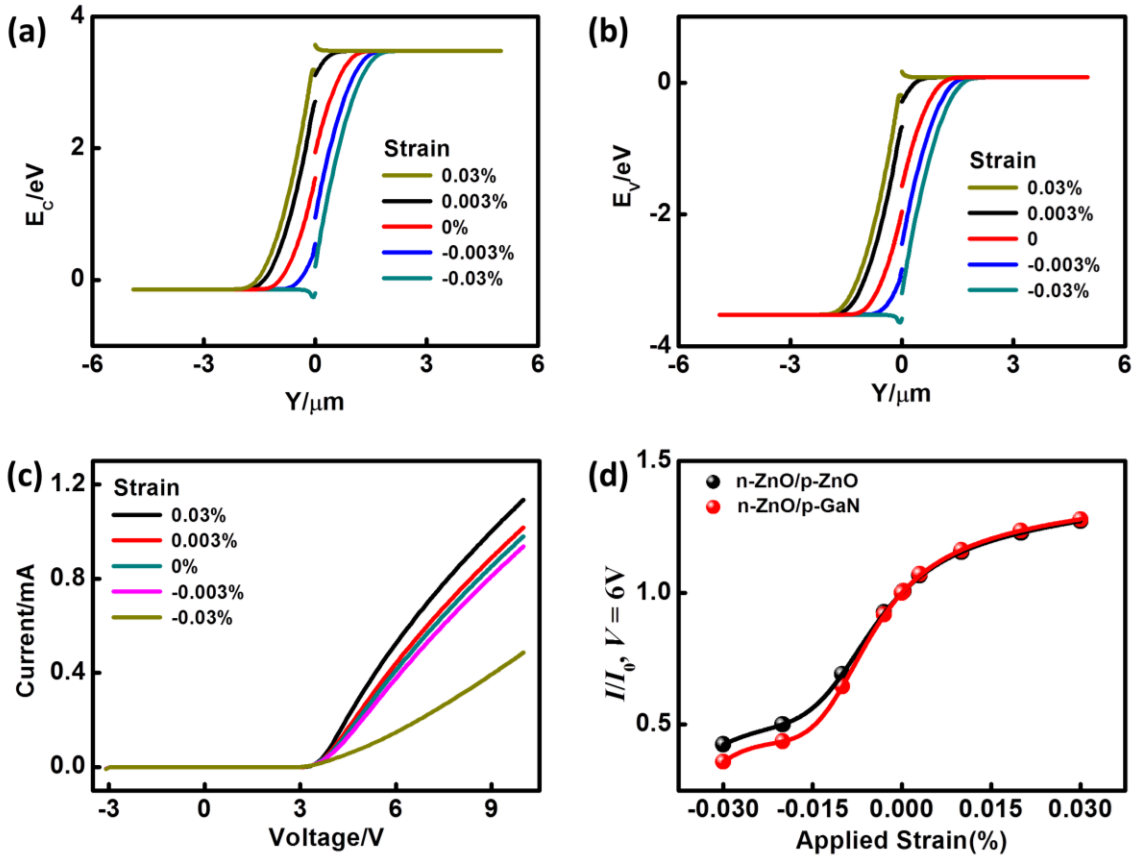

Figure 38 Simulation results for n-ZnO NW/p-GaN substrate structure, (a) Conduction band deformation of such structure under different strain at n-type side base on 1D simulation, which is chosen for comparison purpose, (b) Valence band deformation of such structure under different strain at n-type side based on 1D simulation, (c) current-voltage characteristics based on 2D simulation, geometry layout and doping are set as the same value as in Figure 35a, (d) I_{strain}/I_0 vs ε and comparison with Figure 35b.

Here we compare n-ZnO NW/p-GaN structure with the n-ZnO/p-ZnO structure to examine the influence of different types of junctions on the optimization of piezo-phototronics effect. From Table 2, the bandgap of ZnO and GaN are similar, leaving similar discontinuity in both valance band and conduction band, which simplifies the comparison of simulation result. For a simpler comparison and more intuitive perspective, the result for 1D calculation for heterojunction is shown in Figure 38a and 38b for conduction band and valence band as comparison for Figure 32a. From band structure calculation, the deformation under different strain is similar to the results for a homojunction. In calculation of the device current, the case is much more complicated, as parameters such as charge carrier mobility and diffusion constants can be totally different

in various materials under various doping condition, and discussion regarding different carrier mobility is too complicated and beyond the scope of this paper. For simpler comparison, a simulation setting the charge carrier mobility as the same value in GaN is performed, and the result is shown in Figure 38c and 38d. Figure 38c shows that the *I* - *V* curve under different strain condition is almost identical to that of a homojunction. The curve for current under 6 V bias voltage under different strain conditions are plotted together with that of homojunction in Figure 38d, which shows the impact of piezo-phototronics effect is slightly stronger in homojunction than in heterojunction, especially when compressive strain is applied, without considering the advantages of heterojunction in optoelectronics or the difference in charge mobility and lifetime between various materials. From previous discussions and comparison simulations displayed in Figure 33, lower hole mobility on the p-type side is also desired for the piezo-phototronics effect.

Simulation for Layouts in Experimental Reports

We have also performed simulation using material set up and geometry layout used in previous experiments,[5, 75] and the results are put in Figure 43. From the results, we have confirmed that the geometry layouts used in these experiments can also effectively display the piezo-phototronics effect, but these designs can be further optimized according to the methods provided here.

In previous experimental reports, the geometry layouts used in experiments were modelled by 1D calculation and lacks confirmation from proper 2D simulation and calculation. From the analysis presented in above sections, we have confirmed that under optimized geometry design and doping profile setting, the piezo-phototronics effect is able to influence the current-voltage characteristics. The typical device layouts used in past experiments, however, did not align the c-axis of piezoelectric NWs and the depletion region. This raises questions on whether the piezo-charge can influence the material on a different direction from basic intuitives. However, in 2D and 3D models,

considering there can be interaction between different directions, it is possible for such unaligned device layout to present piezo-phototronics. Using methods presented from the above sections, we have conducted simulations for two of the typical structures, and the results have confirmed that piezo-phototronics effect works very well on these structures.

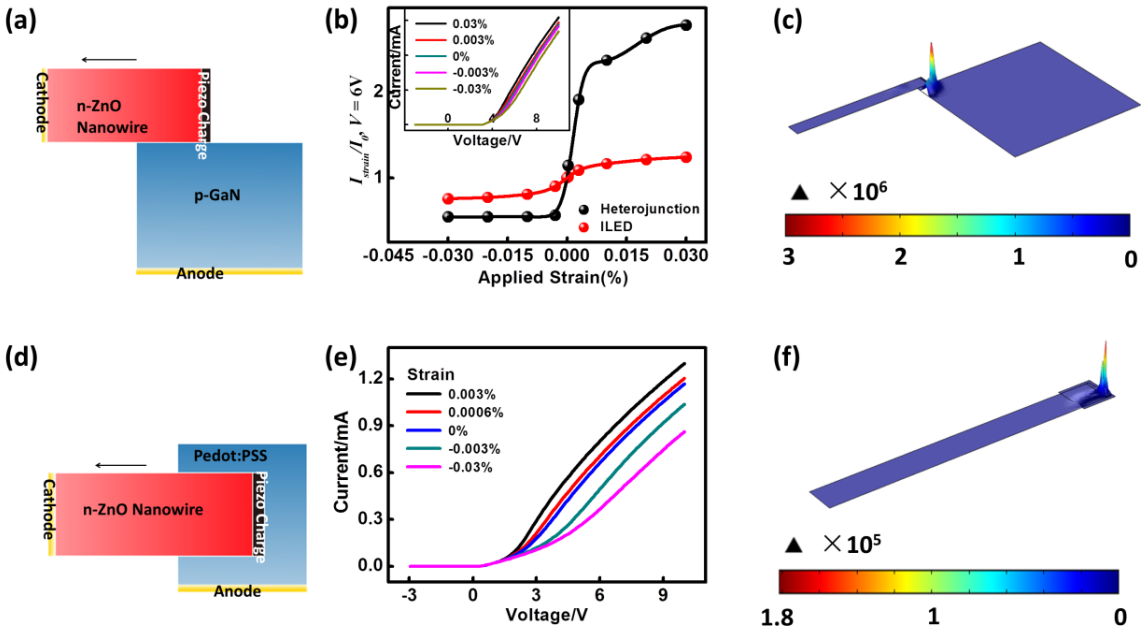

Figure 39 (a) Layout and simulation geometry of ZnO/GaN LED in experiments, (b) Simulation result of (a) and comparison with heterojunction simulated in Figure 36c, (c) current density of the ZnO/GaN LED in experiments, (d) Layout and simulation geometry of ZnO/PEDOT: PSS HyLED in experiments, (e) Simulation result of (d), (f) Current density of the ZnO/PEDOT: PSS HyLED in experiments

Figure 39a, b, c shows the device layout used in a single NW n-ZnO/p-GaN light emitting diode and 2D FEM simulation results. The ZnO NW lies flat on the GaN substrate. Figure 39b shows *R* under various strain of such a structure compared with original simulation in the manuscript. The unaligned geometry has reduced the piezo-phototronics effect, yet is still significant and agrees to previous experimental results. Figure 39c again confirms that majority of the current passed through the piezo-charge area, and light emission will be influenced by the charge channel formed there.

Figure 39d, e, f shows the device layout used in a single NW n-ZnO/p-polymer organic/inorganic hybrid light emitting diode and 2D FEM simulation results. The

polymer formed a layer of ultra-thin film and wrapped around the tip of the NW and the contact area is larger than in inorganic devices, meaning the weight of piezo-charge influence on device performance might be potentially lower. From the simulation, at a bias voltage of 6V, the current change at ±0.003% of strain is about ±30%. Considering the doping level on polymer side is lower, the piezo-phototronics effect has diminished by geometry, yet is still present and strong enough to substantially influence the device performance. Figure 39f again confirms that majority of the current passed through the piezo-charge area, and light emission will be influenced by the charge channel formed there. In real experiments, the presence of Schottky contact also introduced piezo-phototronics effect and the current behavior will be more complicated.

Influence of Electrode Layout

The electrode location varies from the application of the device. For optoelectronic nano devices, aligned anode and cathode on the ends of the device are usually used. In Figure 40, result for simulation of different electrode size and electrode location is plotted. It is easy to conclude that the anode mainly influences the magnitude of the current change, thus the depletion region do not overlap with the electrodes for these conditions. The cathode, however, plays a more important role, as piezo-charges are closer to the cathode side. Putting the cathode close to the depletion region can disturb the device performance and result in unsteady trend of change in device current.

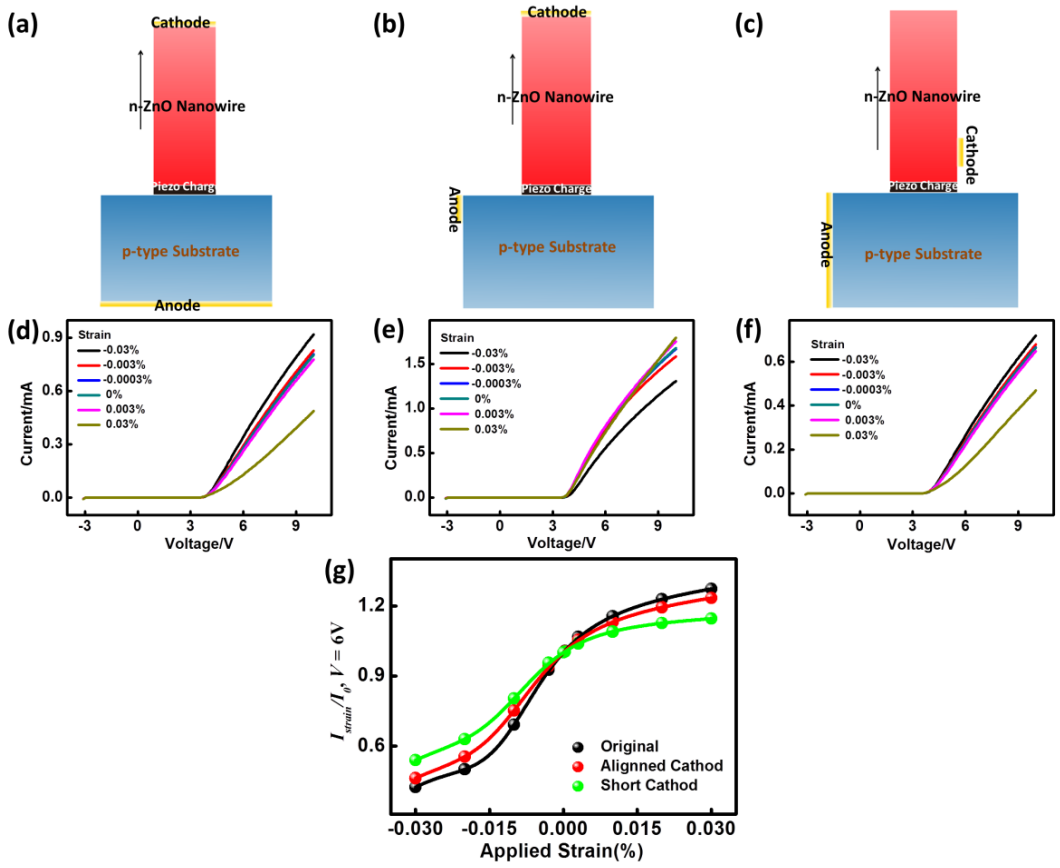

Figure 40 (a,b,c) Geometry layout of simulation (a) changing anode location, (b) changing anode size, (c) cathode location; (c,d,e) simulated current-voltage characteristics of (c) geometry in (a), (d) geometry in (b), (e) geometry in (c); (g) comparison of I_{strain}/I_0 *vs.* ε at 6 V bias for geometry in (a) and (b) with geometry in Figure 35a.

CHAPTER 6

CONCLUSION

Throughout the last five years, as a research assistant in Dr. Wang's group, I have worked towards making significant contributions in theory and experiment for piezo-phototronics effect. My contributions encompass the following topics.

Self-powered Photodetection System and Piezo-phototronics Effect in Photodetectors

A self-powered, ultrasensitive multicolor photodetector is fabricated. BFC with output of 60 mV voltage and 12 nA current was fabricated.[88] A single fiber MFC generates a DC output about V_{oc} = 295 mV and I_{sc} = 56 nA, and provides a power density of 30 W/m^2 of electrode geometry area. The self-powered photodetector can detect down to ~ nW/cm^2 level light intensity with responsivity of more than 300 A/W, which is two to three orders of magnitude higher than that achieved using a conventional MSM photodetector.[89]

Then, the piezo-phototronics effect is tested by testing visible light detection under various applied strain. For a Schottky-Ohmic structure, the responsivity has a monotonic change with the applied strain. Depending on the sign of strain and direction of the c-axis, the responsivity of different device can either increase or decrease. For a Schottky-Schottky structure, the responsivity under forward and reverse bias voltage shows an asymmetric behavior. The result is similar to previously reported ZnO NW UV light detection under strain, while the phenomenon is demonstrated in a more detailed manner and reveals the polar nature of the piezo-phototronics effect.

Piezo-phototronics Effect in LEDs

A strain-piezo charge tuned high efficiency ZnO NW/p-polymer air stable ultraviolet LED is demonstrated. The EQE of the hybrid LED can reach about 5.92% is demonstrated, which is comparable to that of inorganic p-n junction LED and quantum well enhanced nanowire LED.[75] Considering the difficulty in fabrication and conventional low efficiency in organic and inorganic/organic hybrid UV LED, this efficiency is an outstanding progress in reference to the published peer work. The significant enhancement is suggested due to a trimming of the electron current to match the hole current and increasing the localized hole density near the interface through the carrier channel induced by piezo charges. The asymmetric change of *I*-*V* curve under negative and positive bias proves that the enhancement is due to piezo-phototronic effect. The physical mechanism is explained by band diagram analysis. Piezo-phototronic effect enhanced ZnO NW/p-polymer LED represents an interesting alternative to organic LEDs. ZnO NW/GaN substrate LED arrays are fabricated with hydro-thermal process.[90] Strain is successfully applied onto the LED array to realize two-dimensional mechanical sensing.[91]

Theory for Piezo-phototronics Photodetection

A theoretical model is constructed for piezo-phototronic photodetectors based on metal-piezoelectric semiconductor-metal structures. The model works well with the experiments results on strain-piezo charge enhanced photodetector based on ZnO nanowires in ultraviolet wavelength range and CdS nanowires in visible wavelength range. We have then discussed other factors in the experiments and concluded three criteria based on the physics of piezo-phototronic photodetectors, to differentiate the piezo-phototronic effect from other effects. These criteria support our previous experimental results, and can give guidance to future experiments.[92]

Theory for Piezo-phototronics Effect in LEDs

A methodology is studied for numerically simulate the piezo-phototronics effect in nano LEDs for both 1D structure and 2D structure. By studying the change of band structure, we have confirmed the shift of depletion region and formation of charge channel at the interface with application of a proper amount of mechanical strain, which was proposed in previous experimental reports as the major mechanism for the gigantic increase of emission efficiency of LED. By simulating the current characteristics of 2D devices, we have studied the factors including doping profile, geometric factors and material considerations and their influence on the piezo-phototronics effect. We have found that lower NW doping and smaller NW size are favorable for application in piezo-phototronic nano LEDs, and without considering sophisticated factors like charge mobility, homojunctions are potentially more favorable than heterojunctions for improved piezo-phototronic effect. Our methodology has validated previous reported data, and can provide an optimization strategy for future experimental design of piezo-phototronic research.[93]

REFERENCES

1. Wang, Z. L., Piezopotential gated nanowire devices: Piezotronics and piezo-phototronics. *Nano Today* **2010,** *5* (6), 540-552.

2. Wang, Z. L., Progress in Piezotronics and Piezo-Phototronics. *Adv Mater* **2012,** *24* (34), 4632-4646.

3. Hu, Y. F.; Zhang, Y.; Chang, Y. L.; Snyder, R. L.; Wang, Z. L., Optimizing the Power Output of a ZnO Photocell by Piezopotential. *Acs Nano* **2010,** *4* (7), 4220-4224.

4. Yang, Q.; Guo, X.; Wang, W. H.; Zhang, Y.; Xu, S.; Lien, D. H.; Wang, Z. L., Enhancing Sensitivity of a Single ZnO Micro-/Nanowire Photodetector by Piezo-phototronic Effect. *Acs Nano* **2010,** *4* (10), 6285-6291.

5. Yang, Q.; Wang, W. H.; Xu, S.; Wang, Z. L., Enhancing Light Emission of ZnO Microwire-Based Diodes by Piezo-Phototronic Effect. *Nano Lett* **2011,** *11* (9), 4012-4017.

6. Knight, M. W.; Sobhani, H.; Nordlander, P.; Halas, N. J., Photodetection with Active Optical Antennas. *Science* **2011,** *332* (6030), 702-704.

7. Keuleyan, S.; Lhuillier, E.; Brajuskovic, V.; Guyot-Sionnest, P., Mid-infrared HgTe colloidal quantum dot photodetectors. *Nat Photonics* **2011,** *5* (8), 489-493.

8. Konstantatos, G.; Clifford, J.; Levina, L.; Sargent, E. H., Sensitive solution-processed visible-wavelength photodetectors. *Nat Photonics* **2007,** *1* (9), 531-534.

9. Irvin, P.; Ma, Y. J.; Bogorin, D. F.; Cen, C.; Bark, C. W.; Folkman, C. M.; Eom, C. B.; Levy, J., Rewritable nanoscale oxide photodetector. *Nat Photonics* **2010,** *4* (12), 849-852.

10. Zhou, J.; Gu, Y. D.; Hu, Y. F.; Mai, W. J.; Yeh, P. H.; Bao, G.; Sood, A. K.; Polla, D. L.; Wang, Z. L., Gigantic enhancement in response and reset time of ZnO UV

nanosensor by utilizing Schottky contact and surface functionalization. *Appl Phys Lett* **2009,** *94* (19).

11. Soci, C.; Zhang, A.; Xiang, B.; Dayeh, S. A.; Aplin, D. P. R.; Park, J.; Bao, X. Y.; Lo, Y. H.; Wang, D., ZnO nanowire UV photodetectors with high internal gain. *Nano Lett* **2007,** *7* (4), 1003-1009.

12. Bube, R. H., *Photoelectronic properties of semiconductors*. Cambridge University Press: Cambridge ; New York, 1992; p xviii, 318 p.

13. Rose, A., *Concepts in photoconductivity and allied problems*. Rev. ed.; Krieger: Huntington, N.Y., 1978; p xii, 168 p.

14. Jie, J. S.; Zhang, W. J.; Jiang, Y.; Meng, X. M.; Li, Y. Q.; Lee, S. T., Photoconductive characteristics of single-crystal CdS nanoribbons. *Nano Lett* **2006,** *6* (9), 1887-1892.

15. Pan, Z. W.; Dai, Z. R.; Wang, Z. L., Nanobelts of semiconducting oxides. *Science* **2001,** *291* (5510), 1947-1949.

16. Wei, T. Y.; Yeh, P. H.; Lu, S. Y.; Lin-Wang, Z., Gigantic Enhancement in Sensitivity Using Schottky Contacted Nanowire Nanosensor. *J Am Chem Soc* **2009,** *131* (48), 17690-17695.

17. Yeh, P. H.; Li, Z.; Wang, Z. L., Schottky-Gated Probe-Free ZnO Nanowire Biosensor. *Adv Mater* **2009,** *21* (48), 4975-+.

18. Hamilton, M. C.; Martin, S.; Kanicki, J., Thin-film organic polymer phototransistors. *Electron Devices, IEEE Transactions on* **2004,** *51* (6), 877-885.

19. Guiseppi-Elie, A.; Lei, C. H.; Baughman, R. H., Direct electron transfer of glucose oxidase on carbon nanotubes. *Nanotechnology* **2002,** *13* (5), 559-564.

20. Luong, J. H. T.; Hrapovic, S.; Wang, D.; Bensebaa, F.; Simard, B., Solubilization of multiwall carbon nanotubes by 3-aminopropyltriethoxysilane towards the fabrication of electrochemical biosensors with promoted electron transfer. *Electroanal* **2004,** *16* (1-2), 132-139.

21. Cai, C. X.; Chen, J., Direct electron transfer of glucose oxidase promoted by carbon nanotubes. *Anal Biochem* **2004,** *332* (1), 75-83.

22. Heller, A., Miniature biofuel cells. *Phys Chem Chem Phys* **2004,** *6* (2), 209-216.

23. Delumleywoodyear, T.; Rocca, P.; Lindsay, J.; Dror, Y.; Freeman, A.; Heller, A. A., Polyacrylamide-Based Redox Polymer for Connecting Redox Centers of Enzymes to Electrodes. *Anal Chem* **1995,** *67* (8), 1332-1338.

24. Barton, S. C.; Kim, H. H.; Binyamin, G.; Zhang, Y. C.; Heller, A., The "wired" laccase cathode: High current density electroreduction of O-2 to water at+0.7 V (NHE) at pH 5. *J Am Chem Soc* **2001,** *123* (24), 5802-5803.

25. Mano, N.; Mao, F.; Heller, A., Characteristics of a miniature compartment-less glucose-O-2 biofuel cell and its operation in a living plant. *J Am Chem Soc* **2003,** *125* (21), 6588-6594.

26. Chen, C. H.; Wang, K. R.; Tsai, S. Y.; Chien, H. J.; Wu, S. L., Nitride-Based Metal-Semiconductor-Metal Photodetectors with InN/GaN Multiple Nucleation Layers. *Jpn J Appl Phys* **2010,** *49* (4).

27. Gong, X.; Tong, M. H.; Xia, Y. J.; Cai, W. Z.; Moon, J. S.; Cao, Y.; Yu, G.; Shieh, C. L.; Nilsson, B.; Heeger, A. J., High-Detectivity Polymer Photodetectors with Spectral Response from 300 nm to 1450 nm. *Science* **2009,** *325* (5948), 1665-1667.

28. Luquet, H.; Gouskov, L.; Perotin, M.; Jean, A.; Magallon, D.; Lahbabi, M.; Bougnot, G., Noise Equivalent Power Calculation - Application to Ga0.96al0.04sb Avalanche Photodiodes. *J Appl Phys* **1988,** *64* (11), 6541-6545.

29. Wei, Y. C.; Song, J. X.; Chen, Q., In vivo detection of chemiluminescence to monitor photodynamic threshold dose for tumor treatment. *Photoch Photobio Sci* **2011,** *10* (6), 1066-1071.

30. Chen, J.; Keltner, L.; Christopherson, J.; Zheng, F.; Krouse, M.; Singhal, A.; Wang, S. S., New technology for deep light distribution in tissue for phototherapy. *Cancer J* **2002,** *8* (2), 154-163.

31. Schaetzle, O.; Barriere, F.; Baronian, K., Bacteria and yeasts as catalysts in microbial fuel cells: electron transfer from micro-organisms to electrodes for green electricity. *Energ Environ Sci* **2008,** *1* (6), 607-620.

32. Zimmler, M. A.; Voss, T.; Ronning, C.; Capasso, F., Exciton-related electroluminescence from ZnO nanowire light-emitting diodes. *Appl Phys Lett* **2009,** *94* (24).

33. Djurisic, A. B.; Ng, A. M. C.; Chen, X. Y., ZnO nanostructures for optoelectronics: Material properties and device applications. *Prog Quant Electron* **2010,** *34* (4), 191-259.

34. Wang, Z. L.; Yang, R. S.; Zhou, J.; Qin, Y.; Xu, C.; Hu, Y. F.; Xu, S., Lateral nanowire/nanobelt based nanogenerators, piezotronics and piezo-phototronics. *Mat Sci Eng R* **2010,** *70* (3-6), 320-329.

35. Heo, Y. W.; Norton, D. P.; Tien, L. C.; Kwon, Y.; Kang, B. S.; Ren, F.; Pearton, S. J.; LaRoche, J. R., ZnO nanowire growth and devices. *Mat Sci Eng R* **2004,** *47* (1-2), 1-47.

36. Zimmler, M. A.; Capasso, F.; Muller, S.; Ronning, C., Optically pumped nanowire lasers: invited review. *Semicond Sci Tech* **2010,** *25* (2).

37. Bao, J. M.; Zimmler, M. A.; Capasso, F.; Wang, X. W.; Ren, Z. F., Broadband ZnO single-nanowire light-emitting diode. *Nano Lett* **2006,** *6* (8), 1719-1722.

38. Park, W. I.; Yi, G. C., Electroluminescence in n-ZnO nanorod arrays vertically grown on p-GaN. *Adv Mater* **2004,** *16* (1), 87-+.

39. Zimmler, M. A.; Stichtenoth, D.; Ronning, C.; Yi, W.; Narayanamurti, V.; Voss, T.; Capasso, F., Scalable fabrication of nanowire photonic and electronic circuits using spin-on glass. *Nano Lett* **2008,** *8* (6), 1695-1699.

40. Weng, W. Y.; Chang, S. J.; Hsu, C. L.; Chang, S. P.; Hsueh, T. J., Laterally Grown n-ZnO Nanowire/p-GaN Heterojunction Light Emitting Diodes. *J Electrochem Soc* **2010,** *157* (9), Ii866-Ii868.

41. Law, M.; Greene, L. E.; Johnson, J. C.; Saykally, R.; Yang, P. D., Nanowire dye-sensitized solar cells. *Nat Mater* **2005,** *4* (6), 455-459.

42. Weintraub, B.; Wei, Y. G.; Wang, Z. L., Optical Fiber/Nanowire Hybrid Structures for Efficient Three-Dimensional Dye-Sensitized Solar Cells. *Angew Chem Int Edit* **2009,** *48* (47), 8981-8985.

43. Sanchez, C.; Lebeau, B.; Chaput, F.; Boilot, J. P., Optical properties of functional hybrid organic-inorganic nanocomposites. *Adv Mater* **2003,** *15* (23), 1969-1994.

44. Nadarajah, A.; Word, R. C.; Meiss, J.; Konenkamp, R., Flexible inorganic nanowire light-emitting diode. *Nano Lett* **2008,** *8* (2), 534-537.

45. Chang, C. Y.; Tsao, F. C.; Pan, C. J.; Chi, G. C.; Wang, H. T.; Chen, J. J.; Ren, F.; Norton, D. P.; Pearton, S. J.; Chen, K. H.; Chen, L. C., Electroluminescence from ZnO nanowire/polymer composite p-n junction. *Appl Phys Lett* **2006,** *88* (17).

46. Konenkamp, R.; Word, R. C.; Godinez, M., Ultraviolet electroluminescence from ZnO/polymer heterojunction light-emitting diodes. *Nano Lett* **2005,** *5* (10), 2005-2008.

47. Na, J. H.; Kitamura, M.; Arita, M.; Arakawa, Y., Hybrid p-n junction light-emitting diodes based on sputtered ZnO and organic semiconductors. *Appl Phys Lett* **2009,** *95* (25).

48. Sun, X. W.; Huang, J. Z.; Wang, J. X.; Xu, Z., A ZnO nanorod inorganic/organic heterostructure light-emitting diode emitting at 342 nm. *Nano Lett* **2008,** *8* (4), 1219-1223.

49. Son, D. I.; You, C. H.; Kim, W. T.; Kim, T. W., White light-emitting diodes fabricated utilizing hybrid polymer-colloidal ZnO quantum dots. *Nanotechnology* **2009,** *20* (36).

50. Zhao, S. L.; Kan, P. Z.; Xu, Z.; Kong, C.; Wang, D. W.; Yan, Y.; Wang, Y. S., Electroluminescence of ZnO nanorods/MEH-PPV heterostructure devices. *Org Electron* **2010,** *11* (5), 789-793.

51. Guo, H. G.; Zhou, J. Z.; Lin, Z. G., ZnO nanorod light-emitting diodes fabricated by electrochemical approaches. *Electrochem Commun* **2008,** *10* (1), 146-150.

52. Guo, Z.; Zhang, H.; Zhao, D. X.; Liu, Y. C.; Yao, B.; Li, B. H.; Zhang, Z. Z.; Shen, D. Z., The ultralow driven current ultraviolet-blue light-emitting diode based on n-ZnO nanowires/i-polymer/p-GaN heterojunction. *Appl Phys Lett* **2010,** *97* (17).

53. Braun, D.; Heeger, A. J.; Kroemer, H., Improved Efficiency in Semiconducting Polymer Light-Emitting-Diodes. *J Electron Mater* **1991,** *20* (11), 945-948.

54. Benor, A.; Takizawa, S. Y.; Chen, P.; Perez-Bolivar, C.; Anzenbacher, P., Dramatic efficiency improvement in phosphorescent organic light-emitting diodes with ultraviolet-ozone treated poly(3,4-ethylenedioxythiophene):poly(styrenesulfonate). *Appl Phys Lett* **2009,** *94* (19).

55. Zhou, J.; Gu, Y. D.; Fei, P.; Mai, W. J.; Gao, Y. F.; Yang, R. S.; Bao, G.; Wang, Z. L., Flexible piezotronic strain sensor. *Nano Lett* **2008,** *8* (9), 3035-3040.

56. Teke, A.; Ozgur, U.; Dogan, S.; Gu, X.; Morkoc, H.; Nemeth, B.; Nause, J.; Everitt, H. O., Excitonic fine structure and recombination dynamics in single-crystalline ZnO. *Phys Rev B* **2004,** *70* (19).

57. Zhang, B. P.; Binh, N. T.; Wakatsuki, K.; Segawa, Y.; Kashiwaba, Y.; Haga, K., Synthesis and optical properties of single crystal ZnO nanorods. *Nanotechnology* **2004,** *15* (6), S382-S388.

58. Kim, K. K.; Lee, S. D.; Kim, H.; Park, J. C.; Lee, S. N.; Park, Y.; Park, S. J.; Kim, S. W., Enhanced light extraction efficiency of GaN-based light-emitting diodes with ZnO nanorod arrays grown using aqueous solution. *Appl Phys Lett* **2009,** *94* (7).

59. Bester, G.; Wu, X. F.; Vanderbilt, D.; Zunger, A., Importance of second-order piezoelectric effects in zinc-blende semiconductors. *Phys Rev Lett* **2006,** *96* (18).

60. Zhang, Y.; Liu, Y.; Wang, Z. L., Fundamental Theory of Piezotronics. *Adv Mater* **2011,** *23* (27), 3004-3013.

61. Cady, W. G., *Piezoelectricity; an introduction to the theory and applications of electromechanical phenomena in crystals*. New rev. ed.; Dover Publications: New York,, 1964.

62. Wang, Z. L., Nanopiezotronics. *Adv Mater* **2007,** *19* (6), 889-892.

63. Wang, Z. L., Towards Self-Powered Nanosystems: From Nanogenerators to Nanopiezotronics. *Adv Funct Mater* **2008,** *18* (22), 3553-3567.

64. Neamen, D. A., *Semiconductor physics and devices : basic principles*. 3rd ed.; McGraw-Hill: Boston, 2003; p xxiv, 746 p.

65. Sze, S. M., *Physics of semiconductor devices*. 2nd ed.; Wiley: New York, 1981; p xii, 868 p.

66. Rhoderick, E. H.; Williams, R. H., *Metal-semiconductor contacts*. 2nd ed.; Clarendon Press ;
Oxford University Press: Oxford England
New York, 1988; p xiii, 252 p.

67. Zhang, Z. Y.; Yao, K.; Liu, Y.; Jin, C. H.; Liang, X. L.; Chen, Q.; Peng, L. M., Quantitative analysis of current-voltage characteristics of semiconducting nanowires: Decoupling of contact effects. *Adv Funct Mater* **2007,** *17* (14), 2478-2489.

68. Thomas, D. G.; Hopfield, J. J., Exciton Spectrum of Cadmium Sulfide. *Phys Rev* **1959,** *116* (3), 573-582.

69. Zhang, X. J.; Ji, W.; Tang, S. H., Determination of optical nonlinearities and carrier lifetime in ZnO. *J Opt Soc Am B* **1997,** *14* (8), 1951-1955.

70. Bridgman, P. W., The effect of homogeneous mechanical stress on the electrical resistance of crystals. *Phys Rev* **1932,** *42* (6), 0858-0863.

71. Smith, C. S., Piezoresistance Effect in Germanium and Silicon. *Phys Rev* **1954,** *94* (1), 42-49.

72. Chot, T., A Modified Forward I-U Plot for Schottky Diodes with High Series Resistance. *Phys Status Solidi A* **1981,** *66* (1), K43-K45.

73. Lien, C. D.; So, F. C. T.; Nicolet, M. A., An Improved Forward Iv Method for Nonideal Schottky Diodes with High Series Resistance. *Ieee T Electron Dev* **1984,** *31* (10), 1502-1503.

74. Boxberg, F.; Sondergaard, N.; Xu, H. Q., Photovoltaics with Piezoelectric Core-Shell Nanowires. *Nano Lett* **2010,** *10* (4), 1108-1112.

75. Yang, Q.; Liu, Y.; Pan, C. F.; Chen, J.; Wen, X. N.; Wang, Z. L., Largely Enhanced Efficiency in ZnO Nanowire/p-Polymer Hybridized Inorganic/Organic Ultraviolet Light-Emitting Diode by Piezo-Phototronic Effect. *Nano Lett* **2013,** *13* (2), 607-613.

76. Jeong, M. C.; Oh, B. Y.; Ham, M. H.; Myoung, J. M., Electroluminescence from ZnO nanowires in n-ZnO film/ZnO nanowire array/p-GaN film heterojunction light-emitting diodes. *Applied Physics Letters* **2006,** *88* (20).

77. Mohammad, S. N.; Salvador, A. A.; Morkoc, H., Emerging Gallium Nitride Based Devices. *P Ieee* **1995,** *83* (10), 1306-1355.

78. Janotti, A.; Van de Walle, C. G., Fundamentals of zinc oxide as a semiconductor. *Rep Prog Phys* **2009,** *72* (12).

79. Wu, C. I.; Kahn, A., Electronic states and effective negative electron affinity at cesiated p-GaN surfaces. *Journal of Applied Physics* **1999,** *86* (6), 3209-3212.

80. Sze, S. M.; Ng, K. K., *Physics of semiconductor devices*. 3rd ed.; Wiley-Interscience: Hoboken, N.J., 2007; p x, 815 p.

81. Joo, J.; Chow, B. Y.; Prakash, M.; Boyden, E. S.; Jacobson, J. M., Face-selective electrostatic control of hydrothermal zinc oxide nanowire synthesis. *Nat Mater* **2011,** *10* (8), 596-601.

82. Pan, C. F.; Niu, S. M.; Ding, Y.; Dong, L.; Yu, R. M.; Liu, Y.; Zhu, G.; Wang, Z. L., Enhanced Cu2S/CdS Coaxial Nanowire Solar Cells by Piezo-Phototronic Effect. *Nano letters* **2012,** *12* (6), 3302-3307.

83. Niu, S. M.; Hu, Y. F.; Wen, X. N.; Zhou, Y. S.; Zhang, F.; Lin, L.; Wang, S. H.; Wang, Z. L., Enhanced Performance of Flexible ZnO Nanowire Based Room-Temperature Oxygen Sensors by Piezotronic Effect. *Advanced materials* **2013,** *25* (27), 3701-3706.

84. Chakrabarty, K.; Singh, S. N., Depletion layer resistance and its effect on I-V characteristics of fully- and partially-illuminated silicon solar cells. *Solid-State Electronics* **1996,** *39* (4), 577-581.

85. Yun, W. S.; Urban, J. J.; Gu, Q.; Park, H., Ferroelectric properties of individual barium titanate nanowires investigated by scanned probe Microscopy. *Nano letters* **2002,** *2* (5), 447-450.

86. Scott, J. F., Applications of modern ferroelectrics. *Science* **2007,** *315* (5814), 954-959.

87. Kasap, S. O., *Optoelectronics and photonics : principles and practices*. 2nd ed.; Pearson: Boston, 2013; p xvii, 528 p.

88. Hansen, B. J.; Liu, Y.; Yang, R. S.; Wang, Z. L., Hybrid Nanogenerator for Concurrently Harvesting Biomechanical and Biochemical Energy. *Acs Nano* **2010,** *4* (7), 3647-3652.

89. Yang, Q.; Liu, Y.; Li, Z. T.; Yang, Z. Y.; Wang, X.; Wang, Z. L., Self-Powered Ultrasensitive Nanowire Photodetector Driven by a Hybridized Microbial Fuel Cell. *Angew Chem Int Edit* **2012,** *51* (26), 6443-6446.

90. Xu, S.; Xu, C.; Liu, Y.; Hu, Y. F.; Yang, R. S.; Yang, Q.; Ryou, J. H.; Kim, H. J.; Lochner, Z.; Choi, S.; Dupuis, R.; Wang, Z. L., Ordered Nanowire Array Blue/Near-UV Light Emitting Diodes. *Adv Mater* **2010,** *22* (42), 4749-4753.

91. Pan, C. F.; Dong, L.; Zhu, G.; Niu, S. M.; Yu, R. M.; Yang, Q.; Liu, Y.; Wang, Z. L., High-resolution electroluminescent imaging of pressure distribution using a piezoelectric nanowire LED array. *Nat Photonics* **2013,** *7* (9), 752-758.

92. Liu, Y.; Yang, Q.; Zhang, Y.; Yang, Z. Y.; Wang, Z. L., Nanowire Piezo-phototronic Photodetector: Theory and Experimental Design. *Adv Mater* **2012,** *24* (11), 1410-1417.

93. Liu, Y., Niu, S., Yang, Q., Klein, B. D., Zhou, Y. S., Wang, Z. L., Theoretical Study of Piezo-Phototronic Nano-LEDs. *Adv Mater* **2014,** *Submitted*.

VITA

YING LIU

YING was born in Wuhan, Hubei Province of China, which is also known as “the City of Yangzi River” and “the City of Hundred Lakes”. She received a B.S. in Physics from Peking University, Beijing, China in 2009 before coming to Georgia Tech to pursue her Doctorate in Materials Science and Engineering. When she is not working on her research, she enjoys Kunqu Opera and hiking.